QUANTIFYING UNCERTAINTY OF PROBABLE MAXIMUM FLOOD

A Dissertation

by

YU ZHANG

Submitted to the Office of Graduate and Professional Studies of
Texas A&M University
in partial fulfillment of the requirements for the degree of

DOCTOR OF PHILOSOPHY

Chair of Committee,	Vijay P. Singh
Committee Members,	Daren Cline
	Patricia Smith
	Srinivasulu Ale
Head of Department,	John Tracy

May 2021

Major Subject: Biological and Agricultural Engineering

ABSTRACT

Probable maximum flood (PMF) has been used in large hydraulic infrastructure design for decades. However, a complete framework for deriving PMF with uncertainty analysis is lacking. This study investigated from probable maximum precipitation (PMP) with uncertainty to probable maximum storm (PMS), rainfall-runoff (R-R) model with uncertainty, and PMF with uncertainty. A basin-scale model, based on the Hershfield method, was developed for calculating PMP and uncertainty. It showed that PMP and uncertainty from the proposed method were more reliable than other statistical methods because of less restrictive assumptions and the improvement in methodology. The average improvements in terms of the difference percentages for 1-hour, 6-hour and 24-hour duration PMPs were 53.84%, 81.04% and 72.60%, respectively. The improvements in uncertainty by the Delta method were 15.54%, 9.71%, 8.93%, respectively. Hydro-meteorological Report No. 52 (HMR 52) with updated data was adopted to design the PMS from PMP. The updated storm records indicated a different within/without-storm depth-area relation (WWSDA) than HMR 52. The PMP values with 95% confidence interval (CI) were transferred to PMSs utilizing the DAD maps and the WWSDA relations. With the GLUE methodology, the impacts of different sources of uncertainty on the R-R model performance and uncertainty were investigated. Results showed that the uncertainties were more sensitive to smaller basin area, average area of subbasin, precipitation intensity, and observed peak flow, which means that for extreme events modeling with opposite basin features, the selection of model input and model setup had

less impact on model performance and uncertainty. PMSs were then routed by the R-R model with uncertainty to obtain the PMF with uncertainty. Results showed that in lower Brazos River basin, the PMF peak flow derived by the average PMP value was 12716 CMS, which was around three times the peak flow from hurricane Harvey (3764 CMS). The 95% PMP CI was 54.5 mm and resulted in a 3656 CMS difference between the corresponding PMF peak flows. For the peak flow uncertainty, the PMP uncertainty accounted for most of the parts (81%), while the R-R model uncertainty accounted for less (19%).

ACKNOWLEDGEMENTS

I would like to thank my committee chair, Dr. Vijay P. Singh, and my committee members, Dr. Srinivasulu Ale, Dr. Daren Cline and Dr. Patricia Smith, for their guidance and support throughout the course of this research.

Thanks also go to my friends and colleagues and the department faculty and staff for making my time at Texas A&M University a great experience.

Finally, thanks to my mother, father and sister for their love and support.

CONTRIBUTORS AND FUNDING SOURCES

Contributors

This work was supervised by a thesis (or) dissertation committee consisting of Professor Vijay P. Singh of the Department of Biological and Agricultural Engineering Professor Srinivasulu Ale of the Department of Biological and Agricultural Engineering, Professor Daren Cline of the Department of Statistics and Professor Patricia Smith of the Department of Biological and Agricultural Engineering.

The research structure and main review was directed by Professor Vijay Singh. The method for PMP estimation in Chapter II was guided in part by Professor Daren Cline. The analyses depicted in Chapter II were published in 2019. The analyses depicted in Chapter IV were submitted to a journal in 2020.

All other work conducted for the thesis (or) dissertation was completed by the student independently.

Funding Sources

The completion of thesis was supported by a dissertation fellowship from OGAPS of Texas A&M University.

This work was also made possible in part by project “Quantifying Uncertainty of Probable Maximum Flood (PMF),” project no. W912HZ-16-C-0027, funded by the U.S. Army Corps of Engineers, Engineering Research Development Center, Vicksburg, Mississippi. Its contents are solely the responsibility of the authors and do not necessarily represent the official views of the USACE.

NOMENCLATURE

95PPU	95% Prediction Uncertainty
BARE	Bayesian Recursive Estimation
CDF	Cumulative Duration Frequency
CI	Confidence Interval
CN	Curve Number
DAD	Depth-Area-Duration
DEM	Digital Elevation Model
DYNIA	Dynamic Identifiability Analysis
FFA	Flood frequency analysis
GEV	Generalized Extreme Value
GLUE	General Likelihood Uncertainty Estimation
HEC-HMS	Hydrologic Engineering Center of U.S. Army Corps of Engineers
HMR 51	Hydrometeorological Report NO. 51
HMR 52	Hydrometeorological Report NO. 52
HUC	hydrologic unit code
IC	Initial and Constant
K	Frequency Factor
MLBMA	Maximum Likelihood Bayesian Averaging Method
MRLC	Multi-Resolution Land Characteristics
NEXRAD	Next Generation Weather Radar

NOAA	National Oceanic and Atmospheric Administration
NRCS	Natural Resources Conservation Service
NSE	Nash-Sutcliffe Efficiency
NWS	National Weather Service
PMF	Probable Maximum Flood
PMP	Probable Maximum Precipitation
PMS	Probable Maximum Storm
R-R	Rainfall-Runoff
SCEM	Shuffled Complex Evolution Metropolis
SCS	Soil Conservation Service
SODA	Simultaneous Optimization and Data Assimilation Algorithm
SUFI	Sequential Uncertainty Fitting
TCEQ	Texas Commission on Environment Quality
USDA	United States Department of Agriculture
USGS	United States Geological Survey
WMO	World Meteorology Organization
WWSDA	Within/without-storm Depth-area

TABLE OF CONTENTS

Page

LIST OF FIGURES

Page

LIST OF TABLES

Page

CHAPTER I

INTRODUCTION

1.1 Significance and Objectives

1.1.1 Statement of Problems and Research Gap

In 2017 (17 August – 1 September), hurricane Harvey brought catastrophic flooding to the coastal parts of Texas, which caused huge damages to properties and lives. It was stated as the second most costly hurricane in the United States history only behind Katrina (2005), causing 68 direct deaths (Blake and Zelinsky, 2018). Texas has seen its share of hurricane activity over the centuries. The annual average occurrence of a tropical storm or hurricane in Texas per year is 0.8, or 3 per every 4 years (Roth, 2010). The particular geomorphology, climatic characteristics, storm or hurricane strength level, and storm water management of the region together determine the damage or property loss level due to flooding caused by a storm or hurricane.

It is impossible to prevent the storm from happening or decide the intensity of the storm in the region, but predictions and estimates of potential flooding and its time history (hydrograph) can be utilized to improve stormwater management. Hydrographs and inundation maps of the events are the most useful indicators of flood damages. Thus, a multitude of concepts, methods, and models have been developed to simulate the process of extreme weather events. Usually, by hydrologic and hydraulic modeling, predicting a flood and its return period is the ultimate goal. Flood frequency analysis (FFA) has been the most common method used to achieve this goal. Numerous approaches to FFA have been developed using both traditional methods (such as

physical hydrology models) and relatively new developed methods (such as artificial neural network models) (Singh and Strupczewski, 2002; ASCE, 2000). FFA associates risk to return period, which means a specific probability is assigned to a flood peak magnitude. However, an upper bound of extreme floods is of greater interest, because one can then approximately estimate the worst damage that could happen and develop measures to reduce the level of damage and property loss.

Contrary to FFA, probable maximum flood (PMF), which is regarded as an upper flow limit, removes the constraint of specifying a return period. It is defined as "the flood that may be expected from the most severe combination of critical meteorologic and hydrologic conditions that are reasonably possible in the drainage basin under study" (FEMA, 1998). It has been widely studied over decades and has been sed to set the design limit for large hydraulic structures, such as large dams, spillways, levees and major flood control works, and nuclear power plants. However, there are large uncertainties in deriving PMF. PMF is derived from probable maximum precipitation (PMP), which is the theoretically greatest depth of precipitation for a given storm duration that is physically possible over a given size storm area at a particular geographical location at a certain time of the year (WMO 1986, 2009). Before PMP can be transformed to PMF, its temporal and spatial distribution needs to be specified, which results in a probable maximum storm (PMS).

A typical procedure for deriving PMF is as follows: estimate PMP values, construct a synthetic PMS for PMP, build an R-R model and route the PMS with the R-R model to get PMF. There are deterministic and statistical methods to estimate PMP

(Schreiner and Riedel, 1978; Hershfield 1961), which utilize storm maximization and frequency analysis of historical precipitation records, respectively. The Hydrometeorological Report No. 52 (HMR 52) proposed a complete procedure to develop a synthetic PMS with both temporal and spatial distribution. The temporal distribution specifies the arrangement of precipitation increments in the sequence. The spatial distribution describes the shape and orientation of the storm pattern and magnitudes of isohyets(Hansen et al. 1982).

Numerous R-R models have been developed to study the basin hydrology (Devia et al. 2015). Even though separate studies in each area have been conducted, an integrated study with a complete framework for deriving PMF seems to be lacking (Alaya et al., 2018; Chavan and Srinivas, 2015; Casas et al., 2011; Chen et al., 2017; Lee and Singh, 2020; Clavet-Gaumont et al., 2017; Gangrade et al., 2018). The uncertainty of PMF stems from the above three steps in the procedure for deriving PMF. Few studies have investigated the uncertainty caused by each step, not to mention an integrated quantification of uncertainty for the complete procedure. Figure 1 shows the uncertainty accumulation, including the causes of uncertainties. To our knowledge, no systematical study has been done to estimate the uncertainty from all steps.

Most of the studies focused only on the PMP uncertainty but did not incorporate the PMS design and the R-R model uncertainty, and consequently the PMF uncertainty was not determined. Salas et al. (2014) proposed a method to quantify the uncertainty of the statistical method of PMP estimation and analyzed the sensitivity of PMF using the Monte Carlo method. However, the uncertainty caused by the R-R model and PMS were

not included. Micovic et al. (2015) estimated the uncertainty of a deterministic method of PMP estimation but did not investigate the uncertainty of PMF. Zhang et al. (2019) proposed a statistical basin-scale method to estimate PMP and quantified the PMP uncertainty accordingly. Even though there were studies investigating the propagation of uncertainty from rainfall to runoff, e.g., uncertainties from a stochastic rainfall generator (Gabellani et al. 2007), there were no studies in quantifying the uncertainty of constructing a PMS. Because the complexity of the definition of 'probable maximum' and the necessity of referring historical extreme events made it hard to achieve the goal. Sources of uncertainties from R-R models and methods of quantifying such uncertainties have been summarized by (Moradkhani and Sorooshian, 2009; Liu and Gupta, 2007). Only a few studies focused on the uncertainty of R-R models related to extreme events or PMF.

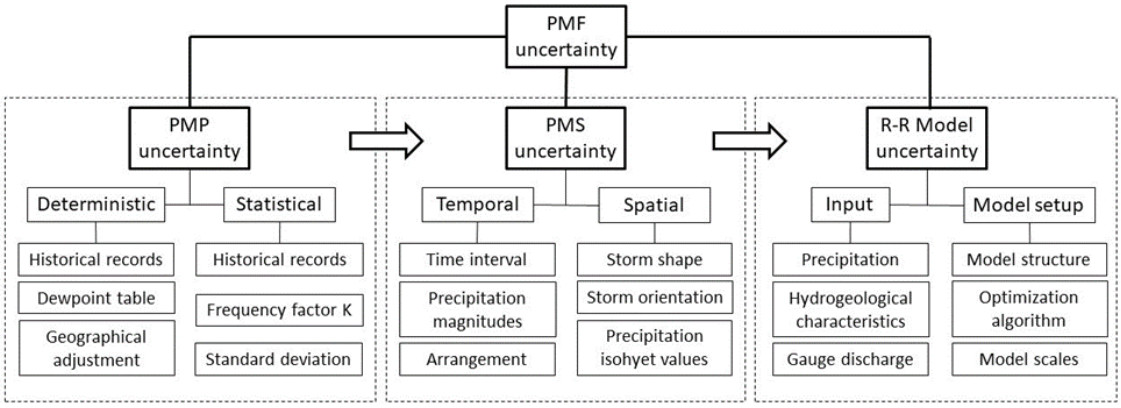

Figure 1 Main steps for deriving PMF and uncertainty.

Thus, this study aims to calculate PMF and quantify the uncertainty associated with it from all the involved procedures, so that the government or decision makers can find a reliable design standard for large flood control structures and get a better understanding of uncertainties in inundation mapping to mitigate catastrophic flood damages.

1.1.2 Objectives of the Research

Methods for each step shown in Figure 1 need to be specified before PMF can be derived. The corresponding uncertainties from all the steps can then be quantified cumulatively. It is noted that the uncertainty of constructing a PMS will not be included in this study. The process of PMS design is deterministic where the uncertainty can only be expressed with numerical sampling. However, this sampling procedure will make it almost impossible to qualify the propagated uncertainty of PMF because of its complexity. The detailed explanation will be discussed in the PMS design section. Above all, the objective of this study is to develop a complete framework to derive PMF and determine the uncertainty associated with the PMF value, depending on all the procedures employed. The framework will be implemented with a case study in Brazos River basin, TX, USA. The specific objectives of the study are:

1) Propose an enhanced basin-scale Hershfield method to execute PMP and uncertainty;

2) Update the historical storms used to construct PMS and develop a synthetic PMS with the guidance of HMR 52;

3) Create a R-R model for extreme event simulation in large-scale basin with parameter uncertainty analysis; and

4) Transfer PMP to PMF using the model mentioned in 2) and systematically define all the uncertainties in the process of deriving PMF.

1.1.3 Chapters Arrangement and Descriptions

To better implement the objectives, the main content of the study is composed of six chapters. Chapter I is introduction which describes the significance and objectives of the study. It also introduces definitions of concepts and former studies in the research area. Chapter II focuses on developing a statistical method of PMP estimation and quantifying the uncertainty embedded in the procedure. Chapter III develops the PMS by the method from HMR 52 and updates big storm data centered on Texas. Chapter IV constructs an R-R model with uncertainty analysis and the consequent PMF with uncertainty. Chapter V contains the discussion and conclusions.

1.2 Probable Maximum Precipitation and Uncertainty

As stated above, because PMF cannot be quantitatively defined, it is usually generated from PMP. The PMP concept originated in the middle 1930's (Paulhus and Gilman, 1953) and was formally defined (American Meteorological Society, 1959) as "the theoretically greatest depth of precipitation for a given duration that is physically possible over a particular drainage basin at a particular time of the year." There were controversies about whether a limit exists. For example, Myers (Myers, 1967) believed

that in general, procedures employed yield estimates that are close enough to what nature can ultimately produce. The users of the PMP concept followed the similar rationale that nature will not produce an infinite amount of rainfall for conditions mentioned in the PMP definition, while many hydrologists criticized the concept by questioning the existence of an upper bound of the amount of rainfall. (Dingman, 1994; Benson, 1973; Wileeke, 1980) The current PMP (refined by Hansen, et al., 1982) is defined as: theoretically the greatest depth of precipitation for a given storm duration that is physically possible over a given size storm area at a particular geographical location at a certain time of the year (Hansen, et al., 1982; WMO, 1986; WMO, 2009). This new definition only differed from the former one by stating that PMP is a function of storm area size instead of specific drainage area, which is a more accurate way of defining PMP and has been used as the standard definition since then. There were continuing developments of the method since PMP was first formally defined in the glossary of the American Meteorological Society (1959), while two main categories can be summarized as deterministic/meteorological method and statistical method. The initial method of PMP is the meteorological method which utilizes meteorological records and is physically based. Though the meteorological method considers most of the important factors related to precipitation (i.e. temperature, moisture, wind, etc.), it cannot be applied to areas that have no meteorological records. On the other hand, statistical method was developed later than was the meteorological method (e.g. Hershfield, 1961; Koutsoyiannis,1999; Douglas and Barros, 2003). It utilizes historical

precipitation records and is based on frequency analysis or probability inference. Introduction of both kinds of methods now follows.

1.2.1 Deterministic Method of Probable Maximum Precipitation Estimation

The basic deterministic method (sometimes called storm maximization method) used in estimating PMP has been described in numerous publications (Paulhus and Gilman, 1953; WMO,1969a; WMO, 1973 and WMO, 2009). In addition, the most comprehensive and complete studies on PMP were conducted by National Weather Service (NWS) of National Oceanic and Atmospheric Administration (NOAA), USA, since the late 1940's. NWS provided full documents of PMP studies of different regions within United States, though it stopped updating beginning with 1999 (https://www.nws.noaa.gov/oh/hdsc/studies/pmp.html). The documents were named as Hydrometeorological Reports with series number appended (e.g., HMR 51). Each of them discussed a PMP study for a particular region (orographic or non-orographic) with variations in methodology. The underlying rationale of deterministic method is to maximize the observed major storms with three main steps: 1) moisture maximization of observed extreme precipitation amounts, 2) transposition to the location of interest of those moisture maximized storm values that are within a meteorologically homogeneous region, and 3) envelopment of the maximized, transposed depth-duration and depth-area amounts. This procedure follows physical laws which make it a deterministic method. Detailed equations and steps for the application for this method can be referred to HMR 51. Despite the firm methodology, meteorological method has many uncertainties

embedded in the three steps, which can be quantified with numerical sampling such as Monte Carlo process. For example, Micovic et al. (2015) quantified PMP uncertainties from five main sources in the deterministic method. Due to the intensive data requirement for this method, for regions with scarce data, this method is not an appropriate choice. Thus, we focus on the statistical method of PMP estimation in this study.

1.2.2 Statistical Method of Probable Maximum Precipitation Estimation

Though the deterministic method considers most of the important factors related to precipitation (i.e., temperature, moisture, etc.), it cannot be applied to areas that have scarce meteorological records. On the other hand, statistical methods (e.g. Hershfield, 1961; Koutsoyiannis,1999; Douglas and Barros, 2003) utilize historical precipitation records and are based on frequency analysis or probability inference. Among the statistical methods, the Hershfield method has been most widely used because of the relatively large data sets it analyzed, the logical frequency analysis it derived, and the recognition by WMO (2009) (Casas et al., 2008; Desa and Rakhecha, 2007; Dhar et al., 1980; Mejia and Villegas, 1979; Nobilis et al., 1991; Rakhecha and Soma, 1994; Rezacova et al., 2005; Zhou et al., 2014; Sherif et al., 2014).

The underlying concept of the Hershfield method is that the frequency of a PMP value is expressed as a function of mean, $\overline{X_n}$, standard deviation, S_n, and frequency factor, *K* (Hershfield, 1961, 1965). Though the Hershfield method is simple to apply and is most widely used, it is necessary to explore the accuracy and application flexibility of

the method for different scales, since studies showed controversies about the method (e.g., controversy about no upper limit for extreme precipitation existing, historical records exceeding PMP, Hershfield PMP values are significantly larger than deterministic method results) (Benson, 1973; Dingman, 1994; Salas et al., 2014). Another problem is that the PMP uncertainty needs to be defined during the procedure of estimating PMP. The computed PMP values have uncertainties caused by K, $\overline{X_n}$ and S_n, that is, (unknown) true value and computed value are different (Nearing et al., 2016).

In recognition of finding a specific value of PMP that was impossible, Koutsoyiannis (1999) reanalyzed Hershfield's method and derived a generalized extreme value (GEV) distribution of K. He argued that the PMP value can be assigned an exact number as long as a probability is assigned, i.e. K=15 corresponds to a return period of 60,000 years, based on Koutsoyiannis's method. However, this argument deviates from the initial meaning of the PMP definition, which is to find the exact number with zero risk. Assuming PMP as an independent variable, Salas et al. (2014) quantified the uncertainty in applying the Hershfield method. They determined the variance of PMP and used Chebyshev's inequality to probabilistically state the value of PMP with uncertainty. It was the only study that quantified the uncertainty in the Hershfield method, which provided a way to consider the PMP uncertainty in the statistical method. They assumed K as a constant which caused no uncertainty (in actuality K is not constant and will cause uncertainty) and PMP to have a normal (which is not necessarily true) or Gumbel distribution.

Hershfield (1961) made enveloping curves of *K* using data from 2,645 stations in the U.S. and around the world. Also, it assumed that the data from 2,645 stations came from the same population, while, because of differences in natural characteristics from one watershed or drainage area to another, in fact, the data came from different populations. Thus, it is of interest to explore if a basin-scale model could be developed to improve the accuracy, because the assumption that basin-scale data comes from the same population is more valid. On the other hand, other methodologies should be explored to quantify the uncertainty comprehensively. This potential method should involve the uncertainty caused by *K* and not need the normality assumption as Salas et al. (2014) made.

In order to solve the problems described above, this study develops a model for computing PMP at the basin scale and quantifies the uncertainty caused by *K*, $\overline{X_n}$ and S_n with no particular assumption about the distribution of PMP. The proposed model is supposed to produce results which are more consistent with those reported by TCEQ (deterministic method results) and be an improvement over the Hershfield method and also over the method of Salas et al. (2014). Brazos River basin, Texas, USA was chosen to be a study case while the proposed model should be applicable to any other basin. Detailed methodology will be discussed in Chapter II. The specific objectives for this chapter are to: 1) develop a new basin-scale model based on the Hershfield method; 2) derive 1-hour, 6-hour, and 24-hour PMP from the Hershfield method and basin-scale method, and compare them with the TCEQ results; 3) propose a new method to quantify the PMP uncertainty and compare to the Salas method results; 4) analyze spatial

characteristics of PMP in Brazos River basin; and 5) define the PMP confidence interval for each station.

1.3 Synthetic Probable Maximum Precipitation Storm Design and Uncertainty

PMP values calculated either by meteorological method or statistical method are only the average areal amount of rainfall for a given storm area, storm duration at a particular location at a certain time of a year. To get PMF, a PMS needs to be designed. Comparing different types of temporal design of PMP, Moore et al. (1993) found that the method from HMR 52 (Hansen et al., 1982) was the most conservative one for dam and levee design. Since HMR 51 and HMR 52 are designed by NWS specifically for PMP and PMS studies, we concentrate on how to develop a PMS with the method from HMR 52. HMR 52 provides a stepwise approach to get the temporal and spatial distribution of PMP. The main steps include: 1) refer to historical storms to develop depth-area-duration (DAD) curves and within/without-storm depth-area (WWSDA) relations; 2) retrieve PMP values from HMR 51 and apply them to DAD curves and WWSDA relations to obtain the isohyetal values for all durations of PMP; and 3) arrange rainfall increments in a time sequence to get the hyetographs with a spatial distribution. More detailed steps and methods are described in Chapter III. This study updated the historical storms used to capture the temporal and spatial features of PMS. The new updated records were from around Texas instead of the vast major storms from the east of the 105th meridian. The PMS designed in HMR 52 used 6-hr increment for a

72-hr duration event. In order to improve the accuracy, we downscaled the time step to 1-hr.

As shown in Figure 1, the PMS design procedure involves all kinds of uncertainties, such as uncertainties stemming from the flexibility of arranging the precipitation time sequence, choice of storm shape, storm orientation, time interval, and isohyetal values referring to historical records (as shown in figure 1). Unlike the statistical method, the uncertainty of this deterministic method can only be qualified with numerical sampling, e.g., with Monte Carlo simulation. However, as the middle procedure to derive PMF and uncertainty, Monte Carlo process will lead to a dramatic growth of numerical samples. For example, if 200 mixed sets of parameters (e.g., storm orientation, time interval) were assigned to derive PMS and 200 R-R model parameter sets were assigned to derive PMF, a total of 40000 run times need to be conducted by the R-R model, which is a huge burden. At the same time, even though there were complete reviews on the uncertainty of design rainfall (Al Mamoon and Rahman, 2014), the storm design of PMP has not been fully studied yet. To the authors' judgment, the deterministic procedure provided by HMR 52 managed to obtain the most severe conditions (e.g., orientation, shape, arrangement) to derive PMF. Thus, we assume that those conditions have been met in this study and no uncertainty was considered in the PMS design method.

1.4 Rainfall-runoff Model for Extreme Events with Uncertainty

The designed PMS needs to be routed through an R-R model to get PMF. There are plenty of R-R models to select from but not many studies had focused on extreme event R-R modeling with uncertainty analysis. Thus, this study explored the uncertainty in extreme event R-R modeling, which was then used in deriving PMF with uncertainty.

With increasing frequency of extreme events under changing climate (Ornes, 2018), it is important to understand the features and uncertainties in R-R modeling of extreme events (Wagener and Gupta, 2005; Georgakakos et al., 2004). Meteorologists have attempted to quantify uncertainties in climate models for predicting extreme weather (Gillingham et al, 2018), while hydrologists were more concerned with uncertainties when applying R-R models. Moradkhani and Sorooshian (2009) summarized that the sources of uncertainties in R-R models stemmed from the forcing data, observed system response, imperfection of model structure, and the parameter values resulting from model calibration. For better understanding of the uncertainty sources from a model construction perspective, it may be pertinent to recall the basic steps in building an R-R model: (1) selection of component methods (e.g., loss method, runoff method, and routing method) to construct a model; (2) delineation of watershed characteristics (e.g., soil type, land use type, and impervious percentage) in the area and building of the base model; (3) collection of input data (e.g., precipitation data and discharge records) for calibrating the model; (4) selection of calibration algorithm (e.g., objective function and search algorithm) to calibrate the model; and (5) validation of the model and its application (Singh et al., 2018). Uncertainties embedded in these steps

result in the integrated uncertainty of R-R modeling. Uncertainty analysis frameworks introduced in the hydrologic literature include the Generalized Likelihood Uncertainty Estimation (GLUE) (Beven and Binley, 1992), Bayesian Recursive Estimation (BaRE) (Thiemann et al., 2001), Shuffled Complex Evolution Metropolis algorithm (SCEM) (Vrugt et al., 2003a), multi-objective extension of SCEM (Vrugt et al., 2003b), Dynamic Identifiability Analysis Framework (DYNIA) (Wagener et al., 2003), Maximum Likelihood Bayesian Averaging Method (MLBMA) (Neuman, 2003), dual state-parameter estimation method (Moradkhani et al., 2005a, 2005b), simultaneous optimization and data assimilation algorithm (SODA) (Vrugt et al., 2005), and Sequential Uncertainty Fitting (SUFI-2) (Abbaspour et al. 2004).

The GLUE method for uncertainty quantification has been widely used in hydrologic modeling. It uses the term 'equifinality' and emphasizes hydrological, rather than statistical, arguments about the nature of a model and data errors and uncertainties. The rationale of the GLUE method is that there are many different model structures and parameter sets within a chosen model structure that may be acceptable in reproducing the observed behavior of a watershed system (Beven and Freer, 2001). The popularity of this method can be attributed to its simplicity and its applicability to nonlinear systems, including those for which a unique calibration is not apparent. Since its development, there have been debates that GLUE is not formally Bayesian, resulting in parameter and predictive distributions that are statistically incoherent and unreliable (Mirzaei et al., 2015).

Studies on the uncertainty in R-R modeling using the GLUE method can be categorized into four types, based on temporal and spatial scales: event-based small watershed (e.g., Aronica et al., 2002; Liu et al., 2020), event-based large watershed (e.g., Lehbab-Boukezzi et al., 2016; Fuentes-Andino et al., 2017), continuous small watershed (e.g., Freer et al., 1996; Cameron et al., 1999), and continuous large watershed modeling (e.g., Montanari, 2005). These studies focused on different aspects of the GLUE method, such as general application, method extension and combination, and the impact of underlying assumptions. Extreme flood event modeling involves event-based large watershed modeling, since extreme events usually involve large watersheds, intensive precipitation, and high peak flows. All these features impact the performance and uncertainty of R-R modeling. However, few studies have focused on quantifying the uncertainty with the GLUE method in extreme events modeling. The studies by Lehbab-Boukezzi et al. (2016) and Fuentes-Andino et al. (2017) either simulated relatively small events compared to "extreme" or only reproduced an extreme storm event with uncertainty analysis using the GLUE method. At the same time, uncertainty stemming from the above five steps of building an R-R model has not been implemented within any of the GLUE method applications. Most GLUE applications only executed the Monte Carlo simulation of parameter sets and derived an uncertainty interval of the simulated flow. Few studies have investigated the contribution of each source of uncertainty in the R-R model. For example, Montanari (2005) developed different experiments of synthetic stream flow series to explore how different sources of uncertainty in the GLUE method affected the uncertainty estimation. However, only one

basin in that study was used for data generation and uncertainty sources were not fully considered or were overlapping each other.

The Chapter IV in this study therefore aims to 1) build R-R models for extreme events and quantify the uncertainties using the GLUE method; 2) investigate the different sources of uncertainty associated with modeling of extreme events based on the GLUE method; and 3) apply the PMS derived from Chapter III to the R-R model and quantify the uncertainty. It is noted that no attempt is made to discuss the foundation of the GLUE method nor compare different methods of quantifying the uncertainty of hydrological modeling. Rather, the aim is to understand the R-R model uncertainty of extreme events based on the framework of the GLUE method and investigate the underlying sources of that uncertainty. The study was based on a case study in the Gulf of Mexico region within Texas, United States. The extreme event used for calibration was hurricane 'Harvey', which is considered as the wettest tropical event that ever happened in the United States (Blake and Zelinsky, 2018). Another extreme storm called hurricane Patricia that affected Texas was used to validate the R-R models. It is noted that the performance of the validation period might not be satisfactory, because certain model processes (such as loss rate in the loss method) might change significantly due to the differences between the two events (an extreme event for calibration, and a small extreme event for validation). Data from different sizes of basins and flood events were collected to build the R-R models for extreme events in the study area. Model uncertainties were quantified using the GLUE method and different sources of

uncertainties were compared both inside each basin model and between different basin models.

Above all, the contents of the whole study have been stated. The methods used to realize the specific objectives and results will be discussed in the following chapters.

CHAPTER II

ESTIMATION OF PROBABLE MAXIMUM PRECIPITATION AND UNCERTAINTY*

2.1 Methods and Materials

2.1.1 Probable Maximum Precipitation

Hershfield Method

Hershfield (Hershfield, 1961) proposed a frequency factor-based formula to estimate PMP as

$$PMP = \overline{X_n} + KS_n \quad (1)$$

where $\overline{X_n}$ is the mean of extreme annual precipitation series, S_n is the standard deviation of extreme annual precipitation series, *n* is the sample size, and *K* is the frequency factor.

K was calculated by observing the biggest maximum annual rainfall as (Hershfield, 1961)

$$K = \frac{X_m - \overline{X_{n-1}}}{S_{n-1}} \quad (2)$$

where X_m is the biggest maximum annual rainfall observed in the series, $\overline{X_{n-1}}$ is the mean annual maximum rainfall excluding X_m, and S_{n-1} is the standard deviation of the series excluding X_m. Then, enveloping curves of *K* against $\overline{X_n}$ were constructed by

* Reprinted with permission from "Basin-Scale Statistical Method for Probable Maximum Precipitation with Uncertainty Analysis" by Yu Zhang, Vijay Singh and Aaron Byrd, 2019. Journal of Hydrologic Engineering, 24(2), 04018067, Copyright [2021] by Journal of Hydrologic Engineering, with permission from ASCE.

analyzing data from 2,645 stations in the U.S. and around the world. To draw the enveloping curve, Hershfield plotted each station's $\overline{X_n}$ versus *K*. As an aid in positioning the enveloping lines, Jenning's (1950) enveloping relationship between rainfall and duration was referred. The equation fitted to Jenning's data is:

$$R = 2\sqrt{t} \tag{3}$$

where *R* is the world-enveloping rainfall (inches), and *t* is the duration (minutes). Series of adjustments have been made to the Hershfield method. For example, adjustments factors for mean annual maximum and standard deviation to eliminate the effect of maximum observed rainfall outliers, adjustment due to rainfall observation time interval and adjustment for translating PMP point estimate to areal-average estimate by depth-area-duration relationship have been made. References can be made to the original study of Hershfield and WMO report for details (Hershfield,1961; WMO, 2009). Thus, for each station, PMP can be calculated from equation (1) after each element in the equation being determined.

Proposed Basin-scale Method

To develop the *K* enveloping curve, the proposed basin-scale method assumed that *K* from the target basin (instead of around United States) came from one population, which was a more reasonable assumption than that made by Hershfield. Equations (1) and (2) were used to calculate the basin-scale PMP and *K*, and basin-scale *K* enveloping curve map was made, based on 39 stations in the basin. However, for the basin-scale *K* enveloping curve, it's not appropriate to use the worldwide rainfall-duration relationship because of the scale. Instead, we reorganized the equation of *K* as a function of only $\overline{X_n}$

with the combination of Jenning's relationship. The procedure for developing the equation is as follows:

The coefficient of variation was assumed constant in according with Jenning (1950). Substituting equations (3) and (4) into equation (2) (replacing X_m with *R*, $\overline{X_{n-1}}$ with $\overline{X_n}$, and S_{n-1} with $c\overline{X_n}$), we get the *K* enveloping curve as expressed by equation (5): (note that the exact substitution cannot happen because X_m is not equal to *R*, $\overline{X_{n-1}}$ is not equal to $\overline{X_n}$, and S_{n-1} is not equal to $c\overline{X_n}$ .We assume it is true here only to explore the potential form of *K* against $\overline{X_n}$)

$$S_n = c\overline{X_n} \tag{4}$$

$$K = \frac{2\sqrt{t}}{c\overline{X_n}} - \frac{1}{c} \tag{5}$$

where *c* is the coefficient of variation (constant). For each duration *t*, *K* has a negative power relation with $\overline{X_n}$, however, the exact form of the curve is not known. Therefore, one manually adjusts the lines to fit the data as well as the equation form as closely as possible. After adjusting and plotting, we selected a form with an exponential base, a negative power and a factor as shown in equation (6):

$$K = b\mathrm{e}^{-d\overline{X_n}} \tag{6}$$

where *b*=20 which followed the beginning point of the Hershfield enveloping curve (Hershfield, 1961). To make it as an enveloping curve, *d* should be determined by equation (7):

$$d = min\left(\frac{-\ln\left(\frac{K_O}{b}\right)}{\overline{X_O}}\right) \tag{7}$$

where $min(.)$ is a function of finding the minimum, K_o is the observed *K* for each station, and $\overline{X_O}$ is the observed mean annual maximum rainfall from each station. Because of the limited data samples in the basin, we used the bootstrap method to extend the data base as described in section 2.1.3, which generated extended values of K_o and $\overline{X_O}$ to capture sufficient information for determining the *d* value.

After determining the *d* values for each duration data, the enveloping curves of the *K* values of the basin can be obtained. With *K* being expressed as a function of mean, PMP can then be expressed as a function only related to the mean and standard deviation and this was used to quantify the standard error. The same adjustment procedure as Hershfield method was adopted to develop the basin-scale model, where 2600 square kms scale PMP values were determined from the PMP point estimates.

2.1.2 Probable Maximum Precipitation Uncertainty

Salas Method

Salas et al. (2014) estimated PMP ($\hat{P}$), determined the variance of $\hat{P}$, and then used Chebyshev's inequality to obtain the value of PMP with uncertainty:

$$E(\hat{P}) = E(\overline{X_n}) + KE(S_n) \tag{8}$$

where *E* is the expectation operator;

$$E(\overline{X_n}) = E\left[\left(\frac{1}{n}\right)\sum_1^n X_i\right] = \left(\frac{1}{n}\right)\sum_1^n E(X_i) = \mu \tag{9}$$

in which μ represents the mean of population of X_i, and X_i is the individual annual maximum rainfall, and *n* is the number of annual maximum rainfall values; and

$$E(S_n) = \frac{\Gamma\left(\frac{n}{2}\right)\sigma}{\sqrt{\frac{n-1}{2}}\,\Gamma\left[\frac{n-1}{2}\right]} \tag{10}$$

where σ represents the standard deviation of population of X_i, and Γ is the incomplete gamma function. Equation (9) is based on the assumption of normality of the annual maximum rainfall series.

Substituting equations (9) and (10), equation (8) can be rewritten as:

$$E(\hat{P}) = \mu + K\frac{\Gamma\left(\frac{n}{2}\right)\sigma}{\sqrt{\frac{n-1}{2}}\,\Gamma\left[\frac{n-1}{2}\right]} \tag{11}$$

Now the variance of $\hat{P}$ can be calculated as:

$$Var(\hat{P}) = Var(\overline{X_n}) + K^2 Var(S_n) + 2KCov(\overline{X_n}, S_n) \tag{12}$$

where $Var(\hat{P})$ is the variance of PMP, $Var(\overline{X_n})$ is the variance of the sample mean, $Var(S_n)$ is the variance of the sample standard deviation, and $Cov(\overline{X_n}, S_n)$ is the covariance of sample mean and standard deviation, which equals zero for normal distribution (Kendall, 1963). Each of the elements in equation (12) can be calculated as below:

$$Var(\overline{X_n}) = \frac{\sigma^2}{n} \tag{13}$$

$$Var(S_n) \approx \frac{\sigma^2}{2(n-1)} \tag{14}$$

$$Cov(\overline{X_n}, S_n) \cong 0 \tag{15}$$

Then, the variance of $\hat{P}$ can be expressed as:

$$Var(\hat{P}) \cong \frac{\sigma^2}{n} + K^2 \frac{\sigma^2}{2(n-1)} \quad (16)$$

The standard deviation of $\hat{P}$ is:

$$\sigma(\hat{P}) \cong \frac{\sigma}{\sqrt{n}} \sqrt{1 + \frac{nK^2}{2(n-1)}} \quad (17)$$

Then, PMP along with uncertainty can be calculated as:

$$PMP = E(\hat{P}) \pm m\sigma(\hat{P}) \quad (18)$$

where *m* is a constant, *m*>1 represents the times of variance away from the estimated PMP. Chebyshev's inequality can be applied to PMP as:

$$P\left[E(\hat{P}) - m\sigma(\hat{P}) < \hat{P} < E(\hat{P}) + m\sigma(\hat{P})\right] \gg 1 - \frac{1}{m^2} \quad (9)$$

Salas et al. (2014) assumed *K* as a constant which means it caused no uncertainty and annual maximum rainfall as a population with normal or Gumbel distribution (not described in this study).

Proposed Basin-scale Method

The proposed method considered both the uncertainty caused by the mean and standard deviation of annual maximum rainfall series and the population scale (basin versus global) assumption of the *K* values. We introduced Delta Method (Casella et al., 2002) to calculate the standard error of PMP. Unlike the Salas method, the delta method does not require the assumption of normality of rainfall series. Hershfield assumed the 2,645 stations data from the U.S. and around the world came from the same population. He found *K* to follow a skewed distribution. It is possible that for a basin-scale population, *K* may not necessarily follow an extreme type distribution, such as Gumbel,

generalized extreme value (GEV), etc. Strictly speaking, even *K* values from different stations in a basin cannot be assumed to be from the same population because of meteorological and geological differences. Instead, we focused on only the enveloping curve of *K* for the basin (as discussed in section 2.1.1) and estimated the standard error of PMP for each station. Then, the standard error was obtained with the delta method as below:

For $\hat{P} = g(\overline{X_n}, S_n^2)$, where $g(x, y)$ is a function of mean and standard deviation, after substituting *K* into equation (1), the variance of PMP by the delta method was defined as:

$$Var(\hat{P}) \approx \left(\frac{\partial g}{\partial x}\right)^2 Var(\overline{X_n}) + 2\left(\frac{\partial g}{\partial x}\right)\left(\frac{\partial g}{\partial y}\right) Cov(\overline{X_n}, S_n^2) + \left(\frac{\partial g}{\partial y}\right)^2 Var(S_n^2) \quad (20)$$

All the elements in equation (20) are defined as below:

$$g(x, y) = be^{-dx}\sqrt{y} + x = be^{-d\overline{X_n}}S_n + \overline{X_n} \quad (21)$$

$$\frac{\partial g}{\partial x} = 1 - bde^{-d\overline{X_n}}S_n \quad (22)$$

$$\frac{\partial g}{\partial y} = \frac{be^{-d\overline{X_n}}}{2S_n} \quad (23)$$

The derivatives were evaluated at the estimates for μ and σ^2 with $\overline{X_n}$ and S_n as:

$$Var(\overline{X_n}) = \frac{\sigma^2}{n} \quad (24)$$

$$Var(S_n^2) = \frac{1}{n}\left(1 - \frac{1}{n}\right)^2 \left(M_4 - \left(1 - \frac{2}{n-1}\right)\sigma^4\right) \quad (25)$$

$$M_4 = E((x - \mu)^4) \approx \frac{1}{n}\sum_{1}^{n}(x_i - \overline{X_n})^4 \quad (26)$$

$$Cov(\overline{X_n}, S_n^2) = \frac{1}{n}\left(1 - \frac{1}{n}\right) M_3 \tag{27}$$

$$M_3 = E((x-\mu)^3) \approx \frac{1}{n}\sum_{1}^{n}(x_i - \overline{X_n})^3 \tag{28}$$

Substituting equations (21)-(28) into equation (20) to get the variance of PMP for each station. To check the reliability of this method, the bootstrap method was also used to generate the sufficient amount of PMP values for each station as described in section 2.1.3. The variance of the generated PMP values was compared with the results from equation (20).

2.1.3 Bootstrap Method for Probable Maximum Precipitation and Uncertainty

To extend the data base for developing the basin-scale *K* enveloping curve (section 2.1.1), evaluate the reliability of our proposed method for quantifying uncertainty (section 2.2.2), and explore the distribution of *K* and PMP at each station, we used the bootstrap method to resample from the original observations. The bootstrap method, introduced by Efron (1979), is a resampling technique and doesn't require information of the true distribution (Joshi, et al.,2006). The general procedure for this study is as below:

For each station *S*, let ($X_{S,1}$,⋯, $X_{S,n}$) be the record of annual maximum rainfall for a fixed duration, where *n* is the record length of station *S*. Let *h* be the number of bootstrap samples to be used.

a) For each h =1, ⋯, N and each station S, generate $X^*_{S,h}$= ($X_{S,1,h}$,⋯, $X_{S,n,h}$) values randomly sampled (with replacement) from the original record.

b) Compute statistics $\overline{X^*_{S,h}}$ (sample mean), $S^*_{S,h}$(sample standard deviation), $K^*_{S,h}$ (K value of new sample h of station S, this value is also used for building the basin-scale K enveloping curves)

c) For each h, follow steps in section 2.1.1, create an enveloping curve map for the basin; in other words, h maps will be created.

d) Compute $K_{S,h}$for each station S, and sample h according to each map from part c)

e) Estimate $\hat{P}_{S,h}$=$K_{S,h}S^*_{S,h} + \overline{X^*_{S,h}}$ for each station S, sample h

f) Find the sample standard deviation of the values ($\hat{P}_{S,1}$, ⋯,$\hat{P}_{S,N}$) which is the estimated standard error for $\hat{P}_S$.

In the case study, 1000 (N=1000) bootstrap samples were generated by resampling from the original sample (annual maximum rainfall series) repeatedly. We used the bootstrap method based on Matlab software (Matlab 2017a). The syntax can be written as:

$$[bootstat, bootsam] = bootstrp(h, @mean, data) \quad (29)$$

$$newsam = data(bootsam) \quad (30)$$

where *bootstat* was the output of the targeted function value (e.g. the mean of the sample), *bootsam* contained indices of the values that were drawn from the original data sets to constitute the corresponding bootstrap sample, *bootstrp* was the built-in function named in Matlab to call the bootstrap method. h represented the resample number.

@mean was the syntax to call for the targeted function value. *Data* was a column of initial observed records. *Newsam* was the new resampled values from the original data. After applying the bootstrap method to the study area records, we got the numerical values of the variance of PMP for each station. Then we compared the results with direct estimation results.

Bootstrap method also provided a way to study the potential distribution of PMP values. With *h* PMP values at each station, frequency analysis could be conducted. The underlying distribution was an important information because it could be used to make statistical inferences. For example, if PMP followed a normal distribution, confidence interval or hypothesis test for PMP values can be derived from the following equation with the PMP estimate and standard error assumed to be known.

$$CI_{PMP} = \bar{X} \pm t_{\alpha/2,n-1} \cdot \frac{s}{\sqrt{n}} \tag{31}$$

where CI_{PMP} is the confidence interval of PMP, $\bar{X}$ is the sample mean of PMP which can be replaced with PMP calculated from basin-scale method for each station, $t_{\alpha/2,n-1}$ is the *t* distribution coefficient, α is the confidence level, *s* is the standard error which could be replaced with $\sqrt{Var(\hat{P})}$, and *n* is the sample size which could be replaced by the annual maximum rainfall series size. (We didn't use the bootstrap sample size because it could be any number, while annual maximum rainfall sample size was a good choice because we could assume that with each year's data added to the series, a new PMP estimation could be generated, which means *n* PMP values in the sample.)

2.2 Data

The study area was Brazos River basin which extends from eastern New Mexico to southeastern Texas up to the Gulf of Mexico. The basin has a length of approximately 1030 kms and a width varying from about 113 kms in the High Plains in the upper basin to a maximum of 177 kms in the vicinity of the city of Waco to about 16 kms near the city of Richmond in the lower basin. The basin drainage area is approximately 117,000 square kms, with about 111,000 square kms in Texas and the remainder in New Mexico. (Wurbs et al., 1988). 39 rainfall stations with average records of 50 years long were analyzed. Hourly rainfall data were collected from the NCDC NOAA website, then 6 and 24-hour duration rainfall data were generated (https://www.nacd.noaa.gov/cdo-web/). The average annual maximum rainfall (all durations) showed a declining trend from southeast to northwest of the basin. For each station in the basin, the distribution of the annual maximum rainfall series was either slight or heavy skewed, which corresponded to the extreme value characteristics. The results are not shown here and the effect of characteristics was not considered at this time.

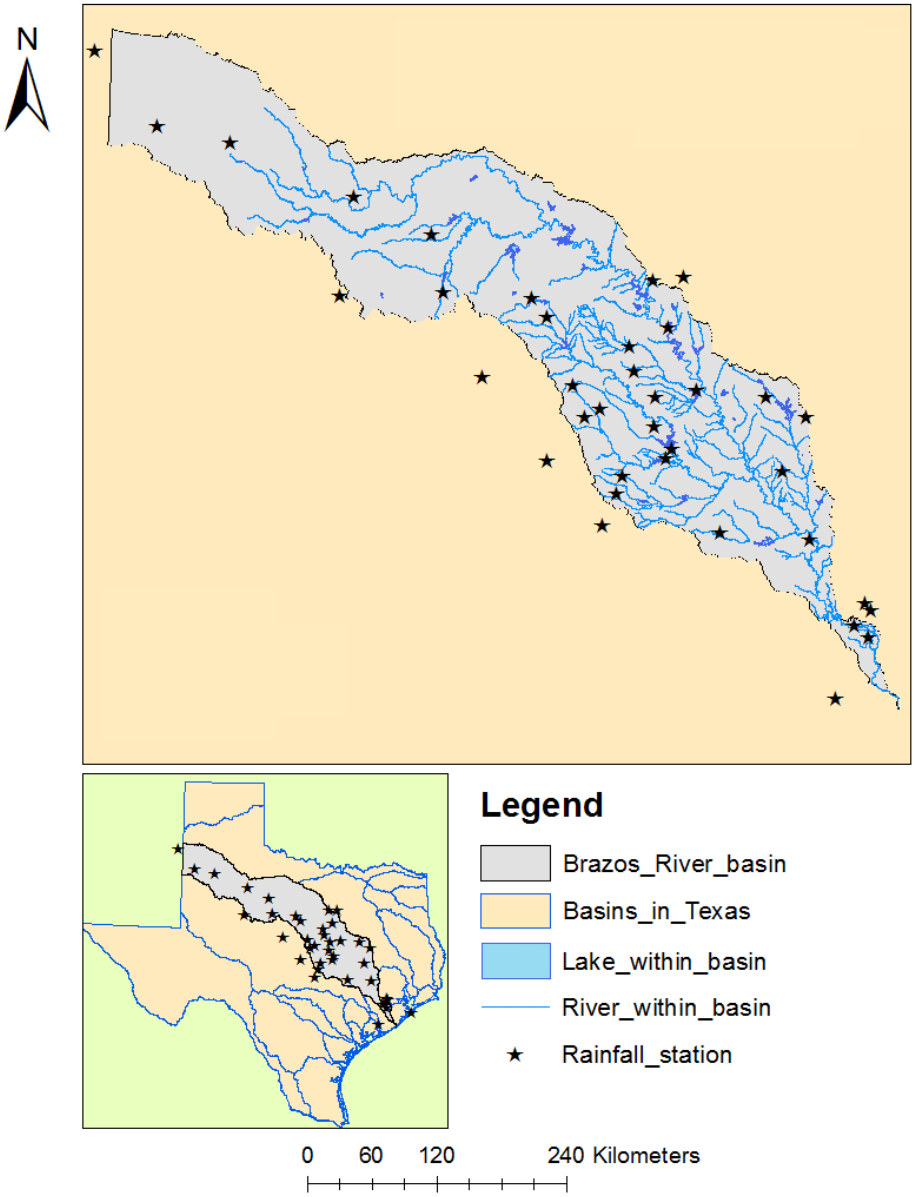

Figure 2 PMP study area: Brazos River basin

2.3 Results and Discussion

2.3.1 Basin-scale K Enveloping Curve

In section 2.1.1 we discussed the method to create a basin-scale *K* value

enveloping curve. Figure 3 shows the results and compares the basin-scale curves with Hershfield curves. The original data of 39 *K* values were used for 1-hour duration, while the procedure described in section 2.1.3 was used to generate 6-hour and 24-hour *K* curves for the basin-scale model [Note: 6-hour and 24-hour rainfall records were generated from the 1-hour data.]. Hershfield curves were recreated from his original paper and represented by the dashed lines. The solid lines are basin-scale curves and the dot-dashed lines are curves from only 39 original values. The *d* values from different methods are shown in table 1. The scale of the curves (gap between 1-hour and 24-hour duration lines) of Hershfield is significantly bigger than that of basin-scale original curves, while with the bootstrap generated curves the gaps were consistent. Even though the Hershfield curves for each duration were higher than those from both the original and bootstrap curves (which made sense because Hershfield samples were from all around the U.S., and basin-scale samples were only from part of the U.S.), the gaps should be consistent. It's not hard to predict that because of the difference of the curves, there will be differences in PMP values between basin-scale and Hershfield method.

Table 1 *d* values from different methods

Duration	Basin-scale original	Hershfield	Basin-scale bootstrap
PMP_01	0.0260	0.0139	0.0153
PMP_06	0.0151	0.00518	0.00930
PMP_24	0.00923	0.00255	0.00632

Note: PMP_01, PMP_06 and PMP_24 are 1-hour, 6-hours and 24-hours durations PMP respectively.

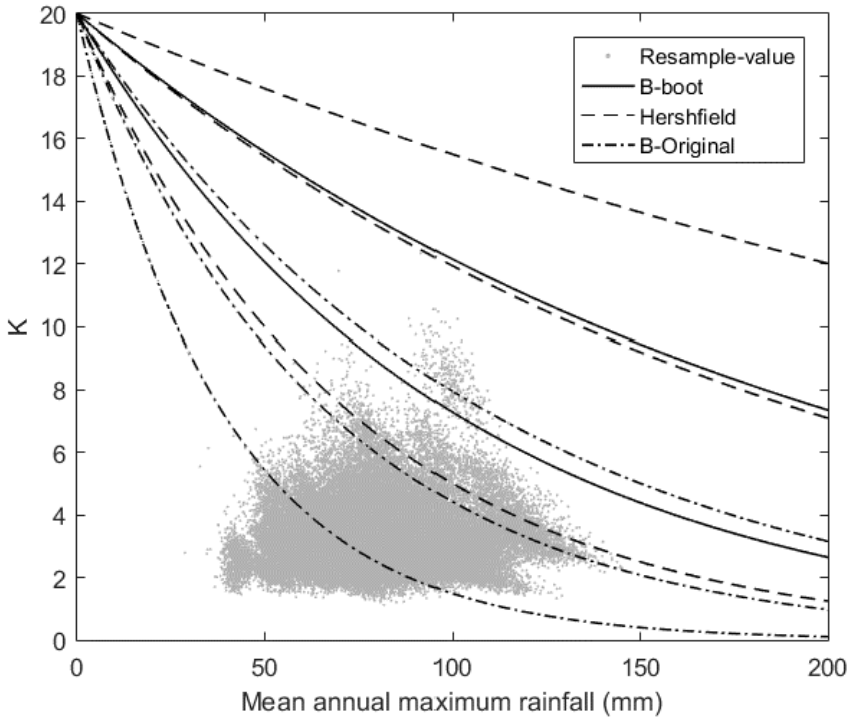

Figure 3 Basin-scale *K* values enveloping curve vs. Hershfield *K* values curve (B-boot represents basin-scale curves generated from bootstrap samples, Hershfield represents curves recreated from Hershfield original works, B-Original represents basin-scale curves derived from only original samples. For each group, curves from bottom to top represent 1-hour, 6-hour and 24-hour duration, respectively.)

2.3.2 Comparison of Probable Maximum Precipitation Values

Texas Commission on Environmental Quality (TCEQ) published a report (2016) about calculating the PMP values in Texas using a deterministic method with meteorological records (Bill K. et al., 2016). This paper calculated 2600 square kms scale general storm PMP values for each station using the method from the report, and compared with basin-scale and Hershfield results. From equations (10) and (11), we noticed that the PMP values calculated by Salas method were very close to those of the Hershfield method (e.g., for n=31, 51 and 81, the results in equation (11) were all very

close to Hershfield results), so we didn't include it into comparison. Table 2 shows all the PMP values from each method. Figure 4 shows how differences occurred individually between different methods.

1-hour duration PMP from both the basin-scale and Hershfield method showed higher values than the TCEQ results. For 6-hour and 24-hour durations, basin-scale values were more consistent with the TCEQ values, while the Hershfield values were much higher (The slope of the guide line in figure 4 is 1). It is worth mentioning that none of the results from any method was the true value of PMP; the deterministic results were adopted by TCEQ, because deterministic results were based on a more reliable method and showed more accuracy (WMO, 2009). Even though the difference between statistical and deterministic results were not negligible, basin-scale results apparently improved over the Hershfield method results. The differences between basin-scale and Hershfield PMP values were caused by the difference of *K* values. The average improvements of the difference percentages for 1-hour, 6-hour and 24-hour durations were 53.84%, 81.04% and 72.60%, respectively. Overall, the Hershfield results were more conservative, while basin-scale results were more consistent with the TCEQ results.

Table 2 Average PMP values for Brazos River basin from each method

Method_duration	TCEQ_1h	TCEQ_6h	TCEQ_24h	Hershfield_1h	Hershfield_6h	Hershfield_24h	Basin-scale_1h	Basin-scale_6h	Basin-scale_24h
Average PMP	98.1	321.0	544.2	270.8	436.5	647.7	177.8	342.9	515.9

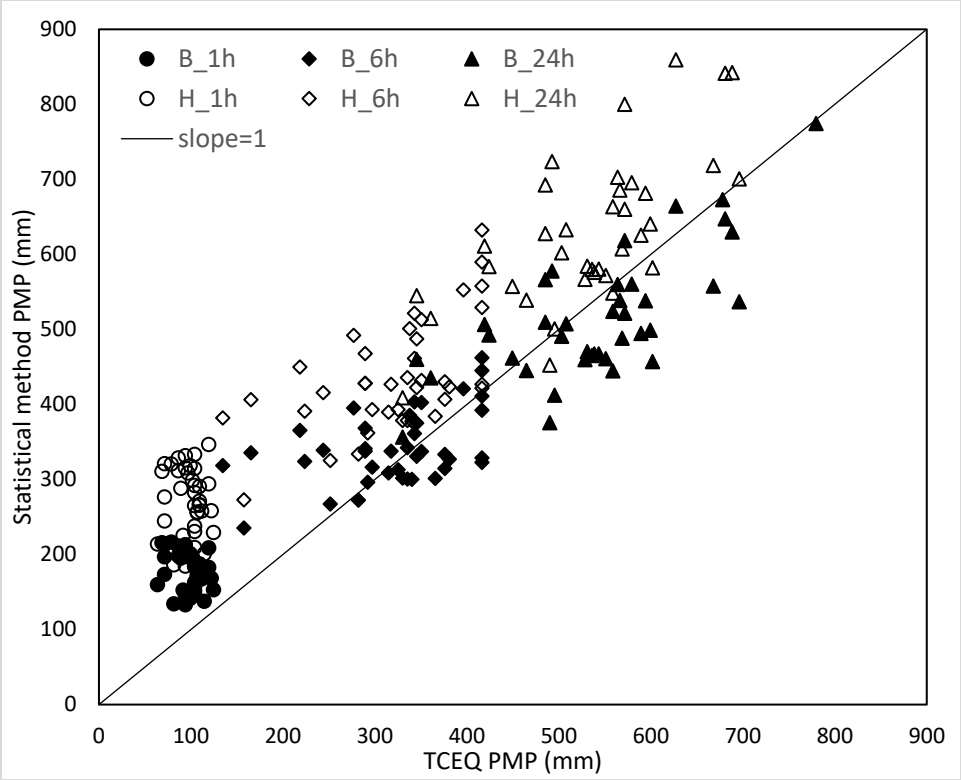

Figure 4 Statistical method PMP vs. TCEQ deterministic method general storm PMP (solid points represent basin-scale results, hollow points represent Hershfield results)

2.3.3 Probable Maximum Precipitation Uncertainties

Basin-scale method quantified uncertainties caused by K, $\overline{X_n}$, and S_n without making any assumptions about distributions of the annual maximum rainfall series, and K values were calculated from the basin enveloping curve. Salas method used Hershfield K enveloping curve and assumed normally distributed rainfall series. It also numerically solved the problem using Monte Carlo simulation with the Gumbel distribution assumption on the rainfall series. Table 3 shows the results of the standard error of PMP by three different methods. As duration became longer, the standard error for all the

three methods tended to be bigger, because the PMP values also followed the same pattern. On average, the bootstrap values were the largest of the three and the Salas values were the smallest. The differences between the delta values and bootstrap values and between the Salas values and bootstrap values for each duration were 10.05%, 10.35%, 19.02% and 25.59%, 20.06%, and 27.95%, respectively. The average percentage of standard error of the PMP estimate for the basin-scale method of all durations was 10%.

Figure 5 shows the difference of the standard errors by the three methods for each station. Surprisingly, the delta and bootstrap method values were highly consistent (The slope of the guide line in figure 5 is 1) which showed that the delta method was valid for the basin-scale model because each standard value from bootstrap method was from 1000 resamples, which was quite representative. The reason why Salas values were relatively small was that the normality assumption ignored the correlation between standard deviation and mean, and the uncertainty caused by *K* was not included.

Table 3 Standard error of PMP by different methods

	Salas_1h	Salas_6h	Salas_24h	Delta_1h	Delta_6h	Delta_24h	Bootstrap_1h	Bootstrap_6h	Bootstrap_24h
average	13.3	31.4	45.8	14.6	34.6	54.6	16.7	37.7	58.7

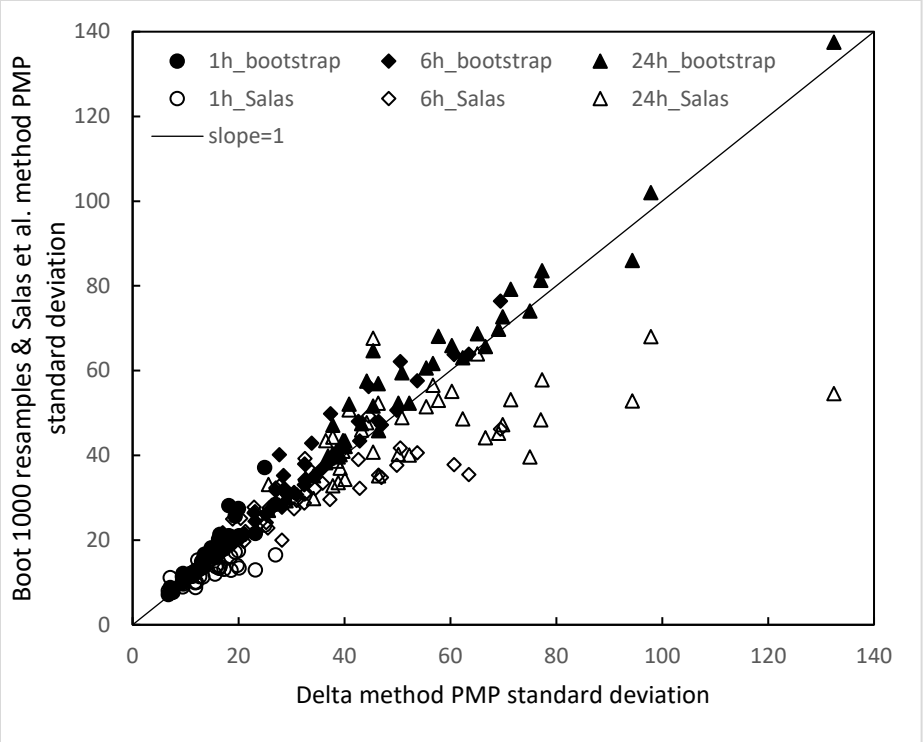

Figure 5 Different methods PMP standard error

2.3.4 Spatial Distribution of Probable Maximum Precipitation

With PMP point estimation and depth-area-duration transformation, basin area PMP values were interpolated using the inverse distance weighting method in Arc-GIS map. The spatial distribution of Hershfield and basin-scale results were highly consistent, because the main cause of difference in PMP values was *K*, while the pattern of enveloping curves of *K* were consistent, even though the magnitudes were different. The TCEQ values from figure 6(a)-(c) showed an obvious declining trend from east coast to west (in land) for all durations, because the deterministic method relied on meteorological characteristics which were related to climate divisions. The grids used in the deterministic method also contributed to the smoothly changing trend of the TCEQ values. The statistical method

values of 6-hour and 24-hour durations showed similar trends, while the distribution of 1-hour duration values was quite different from the deterministic method. Because in reality, extreme events could happen anywhere especially for short duration events which had more uncertainties than long duration events. For example, figures 7(a) and 8(a) show that there were higher PMP values in the upper basin for 1-hour duration, but the storms wouldn't last long as figures 7(b) and 8(b) show lower PMP values for 6-hour duration in the same area. This means local climate features had more effects on longer duration storms as figures 7(c) and 8(c) show similar trends with figure 6(c). At the same time, storms were not only boarding from east coast but also from the south coast to the inner part of Texas (Roth, 2010).

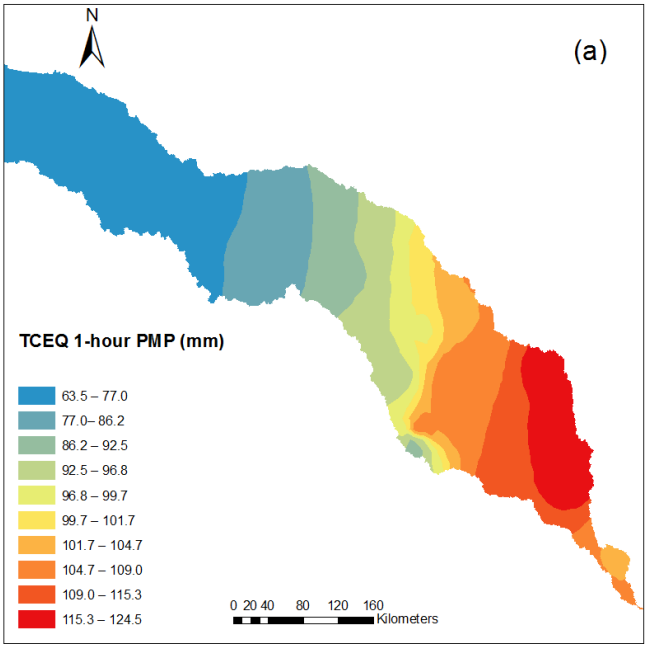

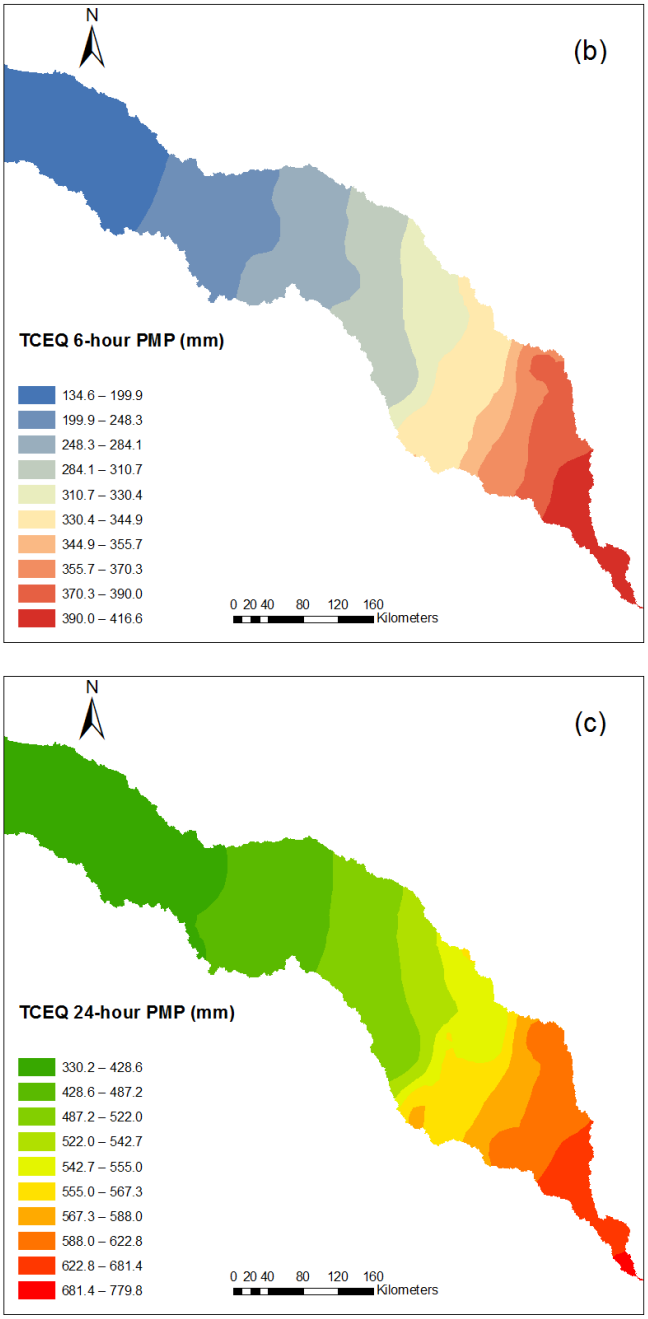

Figure 6 Spatial characteristics of TCEQ PMP of all three durations

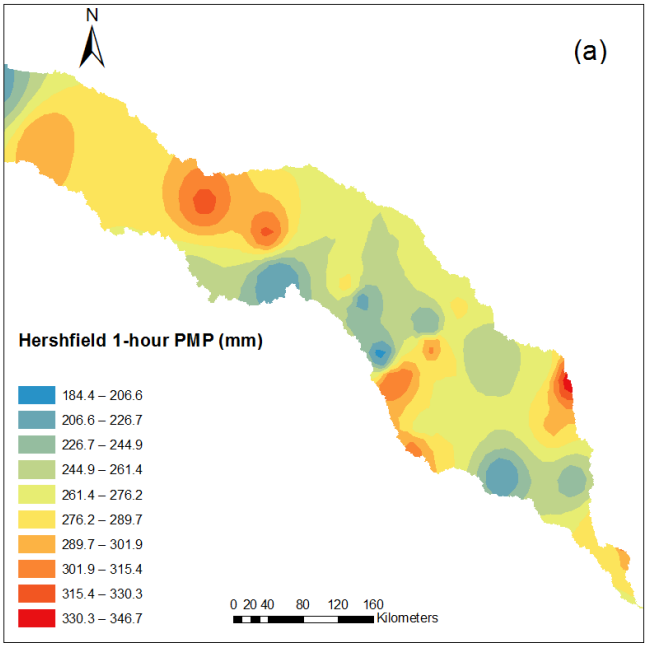
N
(a)
Hershfield 1-hour PMP (mm)
184.4 – 206.6
206.6 – 226.7
226.7 – 244.9
244.9 – 261.4
261.4 – 276.2
276.2 – 289.7
289.7 – 301.9
301.9 – 315.4
315.4 – 330.3
330.3 – 346.7
0 20 40 80 120 160
Kilometers

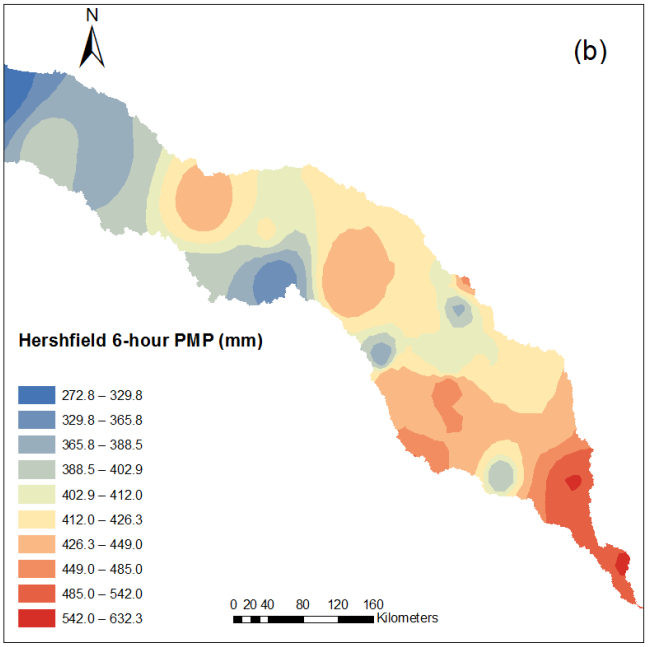
N
(b)
Hershfield 6-hour PMP (mm)
272.8 – 329.8
329.8 – 365.8
365.8 – 388.5
388.5 – 402.9
402.9 – 412.0
412.0 – 426.3
426.3 – 449.0
449.0 – 485.0
485.0 – 542.0
542.0 – 632.3
0 20 40 80 120 160
Kilometers

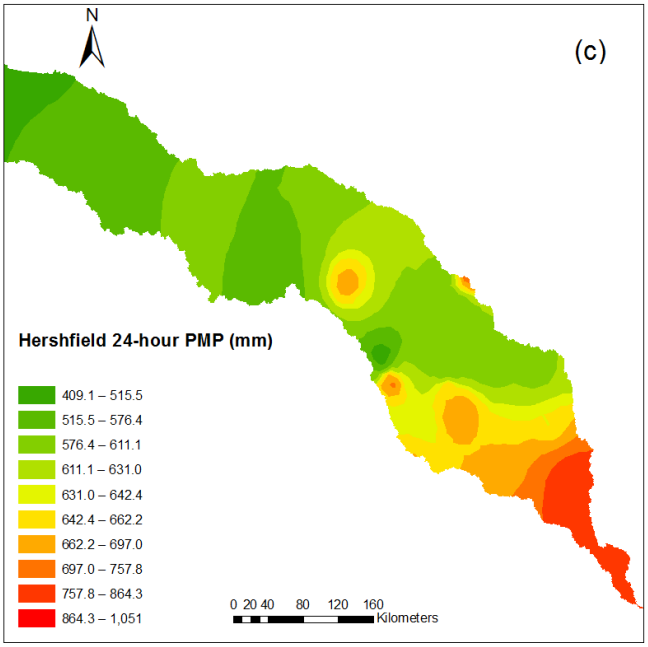

Figure 7 Spatial characteristics of Hershfield PMP of all three durations

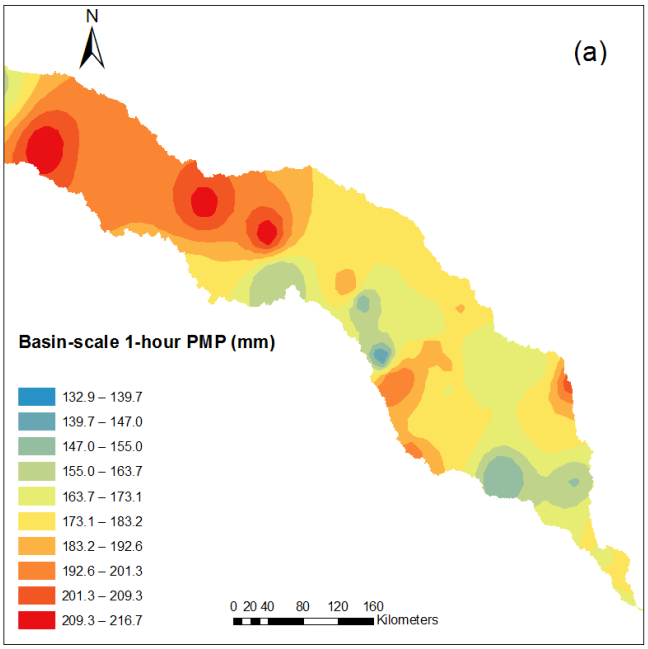

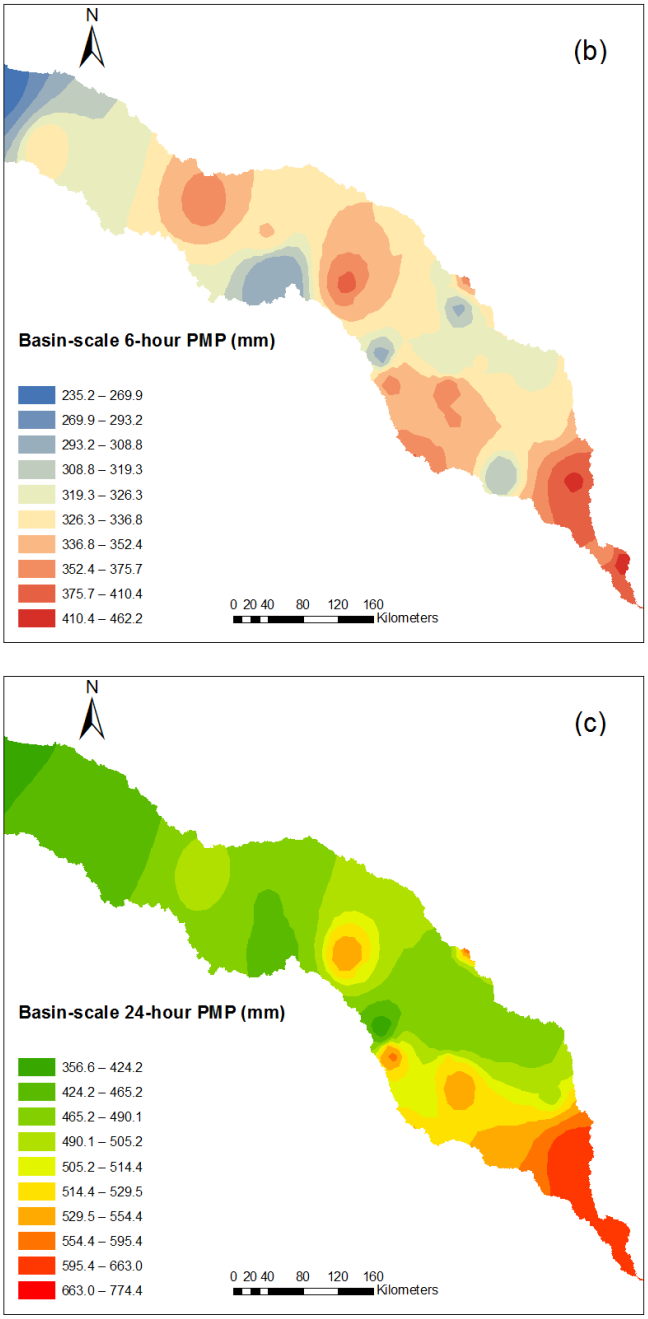

Figure 8 Spatial characteristics of basin-scale PMP of all three durations

2.3.5 Frequency Analysis and Application of Uncertainty

For estimating PMP with the statistical method, the standard error was nearly

10% of the amount of PMP value. From frequency analysis, uncertainties can be quantified along with PMP values. It was not possible to analyze PMP frequency for each station since one station's data could only generate one PMP value. However, the bootstrap method sufficiently generated resamples of the original data set. For example, 1000 resamples were generated for each station's data which led to 1000 PMP values for each station. Thus, PMP frequency analysis was done through 39 stations for each duration. Figure 9 shows that in most cases PMP followed the normal distribution at each station. Thus, with this information, one could combine PMP estimate and standard error with the normal distribution to make statistical inferences. As described in section 2.5, 95% confidence interval for PMP was calculated. Figure 10 shows that even though the PMP magnitudes were different for different durations, the percentages of confidence interval to PMP values were similar. On average, the percentages were 4.59%, 5.69, and 5.90%, respectively. For decision makers, it is more conservative to choose the upper bound of PMP as a design limit.

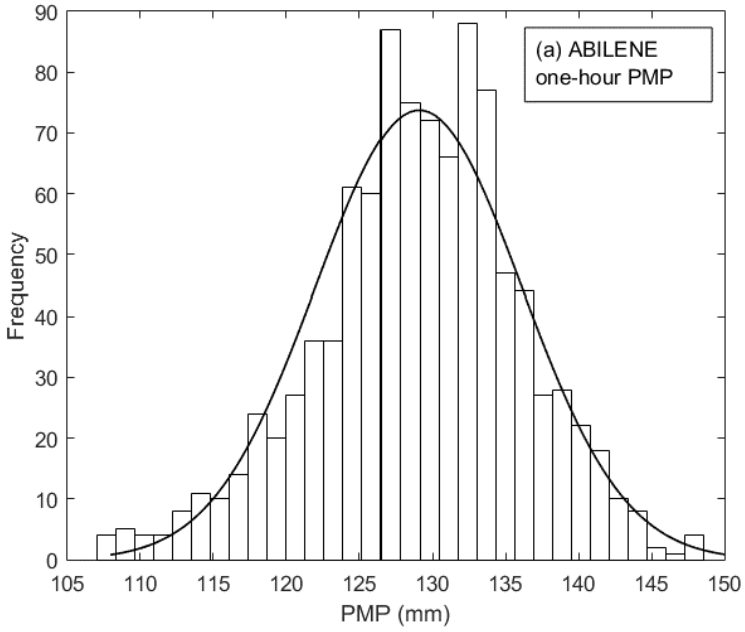
(a) ABILENE
one-hour PMP
Frequency
PMP (mm)
0
10
20
30
40
50
60
70
80
90
105
110
115
120
125
130
135
140
145
150

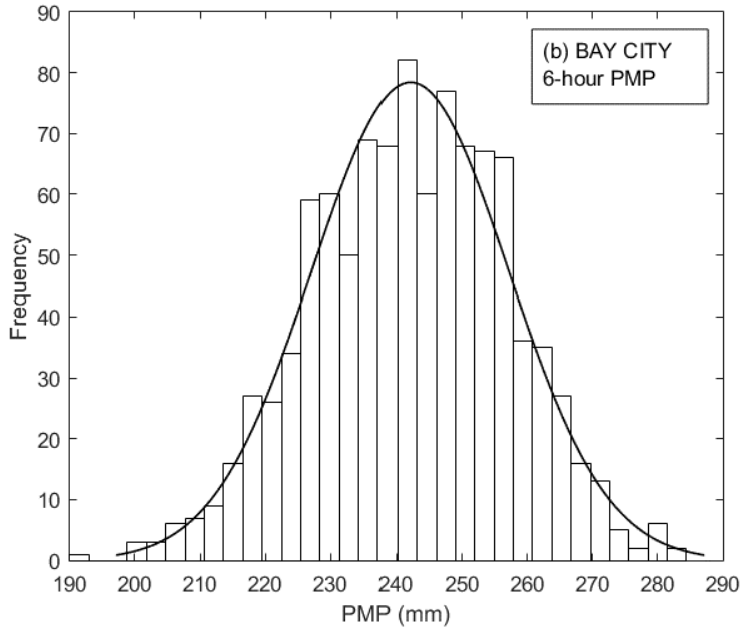
(b) BAY CITY
6-hour PMP
Frequency
PMP (mm)
0
10
20
30
40
50
60
70
80
90
190
200
210
220
230
240
250
260
270
280
290

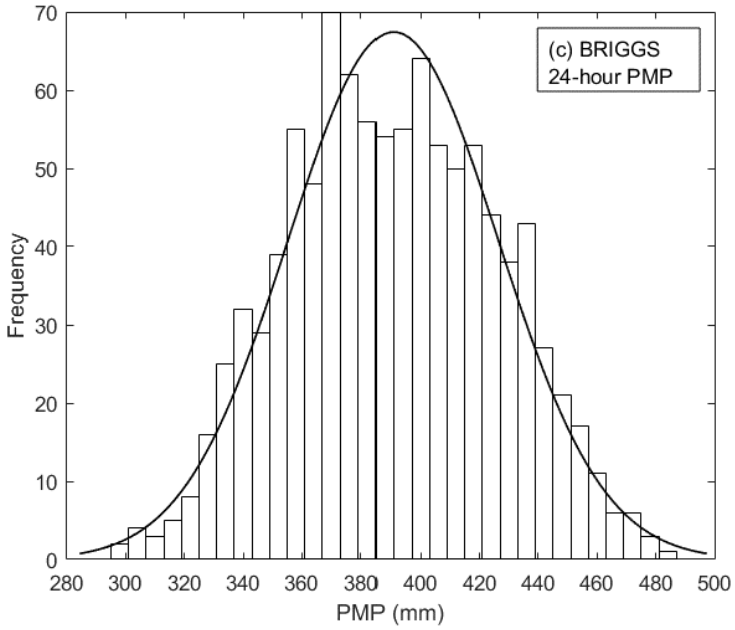

Figure 9 PMP histogram with normal distribution fitted for all durations from randomly selected stations

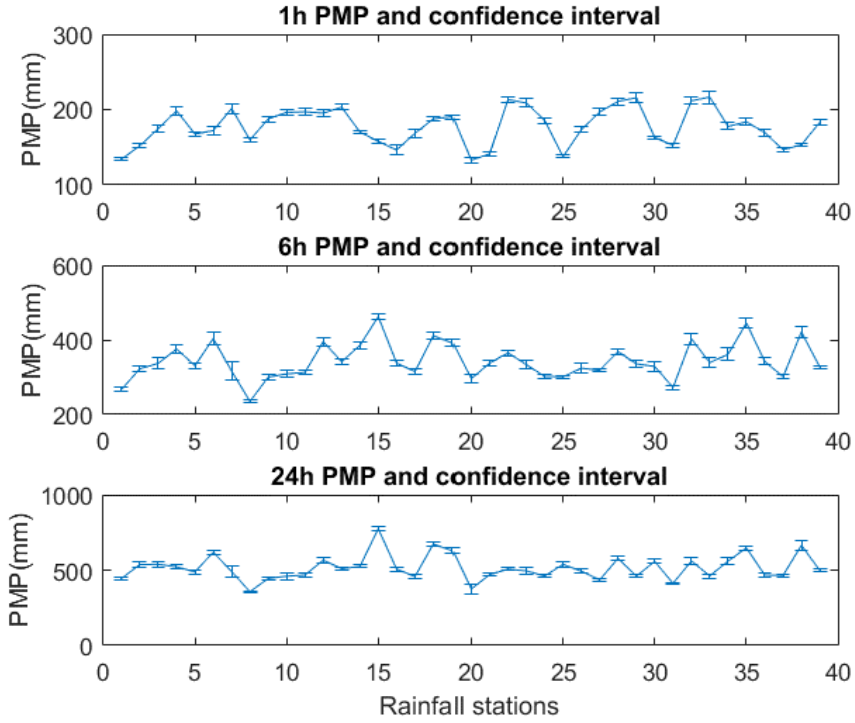

Figure 10 PMP with 95% confidence intervals for all durations of 39 stations

CHAPTER III

PROBABLE MAXIMUM STORM DESIGN WITH HMR 52

3.1 Methods and Materials

3.1.1 Temporal Distribution

In many applications, the definition of PMP for 6-hour is sufficient. Thus, a plot of PMP depths of 6-, 12-, 24-, 48- and 72-hour durations against duration joined by a smooth curve can be used to define PMP for all durations between 6 and 72 hours. For our study case, to improve accuracy, 1-hour increment is used. A 72-hour duration storm is conducted. In addition to those rainfall depth magnitudes, it is necessary to define rainfalls with time which reflect the order of which increments happen in the time sequence (hyetograph). Accumulated rainfall plotted against time from the storm beginning is called a mass curve of rainfall. It represents the rainfall time sequence of the actual storm. HMR 52 provides observed chronological sequences of 6-hour increments in major storms from the east of the 105th meridian. Our study updated the records of major storms which focused on around Texas and ranged from 1899-2015. It showed differences of structures in the sequence between tropical and non-tropical storms, but it suggested not to distinguish time sequences for PMP by storm type, because the PMP in coastal regions may be produced by a complex weather situation that is a mixture of both tropical and non-tropical influences (Hansen et al., 1982). Suggestions for arranging a PMP sequence are as below:

a) Arrange the individual 6-hour (1-hour duration increment is specified for our study) increments such that they decrease progressively to either side of the greatest 6-

hour increment. This implies that the lowest 6-hour increment will be at either the beginning or the end of the sequence.

b) Place the four greatest 6-hour increments at any position in the sequence except within the first 24-hour period of the storm sequence. Studies show that the maximum rainfall rarely occurs at the beginning of the sequence.

A possible sequence is shown in Figure 11.

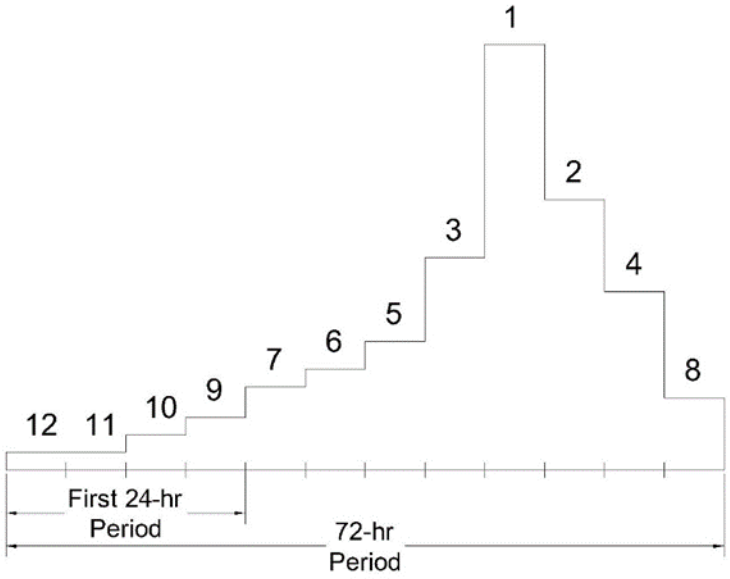

Figure 11 Schematic example of one temporal sequence allowed for 6-hour increments of PMP. (Recreated from HMR 52 figure 3, Hansen et al., 1982)

3.1.2 Spatial Distribution

The two main considerations for the spatial distribution of PMP are the shape (including the orientation) of the pattern and the number and magnitude of isohyets

within the pattern. Another consideration like the area of PMP pattern applied to drainage also needs to be clarified. It needs to be noted that the discussion of pattern placement in this report is primarily directed at drainage areas that are not affected by orographic influences.

Shape and Orientation of the Pattern

After studying 53 major rainfall storms, a shape of ellipse was found to be fit for most of the storms. For the shape ratio of the ellipse, a ratio of major to minor axis of 2.5 to 1 is recommended for the distribution of all increments of precipitation over drainage areas in the non-stippled zones east of the 105th meridian. Figure 12 shows a standard pattern with a scale of 1:1000000, which can be applied to different drainage areas with some transformation. It is also recommended to center the pattern over a drainage area to obtain the hydrologically most critical runoff volume. It is noted that in HMR 52, this pattern was only applied to the first three greatest 6-hour increments of PMP, and a uniform distribution of PMP throughout the area was recommended for the remaining 6-hour increments of PMP in the 3-day storm, while in our study, the stacked isohyetal pattern was applied to each 1-h increment.

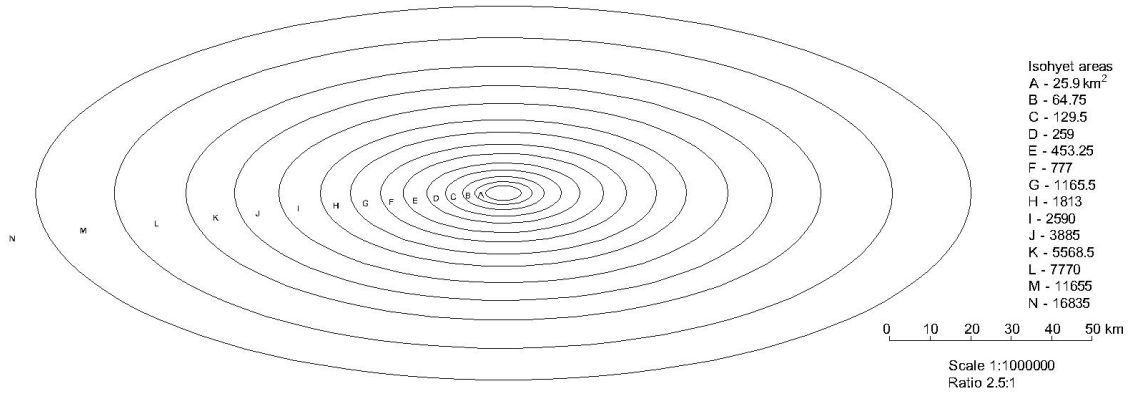

Figure 12 Standard isohyetal pattern recommended for spatial distribution of PMP east of the 105th meridian. (Recreated from HMR 52 figure 5, Hansen et al., 1982)

The orientation of the PMP pattern is not always consistent with the drainage orientation. HMR 52 studied historical storms and gave a generalized pattern orientation map (refer to HMR 52 Figure 8) which attempted to match as many of the storm orientations as possible and yet maintain some internal consistency regarding gradients and smoothness. It is unrealistic to expect that the orientation map is without error and that PMP at any location is restricted to only one orientation. Thus, a range of ±40º centered on the value read from the orientation map will result in a full PMP. In other words, whenever the pattern best fits the drainage area for which PMP is determined has an orientation that falls within 40º of the orientation obtained for that location (from Figure 12), full PMP is used. If a difference is more than 40º, adjustment should be referred to from an adjustment factor map (refer to HMR 52 Figure 10).

Magnitude of Isohyets

HMR 52 recommended distributing incremental PMP for only the three greatest 6-hour PMP increments. First, a within/without-storm average ratio map was developed

for the first 6-hour increment (similar procedure can be applied to second and third increment) as shown in Figure 13. The data used in developing this map are from historical extreme storms. (In HMR 52, data from 29 storms were used). For example, for 25.9 km^2, divide the 25.9-, 518-, 2590-, 12950-, 25900- and 51800-km^2 depths by the 25.9 km^2 depth. Then, form all the ratios for 518 km^2 and so on to the 51800-km^2 ratios. Those within/without-storm average ratios are given as a percent of the respective standard area size value. Second, for a specific location chosen from HMR 51, the PMP values from different area sizes of a particular duration can be read, (in HMR 52, a case location was chosen at 37ºN, 89ºW), apply Figure 13 to storm area averaged 6-hour PMPs for various area sizes (referred to HMR 51), a set of curves can be obtained as shown in Figure 14. This figure gives a plot of the within/without-storm average precipitation relative to area size, which is the within/without-storm depth-area relation (WWSDA) map. To use Figure 14, consider PMP for a particular area size, e.g., 2590 km^2, read the ordinate of 2590 km^2 on the solid line, 393.7 mm. (Note: all these rainfall values read from the figure are areal average rainfall, not the magnitudes of an isohyet.). To determine the corresponding precipitation during this PMP storm for any smaller (larger) area size in that 2590 km^2 PMP pattern, follow the short-dashed (long-dashed) curves from the point of PMP. Third, the isohyetal profile was built from Figure 14 with a reverse process generally followed for deriving DAD curves from an isohyetal profile. The process was briefly outlined in the Manual on Estimation of Probable Maximum Precipitation (PMP) (WMO-No. 1045, 2009, page31-33). The isohyetal profile at location 37ºN, 89ºW is shown in Figure 15. To apply Figure 15 for a PMP pattern of

2590 km^2, e.g., enter the abscissa at each of the isohyets and move vertically to intersect the curve for 2590 km^2. Then, move horizontally to the left to read the respective value of the isohyet. At last, a nomogram for isohyetal values was created covering PMP for all locations. We did not include the nomogram, since we only focused on the case study area. It was done by converting Figure 15 to a percentage of the greatest 6-hour increment of PMP (the same as the 6-hour PMP). For example, the 2590 km^2 area averaged 6-hour PMP is 393.7 mm, the isohyetal value for the C isohyet is 520.7 mm. From Figure 15, dividing 520.7 by 393.7 gives roughly 132 percent. For each standard area size, we have a percentage for the C isohyet. Plot the area size against the percentage for the C isohyet, and the same procedure was used for other isohyets. Detailed procedure and results are shown in HMR 52. For this study, we only need the isohyet values (shown in Figure 15 as an example) derived from the updated storm records and PMP values from Chapter II.

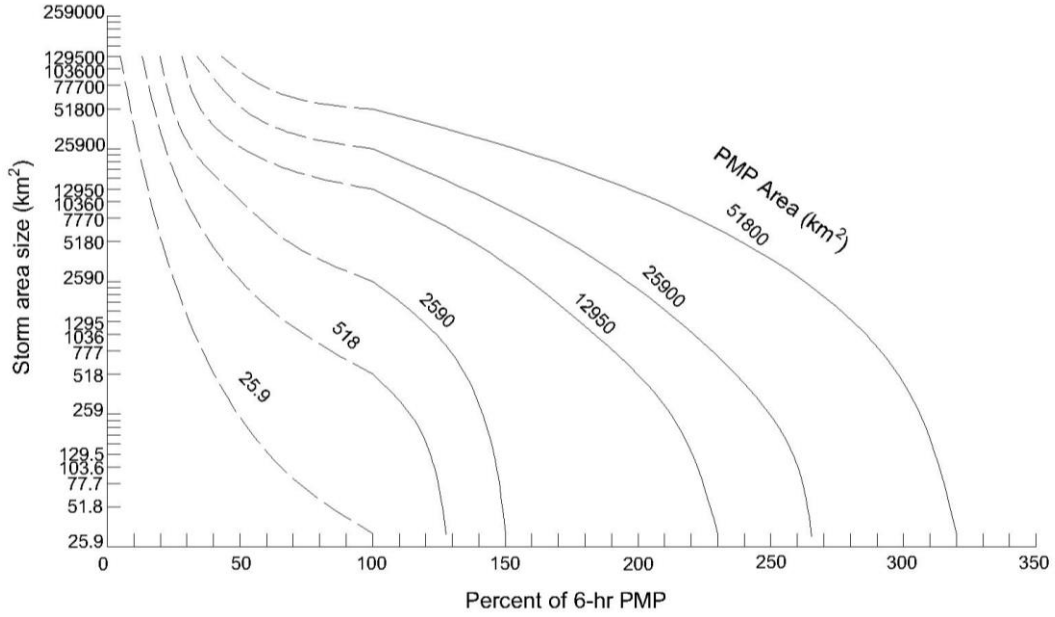

Figure 13 6-hour within/without-storm average curves for standard area sizes. (Recreated from HMR 52 figure 13, Hansen et al., 1982)

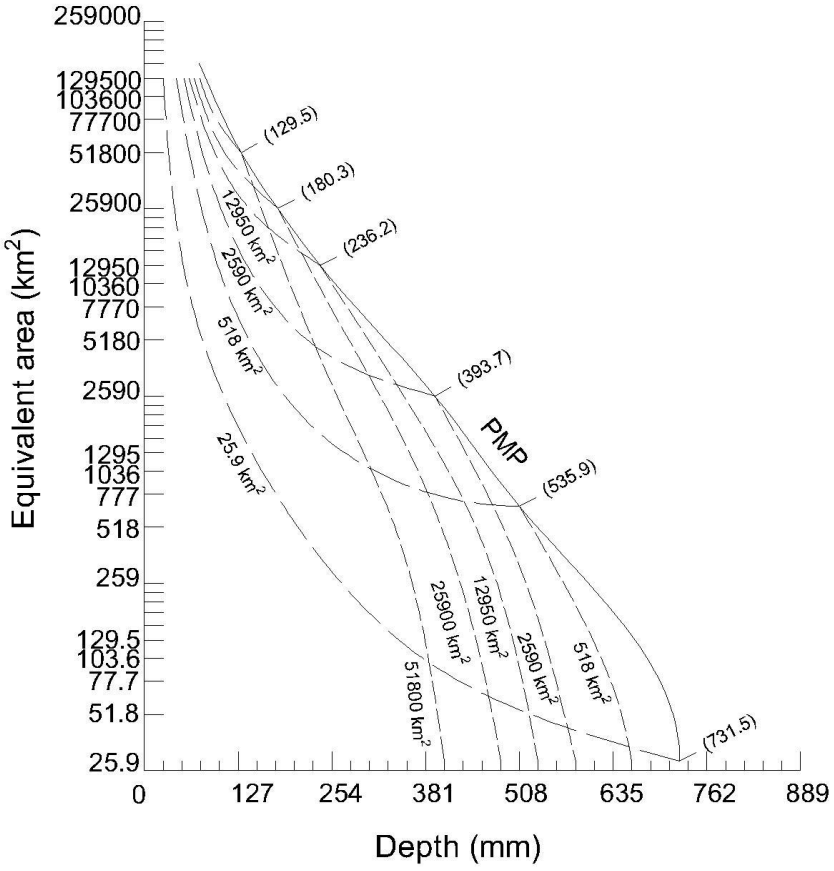

Figure 14 Within/without-storm curves for 6-hr PMP at 37°N, 89°W for standard area sizes. (Recreated from HMR 52 figure 14, Hansen et al., 1982)

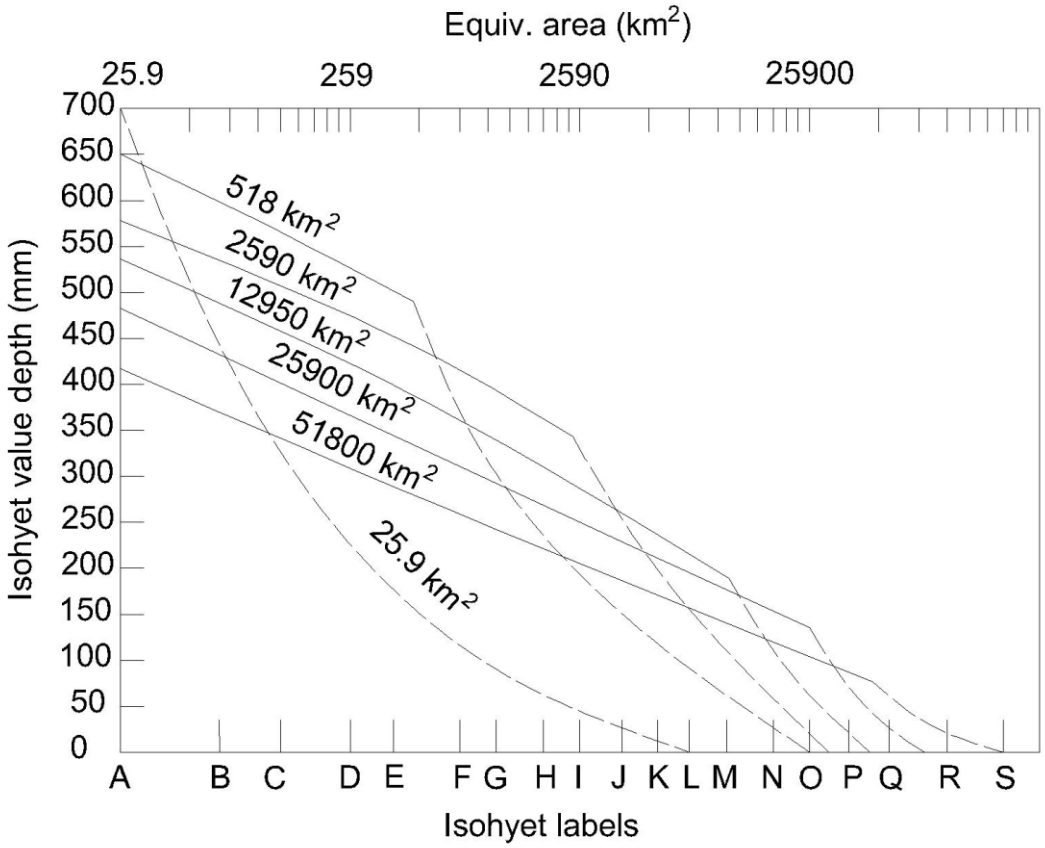

Figure 15 Isohyetal profiles for standard area sizes at 37ºN, 89ºW (Recreated from HMR 52 figure 15, Hansen et al., 1982)

Area of Pattern Applied to Drainage

For all the procedures stated above, the 2590 km^2 PMP was used as an example. In real application, we need to decide the area of PMP pattern to be applied to the drainage. In HMR 52, it chose to base the selection of PMP pattern on maximizing the volume of precipitation within the drainage. The maximum volume is a function of pattern centering, basin irregularity of shape, and the area size of PMP distributed over the drainage. HMR 52 recommended the centering of the pattern to place as many complete isohyets within the drainage as possible. The shape of the drainage is fixed and

only the area of the PMP pattern is variable. It provided a procedure involving a series of trials. To conduct the trial, one starts by selecting an area size in the vicinity of that for the drainage. It is convenient to choose areas that match those for the isohyets in the idealized pattern (e.g., 1813, 3885, 16835 km^2). Compute the volume of precipitation for each of the 3 greatest 6-hour increments of PMP for the area size chosen and obtain the total volume. Then, choose additional areas on either side of the initial choice, and evaluate the volume corresponding to each of these. By plotting the results as area size vs. volume, a size which produces the maximum volume can be approximated. This size is used as the area size of PMP pattern. For this study, in general, it makes sense that the PMP size which is close to the drainage area will result in the biggest volume. Thus, based on the study area (24162 km^2), we chose the standard shape area (25900 km^2) as the PMP size.

3.1.3 Temporal and Spatial Distribution of All Durations

HMR 52 used 6-hour PMP increment as the smallest unit for the 72-hour event. To improve accuracy, we used 1-hour time steps to construct the rainfall sequence. To achieve this, we collected data from 59 big storms and constructed depth-duration and depth-area maps. Then, the 1-hour point PMP from Chapter II was applied to the DAD curves to find the 25900 km^2 PMP of all durations. These PMP values were then applied to the WWSDA map to get isohyetal values of PMP of each duration. Note that the former duration PMP needs to be deducted from the latter to get the increment amount within this 1-hr time step. For example, the 1-hour PMP itself is one increment. The 2-

hour PMP values need to subtract the 1-hour PMP to get the second largest 1-hr increment, and the same applies to the rest of the durations. Once all the increments were calculated, we arranged them according to the rules in section 3.1.1. After all the procedures, the temporally and spatially defined PMP is derived as PMS.

3.1.4 Uncertainty of Probable Maximum Storm

The procedure stated above involves different kinds of uncertainties, such as uncertainties from the flexibility of arranging the precipitation time sequence, choice of storm shape, storm orientation, time interval, and isohyetal values referring to historical records (as shown in Figure 1). Unlike the statistical method, the uncertainty of this deterministic method can only be qualified with numerical sampling, e.g., with Monte Carlo simulation process. However, as the middle procedure to derive PMF and uncertainty, Monte Carlo process will lead to a dramatic growth of numerical samples. For example, if 200 mixed sets of parameters (storm orientation, time interval, etc.) were assigned to derive PMS and 200 R-R model parameter sets were assigned to derive PMF, a total of 40000 times of running need to be conducted by the R-R model, which is a huge burden. At the same time, even though there were complete reviews on the uncertainty of design rainfall (Al Mamoon and Rahman, 2014), storm design of PMP has not been studied yet. The deterministic procedure provided by HMR 52 managed to obtain the most severe conditions (e.g., orientation, shape, arrangement and so on) to derive PMF. Thus, we assume that those conditions have been met in this study and no uncertainty was considered in the PMS procedure.

3.2 Data

3.2.1 Probable Maximum Storm Study Area

The PMS study area is shown in Figure 16. It was based on the PMP study area of Chapter II as well as the event boundary of hurricane Harvey. The reason for the necessity of involving hurricane Harvey is that it was the most severe storm that happened in the area and is important to calibrate the R-R model. Thus, the study area was after comprehensive consideration. First, we referred to the water footprint of hurricane Harvey (https://owi.usgs.gov/vizlab/hurricane-harvey/) to estimate the event boundary inside the Brazos River basin. Second, the digital elevation model (DEM) data and the hydrologic unit code (HUC) map inside that boundary were downloaded from the USGS NED database and USDA NRCS database, respectively. Third, DEM data and HUC data were intersected to produce the final boundary of the study area. The total area was 24162 km^2. HEC-GeoHMS was used to generate the sub-basins and reaches. Sub-basins and reaches were generated by the program and manually corrected, referring to HUC maps. At last, a total of 36 sub-basins and 25 major reaches were obtained to represent the watershed. These subbasins and reaches will be used in the construction of the R-R model later in Chapter IV.

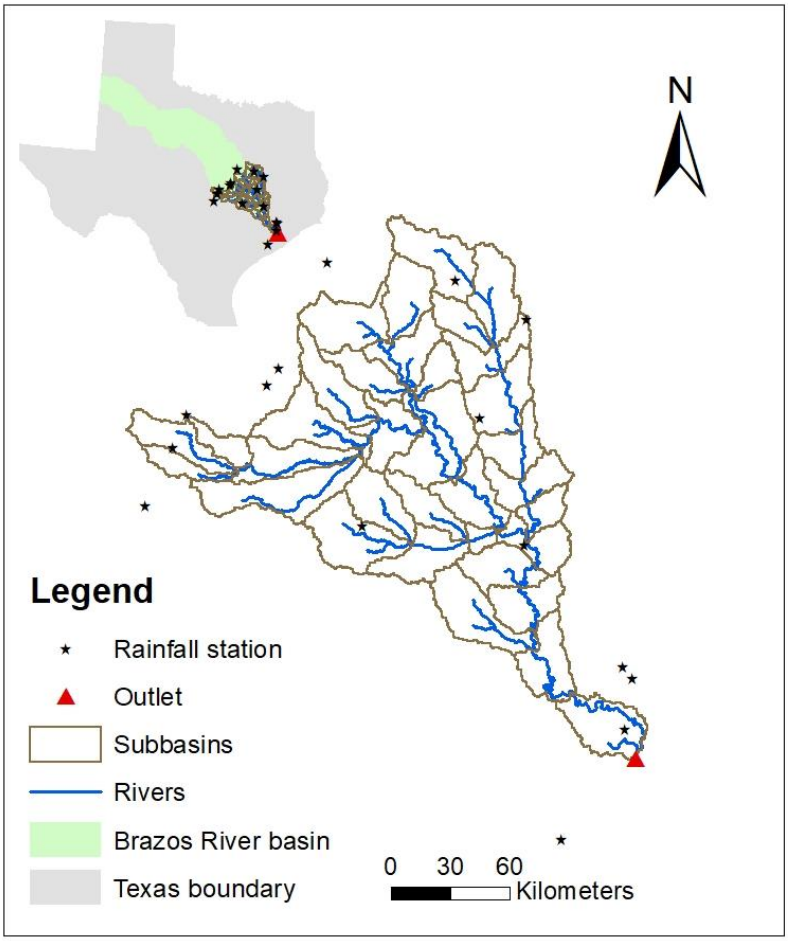

Figure 16 Lower Brazos River basin

3.2.2 Update of Historical Storm Records

In HMR 52, historical storm records were used to construct the temporal and spatial distribution of PMS. For example, the depth-area-duration (DAD) curves were constructed from these records and then applied to PMP values to derive a PMS. However, those storm records haven't been updated since the report was prepared. Thus, we collected the storms (59 in total) within and around Texas that occurred in recent

decades (1899-2015) from Texas Commission on Environmental Quality (TCEQ) PMP report (https://www.tceq.texas.gov/compliance/investigation/damsafetyprog.html). New DADs were constructed from the updated records to design PMS.

3.3 Results and Discussion

3.3.1 Depth-area-duration Curves of Updated Storm Records

The relationships between precipitation depth and duration and storm area size are essential to design a rainfall storm. We assumed that the 59 big storms were sufficient to capture the temporal and spatial distribution features of the PMS within or around Texas. Thus, the DAD curves derived from these storms were used to extend the 1-hr point PMP value to 72-hour duration PMP values with various storm area sizes. The 59 storm records collected from TCEQ contained DAD tables for each of the storm record. Figure 17 shows the plot of the percent of point depth against the storm area size for all the storms. The records with storm area larger than 50000 km^2 showed fluctuate curves which means that those data were less reliable. When storm area was larger than 5000 km^2, the precipitation depth dropped under 50% of the point depth. As the storm duration increased, the drop in depth became smaller. Figure 18 shows the relationship between duration and precipitation depth. Again, these data were retrieved from historical big storms which were assumed to represent the features of PMS. The PMP values increased with the duration increase. For a specific duration, the larger storm area PMP has a bigger value. The DAD relations shown in figure 17 and figure 18 were used to interpolate the PMP values for all durations and storm areas.

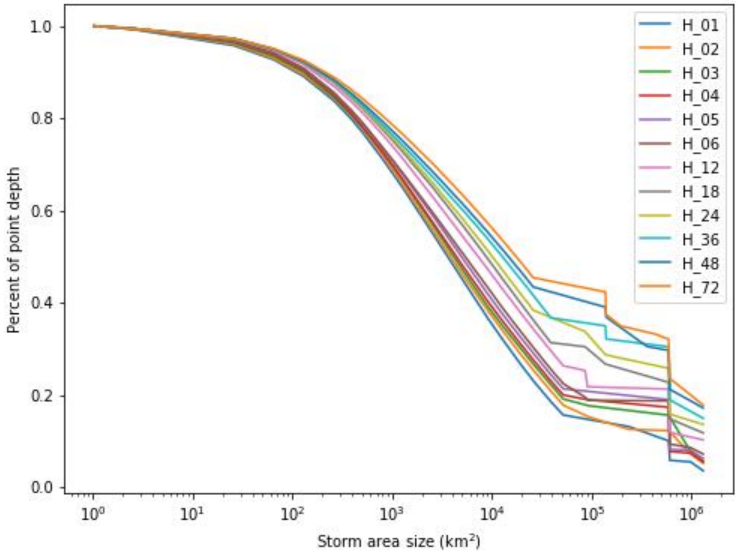

Figure 17 Depth-area relationship from updated storm records

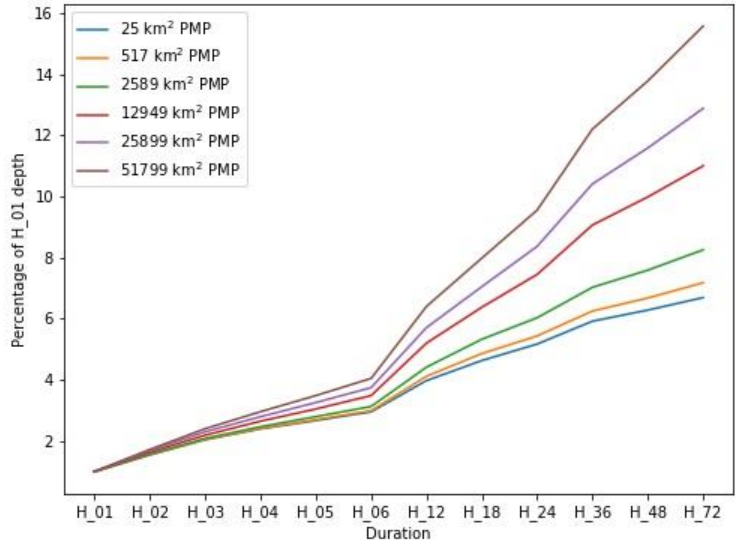

Figure 18 Depth-duration relationship from updated storm records

3.3.2 Within-without Storm Depth-Area Relations

HMR 52 introduced the concept of within-without storm depth-area (WWSDA) relation. The WWSDA relation represents the areal variation of precipitation within a storm that gives PMP for a particular area size. It can also be stated as the storm that results in PMP for one area size may not give PMP for any other area size. Except for the area size that gives PMP, the within-storm depth-area relation will give depths less than PMP for smaller area sizes. This concept was illustrated in the schematic diagram shown in Figure 19. However, after the update of historical storm records, an outside storm relation (red dashed line in Figure 19) different from that described in HMR 52 was found.

First, Figures 20 (a-d) were constructed similar to Figure 13 as the preprocessing for the WWSDA relation. Figure 20 only shows (a) 1-hr, (b) 6-hr, (c) 24-hr and (d) 72-hr duration relations, the remaining duration figures are shown in Appendix A. It shows the ratio of the depth of varying storm area (numerator) to the depth of a particular storm area (denominator) for a particular duration. Not all durations are shown here, but with the duration increased (from a to d), all the ratios for different storm areas decreased. Within each duration, the ratio increased as the particular storm area (denominator) increased. Figure 20 shows similar trends with figure 13 from HMR 52. Second, the average PMP values retrieved from Brazos River basin (from Chapter II) was applied to Figure 20 for each duration to obtain within/without-storm average PMP curves for each duration. Figure 21 shows the example of 6-hr duration case.

Compared to figure 14, the within storm curves showed that except for the area size that gave PMP, they gave depth larger than PMP for smaller area sizes, which is opposed to the relation stated by HMR 52. The red dashed line in figure 19 was a simple implementation of the new discovered relation. We believed that the new opposite relation reflected by the updated storms and PMP values also make sense. For example, consider that two different sized storms ($A_1>A_2$) happened at a particular location with the same duration which both resulted in PMP with areal average depths ($PMP_1<PMP_2$). Most studies showed that average rainfall intensity decreased as storm radius increased (Yu et al, 2017), which is why $P_1<P_2$, hence, $PMP_1<PMP_2$. However, there was no evidence that the average rainfall intensity of storm 1 within the area of A_2 must be smaller than P_2. Accordingly, rainfall from PMP_1 within A_2 is not necessarily smaller than PMP_2. Thus, the assumption in HMR 52 "Except for the area size that gives PMP, the within-storm depth-area relation will give depths less than PMP for smaller area sizes." was not necessarily true and there was no evidence prove it. Instead, our updated records showed the opposite results in figure 21.

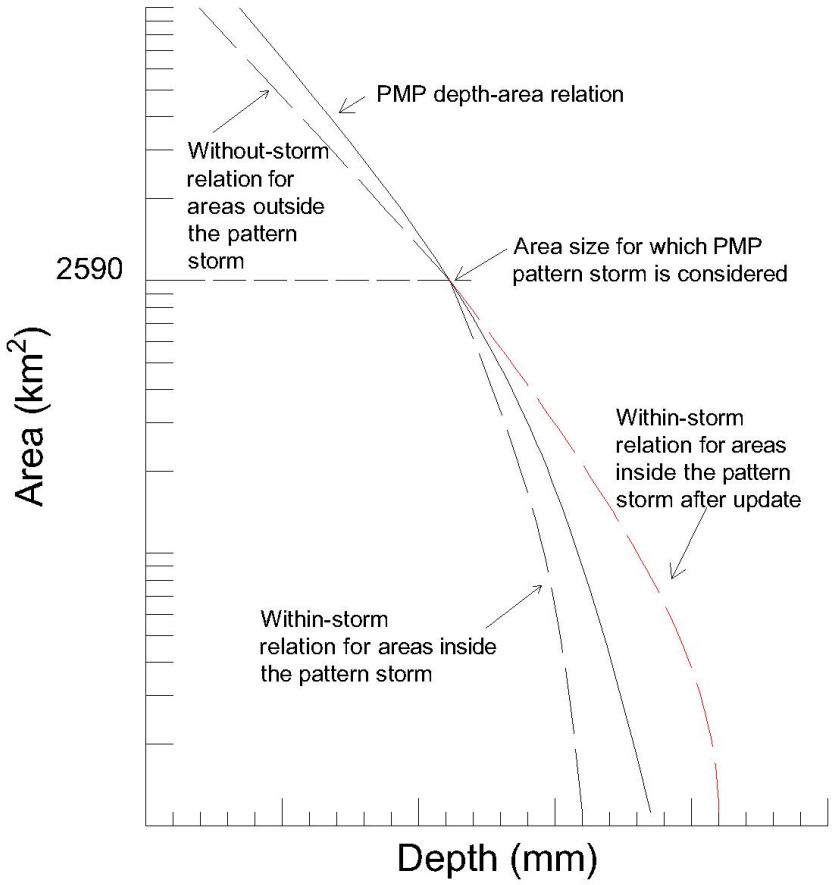

Figure 19 Schematic diagram showing the relation between depth-area curve for PMP and the within/without-storm relations for PMP at 2590 km^2 (partial recreated from HMR 52 figure 1, Hansen et al., 1982)

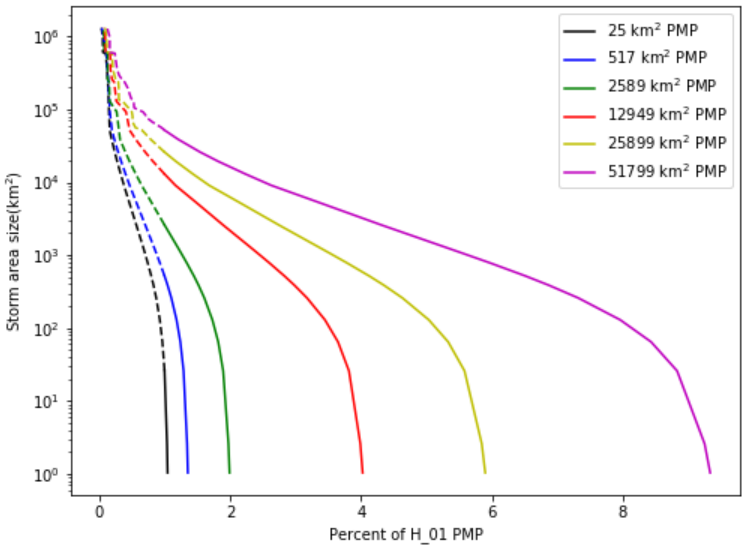
25 km² PMP
517 km² PMP
2589 km² PMP
12949 km² PMP
25899 km² PMP
51799 km² PMP
Storm area size(km²)
Percent of H_01 PMP

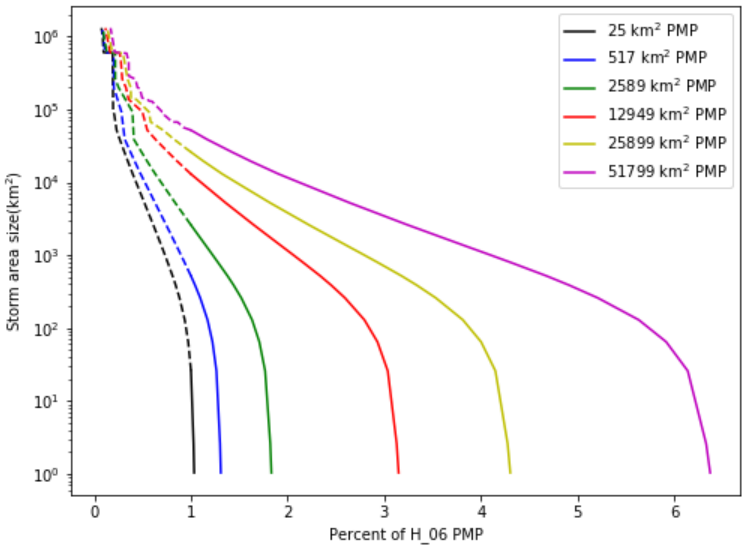
25 km² PMP
517 km² PMP
2589 km² PMP
12949 km² PMP
25899 km² PMP
51799 km² PMP
Storm area size(km²)
Percent of H_06 PMP

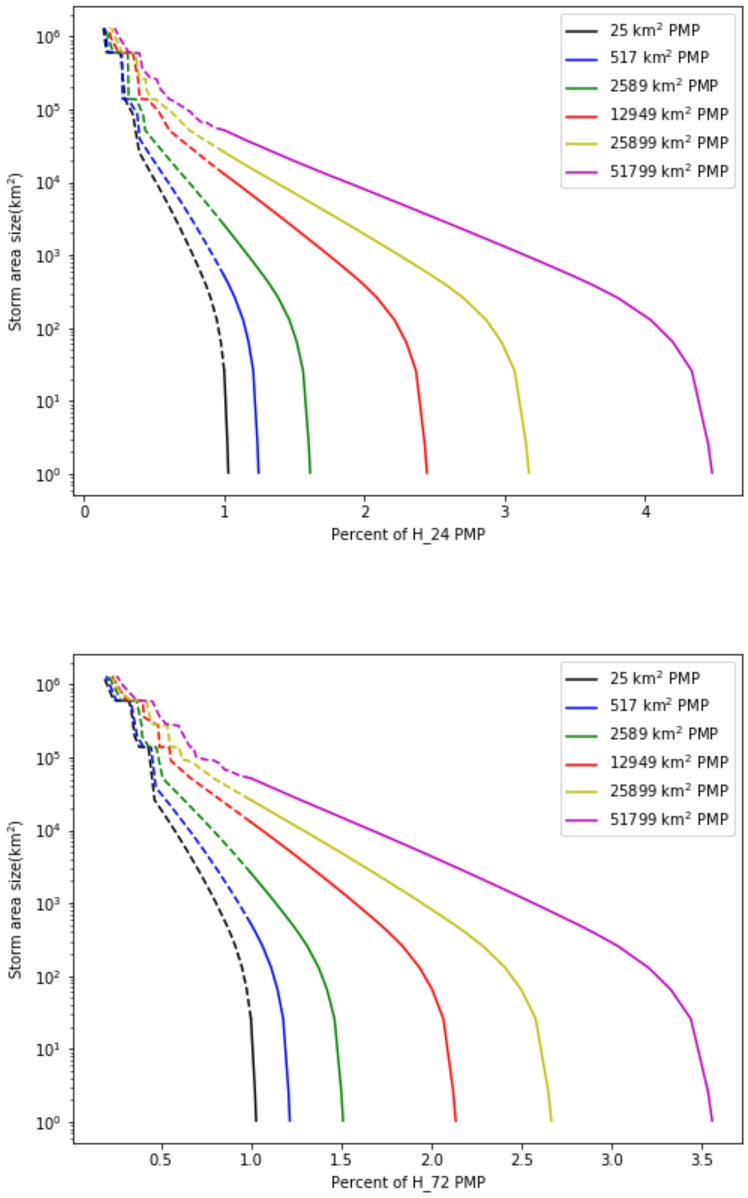

Figure 20 Within/without-storm average curves for standard area sizes of (a) 1-hr, (b) 6-hr, (c) 24-hr and (d) 72-hr duration.

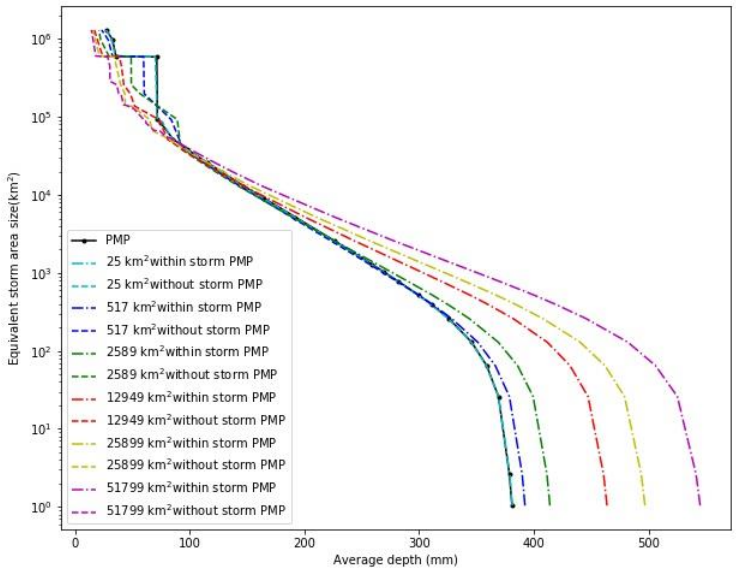

Figure 21 Within/without-storm curves for 6-hr average PMP in the study area for standard area sizes.

3.3.3 Probable Maximum Storm with Spatial and Temporal Distribution

With procedure in section 3.1.2, the reverse process generally followed for deriving DAD curves from an isohyetal profile, and the average areal PMP values in figure 21 were transferred to the standard isohyetal values in figure 22. Note that PMPs of all durations were transferred by this procedure, which means there were 72 maps. To read this map, e.g., in our case, refer to the 25899 km^2 PMP line and read the contour values for standard areas (listed in figure 12). After obtaining the contour value of each standard area, ArcGIS was used to display the spatial distribution as shown in figure 23. The distribution in figure 23 was the total depth of a duration. In order to generate the rainfall time sequence to be used in the R-R model, the rainfall depth in each time step

(1-hr increment hyetograph) within the study area needed to be specified. It was achieved by subtracting each duration's PMP map by the later one and then arranging the 72 hours magnitudes in a preferred way, such as described in figure 11. In this study, we put the most intensive hour rainfall in the middle and then progressively decreased the amounts on both sides. For each ellipse size, a hyetograph was generated as stated above. Figure 24 showed the hyetographs for all ellipse area sizes. Each spatial distribution map with the hyetograph was introduced to the R-R model and then run for the PMF hydrograph.

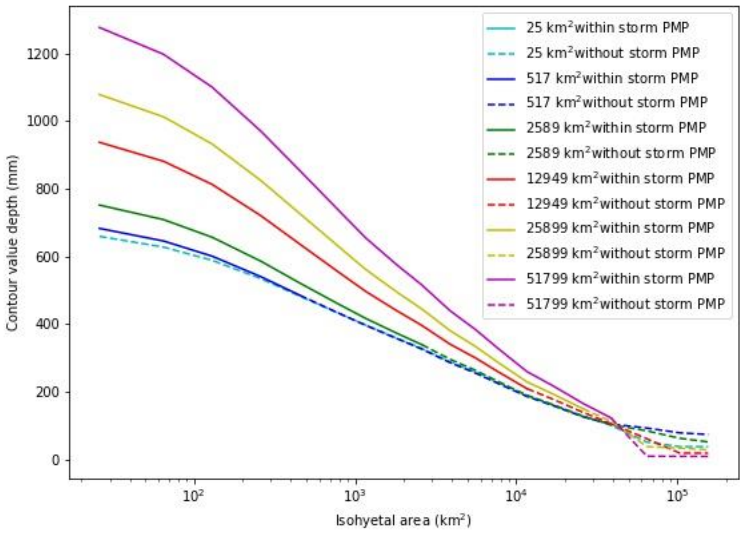

Figure 22 6-hr PMP isohyetal profiles for standard area size storms in the study area.

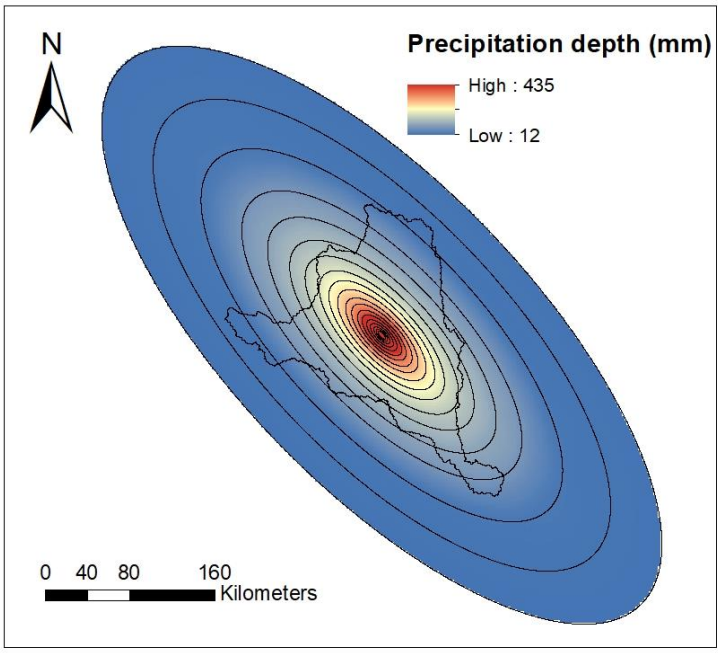

Figure 23 6-hr 25899km^2 average PMP spatial distribution in the study area.

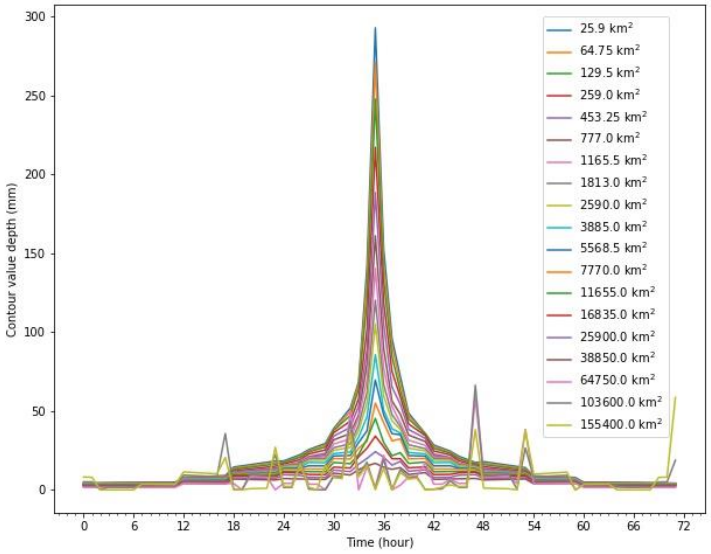

Figure 24 Hyetographs of different standard ellipse areas for a 25900 km^2 PMP

CHAPTER IV

UNCERTAINTY ANALYSIS OF RAINFALL-RUNOFF MODELS OF EXTREME EVENTS WITH GLUE METHOD

4.1 Methods and Materials

Many rainfall-runoff (R-R) models have been developed, but this study does not attempt to investigate the differences or determine the best model. For this particular "extreme event-based large scale" hydrologic model, the HEC-HMS model was selected as the modeling platform. Hurricane Harvey was chosen to be the calibration event and hurricane Patricia was used for validation. NEXRAD precipitation and flow records during the event, basin hydrogeologic characteristics in Texas, and other related information were collected. The generalized uncertainty likelihood estimation (GULE) method was implemented as the framework for evaluating the extreme flood event uncertainty during the modeling procedure.

4.1.1 Model Structure

In this study, the Hydrologic Modeling System from Hydrologic Engineering Center of the U.S. Army Corps of Engineers (HEC-HMS) was used to build the R-R model structure. HEC-HMS has been widely used in North America and all around the world. It is a semi-distributed conceptual model which provides users multiple options to build their own model structures (HEC-HMS Users Manual, version 4.2, 2016). Based on the HEC-HMS applications manual, Initial and Constant loss (IC), and Soil Conservation Service (SCS) Curve Number (CN) method for computing abstractions,

ModClark unit hydrograph for transforming rainfall-excess into surface runoff, baseflow recession, and Muskingum-Cunge method for flow routing were selected to build the model structure. The model is extreme-event based and no surface loss method is used in the model, since the event period is relatively short and humidity in the air is high and no evapotranspiration is assumed to occur in the process. The canopy method was ignored because of the relatively large study area. Besides, calibration of the model through the loss method will compensate for these two ignored processes. The main formulations of HEC-HMS components are summarized below (HEC-HMS technical reference manual).

The rainfall excess P_{et} during a time interval with relation to constant loss rate f_c and initial loss I_L is given by:

$$P_{et} = \begin{cases} 0 & if \sum p_i < I_L \\ p_t - f_c & if \sum P_i > I_L \; and \; p_t > f_c \\ 0 & if \sum P_i > I_L \; and \; p_t < f_c \end{cases} \tag{32}$$

The SCS-CN model describes the relationship between precipitation excess and soil cover, land use, and antecedent moisture as:

$$P_e = \frac{(P - I_a)^2}{P - I_a + S} \tag{33}$$

where P_e is the accumulated precipitation excess at time *t*; P is the accumulated precipitation depth at time *t*; I_a is the initial abstraction which is assumed to equal to 0.2 S; S is the potential maximum retention and is calculated by CN using the following equation (IS system):

$$S = \frac{25400 - 254CN}{CN} \tag{34}$$

The Clark unit hydrograph model transforms the precipitation excess to outflow using the continuity equation and a linear reservoir model. The ModClark method applied the unit hydrograph to a cell-based basin:

$$\frac{dSW}{dt} = I_t - O_t \tag{35}$$

$$SW_t = RO_t \tag{36}$$

$$O_t = C_A I_t + C_B O_{t-1} \tag{37}$$

$$C_A = \frac{\Delta t}{R + 0.5\Delta t} \tag{38}$$

$$C_B = 1 - C_A \tag{39}$$

$$\overline{O_t} = \frac{O_{t-1} + O_t}{2} \tag{40}$$

where SW is the storage of water throughout the watershed; I_t is the average inflow to storage at time *t*; O_t is the outflow from storage at time *t*; *R* is a constant linear reservoir parameter; C_A and C_B are the routing coefficients; and Δt is the computation time step.

A specific time-area relationship is built into the HEC-HMS program to simulate the watershed area contributing to flow at the outlet as a function of time:

$$\frac{A_t}{A} = \begin{Bmatrix} 1.414\left(\frac{t}{t_c}\right)^{1.5} for\ t \le \frac{t_c}{2} \\ 1 - 1.414\left(1 - \frac{t}{t_c}\right)^{1.5} for\ t \ge \frac{t_c}{2} \end{Bmatrix} \tag{41}$$

where A_t is the cumulative area contributing to the watershed at time *t*; *A* is the total watershed area; and t_c is the time of concentration.

The exponential recession model defines the relationship between baseflow at time *t* and an initial value as:

$$Q_t = Q_0 K^t \tag{42}$$

where Q_t is the baseflow at any time *t*; Q_0 is the initial flow; and *K* is an exponential decay constant.

The Muskingum-Cunge method was selected for flow routing. It combines a continuity equation and a momentum equation, and uses a linear approximation to yield the convective diffusion equation:

$$\frac{\partial A}{\partial t} + \frac{\partial Q}{\partial x} = q_L \tag{43}$$

$$S_f = S_o - \frac{\partial y}{\partial x} \tag{44}$$

$$\frac{\partial Q}{\partial t} + c\frac{\partial Q}{\partial x} = \mu\frac{\partial^2 Q}{\partial x^2} + cq_L \tag{45}$$

where *A* is the wetted perimeter; *t* is time; *Q* is the flow in channel; *x* is the distance along the flow path; q_L is the lateral inflow; S_f is the energy gradient; S_o is the bottom slope; *y* is the hydraulic depth; *c* is the wave celerity; and μ is the hydraulic diffusivity. For the above model structure, model parameters are summarized in table 4. For a detailed estimation of the initial parameter values, please refer to Appendix B, which described specifically how the parameters were estimated using lower Brazos River Basin as an example. Parameters of other basins were derived in the same way.

Table 4 Model parameters

Method	Parameter symbol	Parameter definition	Calibration
IC loss method	A_s	Subdivision drainage area	No
	I_L	Initial loss	Yes
	f_c	constant loss rate	Yes
SCS CN loss method	CN	Curve number	Yes
	IP	Impervious percentage	No
	I_a	Initial abstraction	Yes
ModClark unit hydrograph method	R	Constant linear reservoir parameter	No
	t_c	Time of concentration	Yes
Recession baseflow method	Q_0	Initial baseflow	Yes
	K	Exponential decay constant	Yes
Muskingum-Cunge routing method	L	Reach length	No
	N	Roughness coefficient	Yes
	S_e	Energy grade	No
	W	Bottom width of reach	No
	S_s	Side slope	No

4.1.2 Generalized Likelihood Uncertainty Estimation Methodology

In the GLUE method, a generalized likelihood measure is chosen to characterize the performance of a model (observed data vs. simulated data). In this study, we used a likelihood measure based on the NSE criterion with shape factor N (we chose N equal to 1):

$$L[M(\theta_i|Y_T, Z_T)] = \left(1 - \frac{\sigma_\epsilon^2}{\sigma_0^2}\right)^N \; for \; \sigma_\epsilon^2 < \sigma_0^2 \tag{46}$$

where L indicates the likelihood measure of the model; Y_T is the input data; Z_T is the observed data; θ_i is the ith parameter set value; $M(\theta_i|Y_T, Z_T)$ indicates the ith model conditioned on input data Y_T and observed data Z_T; σ_ϵ^2 is the error variance; σ_0^2 is the variance of the observations; and N is the shape factor.

Then, feasible ranges of parameter sets (e.g. 200 sets were generated in this study) were generated by Monte Carlo simulation. We used the uniform distribution as the prior information of the parameters and the range was determined, based on the calibrated parameter values. The likelihood measures resulting from each parameter set were filtered by the chosen efficiency criterion (we filtered the half top ensembles as accepted models). An update of the prior parameters (originally used feasible parameter values) can be done, based on the Bayesian framework:

$$L[M(\theta)] = L_0[M(\theta)]L_T[M(\theta|Y_T, Z_T)]/C \tag{47}$$

where $L_0[M(\theta)]$ is the specified prior likelihood for the model $M(\theta)$ with parameter vector θ; $L_T[M(\theta|Y_T, Z_T)]$ is the likelihood measure calculated for the model over period T with input vector Y_T and observed variable vector Z_T; and C is a scaling constant.

Given the samples from Monte Carlo simulation, for each time step t, the sample likelihood values can be renormalized such that $\sum_{i=1}^{B} L[M(\theta_i)] = 1$, where $M(\theta_i)$ now indicates the ith behavioral Monte Carlo sample, so that

$$P\left(\widehat{Z_t} < z\right) = \sum_{i=1}^{B} L\left[M(\theta_i)\middle|\widehat{Z_{t,i}} < z\right] \tag{48}$$

where $\widehat{Z_{t,i}}$ is the value simulated by model $M(\theta_i)$ at time *t*, and *B* is the number of total samples. Thus, the conditioned hydrograph quantiles can be obtained from equation (48).

In order to quantify the level of uncertainty, we used the relative width (R-factor) to measure the relative band width of uncertainty range and Shannon entropy to describe the distribution of NSE. The R-factor is defined as below (Abbaspour, 2008), which represented the average thickness of the 95% prediction uncertainty (95PPU) band divided by the standard deviation of the observed data:

$$R-factor = \frac{\frac{1}{n}\sum_{t}^{n}\left(q_{t,95\%}^{M} - q_{t,5\%}^{M}\right)}{\sigma_{obs}} \tag{49}$$

where n is the number of time steps; $q_{t,95\%}^{M}$ and $q_{t,5\%}^{M}$ are the discharge values corresponding to 95 percent and 5 percent likelihood quantiles; and σ_{obs} is the standard deviation of observed discharge series.

The Shannon entropy measure H is defined as (Beven and Binley, 1992):

$$H = \sum_{i=1}^{B} L_i \cdot \log_2 L_i \tag{50}$$

where the likelihoods L_i, *i*= 1, 2, . . . B, are scaled such that $\sum_{i=1}^{B} L_i$ = 1 and B is the total number of realizations. This is maximum (= $\log_2 B$) when all realizations are equally likely (the case of the uniform prior distribution). It has a minimum of 0 when one single realization has a likelihood of 1 and all others have a likelihood of zero (the case of the 'optimal' parameter set).

4.1.3 Analysis of Uncertainty Sources

The GLUE method quantifies the uncertainty by resampling model parameters and filtering acceptable ensembles with a model efficiency value. However, simply resampling model parameters resulted in a limitation on investigating the underlying sources of uncertainty. For example, before model parameters were sampled, the model needed to be calibrated first. The calibration procedure determined the values of parameters. In other words, uncertainties were embedded in data collection for calibration (e.g., precipitation data, flow data, soil data, and land use data). Figure 25 demonstrated the process of uncertainty accumulation. As shown in the schematic diagram, we traced back model parameter uncertainties and separated the sources into two main parts: model input and model setup.

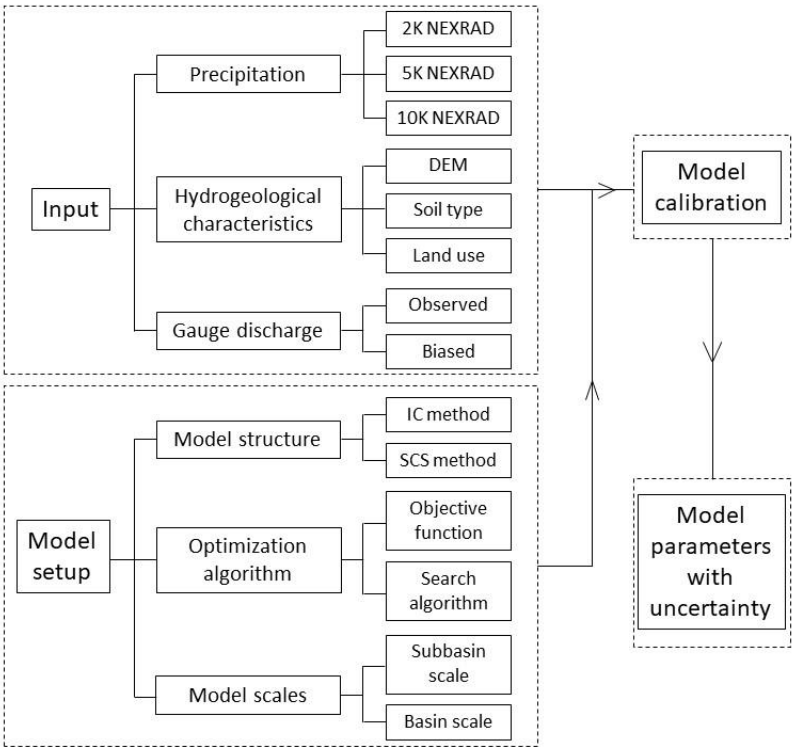

Figure 25 Schematic diagram of R-R model uncertainty accumulation process

Uncertainty from Input Data

Model input contributed to the uncertainty by involving three major data types: precipitation, hydrogeological characteristics, and gauge discharge. It is the most common way to introduce error when preparing precipitation data for the model. For example, there are precipitation data from different sources, such as ground-based stations and radar sensors. The Thiessen polygon method is usually used when only data from ground stations are available. In that case, the density of stations would be the major uncertainty source, since higher density of stations would usually produce more accurate data. The Next Generation Weather Radar (NEXRAD) system currently comprises 160 sites throughout the United States and select overseas locations. It is

generally believed that NEXRAD precipitation data provides more accurate spatial results than data interpolated from ground stations. However, different studies showed that NEXRAD precipitation data did not necessarily lead to better model performance (Gali et al., 2012). In this paper, we used '4KM Gridded Data (GRIB) Stage IV Data' for hurricanes Harvey and Patricia and scaled them (with ArcGIS raster mosaic functions) into three different size grid cell maps: 2 kilometers (2K), 5 kilometers (5K), and 10 kilometers (10K). The purpose was to detect how precipitation data from different resolution levels impacted model performance and uncertainty, e.g., does coarser precipitation data necessarily result in poorer model performance and more uncertainty?

To develop a model in any platform requires hydrological data, such as DEM, soil type, and land use data. Except for measurement error, the main source of uncertainty is grid size of the data (assume all these data are grid-based raster data). Now-a-days, most of these data have very small grid size which can be considered as high accuracy data (e.g., 30-meter resolution for land use cover data). In this case, resampling those data into model grids of 2 kilometers will lead to minor influence on model uncertainty. Thus, we did not analyze uncertainty caused by those data. However, theoretically, they caused uncertainty in the model as well.

Finally, discharge data from gauge stations also causes uncertainty to the model. The main error may stem from measurement instruments, time steps of measurement, and compilation of data. We introduced a 10% range biased synthetic discharge data during hurricane Harvey to represent the uncertainty. We used 'Observed' and 'Biased'

in the model title to represent the true observed discharge and 10% error introduced synthetic discharge, respectively.

Uncertainty from Model Setup

Setting up a model involves choosing model structure, optimization algorithm, and basin and sub-basin scales. Choosing a model platform itself also causes uncertainty, since different models have their own structures, assumptions and advantages. In this study, we assumed that the difference of model structures represented the majority of model difference. Thus, this type of uncertainty was included in the process of choosing a model structure. Model structure comprises certain modeling methods, such as surface method, loss method, transform method, baseflow method, and routing method. In order to determine the uncertainty introduced by those methods, we constructed the model with two different loss methods as examples: the IC method and the SCS method. To reduce complexity, methods for other modules were kept the same. The other methods adopted were: ModClark (transform method), recession baseflow (baseflow method), and Muskingum-Cunge (routing method).

Optimization algorithm is fundamental for model calibration, different objective functions, and search algorithm which may lead to significantly different parameter values (Dariane et al., 2016). There are numerous factors affecting an algorithm considered as the optimization one (Arsenault et al., 2014) and hence different algorithms at various locations were compared. Usually, more than one accepted algorithm can be used for constructing a particular model, which also corresponds to the basis of ‘equifinality’ in the GULE methodology. In this study, we did not discuss the

uncertainty caused by the optimization algorithm. Instead, the most basic and accepted algorithm embedded in the HEC-HMS package was used: univariate gradient and peak-weighted root mean square error.

The two types of scales related to hydrologic modeling are total basin area and sub-basin (or model unit) area. A complete model simulates a whole basin area which comprises sub-basins. Numerous studies have explored the relationship between scales and model performance (e.g., Booij, 2005; Yu et al., 2012; Zhang et al., 2013; Ichiba et al., 2018; Perrin et al., 2001; Merz et al., 2009). However, this kind of uncertainty has not been formally quantified into the GLUE framework. We introduced 26 different-sized basins, and different levels of hydrologic unit code (HUC8, HUC10, HUC12) as subbasin areas to explore how model scales affected model performance and uncertainty.

The above two sections established the basic framework for tracing uncertainty sources in constructing a model. The corresponding models with various structures and accuracies of precipitation and discharge were built: 2K-IC-Observed (pivot model), 5K-IC-Observed, 10K-IC-Observed; 2K-SCS-Observed, and 2K-IC-Biased models, respectively. Each of them represented different sources of uncertainty.

Uncertainty Affected by Extreme Event Oriented Components

The controlling features that make an extreme event stand out are the intensity of precipitation, critical peak flow, and large scope of the storm (basin scale). Thus, extreme event model uncertainties related to these features may act differently from normal flood events, which correspond to relatively small precipitation, peak flow, and range of influence. To investigate the possible patterns of the difference, we compared

model efficiency and uncertainty within 26 basins with different precipitation intensities, gauge discharges, and model scales. 26 samples were considered sufficient in the lower basin areas in Texas.

4.2 Data

4.2.1 Rainfall-runoff Model Study Area

Basins in southeast Texas, USA (Figure 26), were chosen as the R-R model study area. The area was delineated according to the water footprint of hurricane Harvey, since it is the main event to be collected for calibration. The adjacency of basins to the Gulf of Mexico leads to high frequency of storms, and they have relatively sufficient data available (such as USGS gauges). Fourteen official basins (a total area of 113188.58 km^2) were included in this area during hurricane Harvey. A total of 26 independent R-R models were built based on sub-basins after the delineation of independent watersheds. Climate and weather features in the study area are summarized in the link below: https://statesummaries.ncics.org/chapter/tx/.

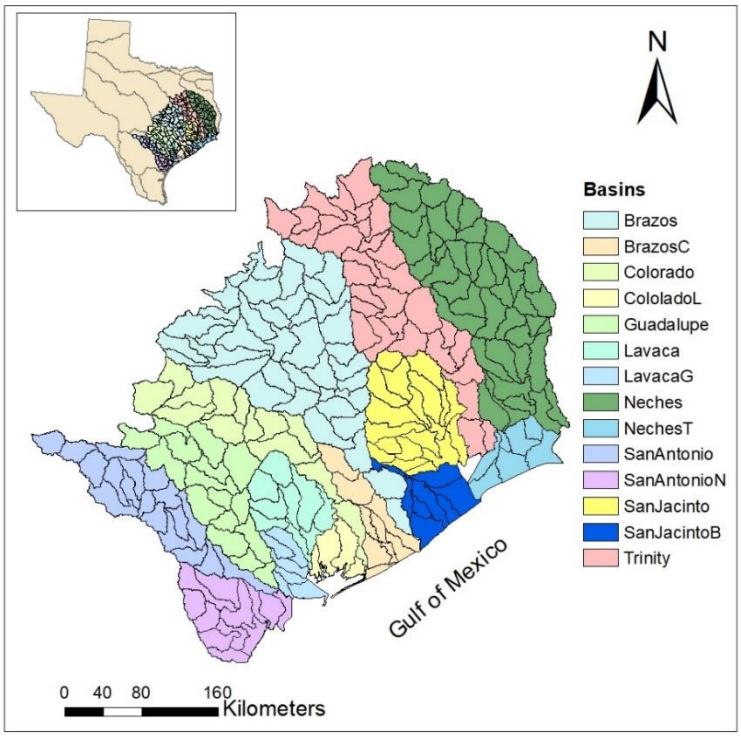

Figure 26 Basins in Texas near Gulf of Mexico

4.2.2 Software Used and Data Sources

We used HEC-HMS (version 4.2.2) as the basic hydrologic model software to construct the models. HEC-DSSVue was used to store discharge data and NEXRAD grid data to support HEC-HMS. HEC-GeoHMS (version 10.0) was used to delineate the DEM data and parameterize hydrogeological data. ArcGIS desktop (version 10.6) was used to pre-process the spatial related data. Python (version 3.4) was used for coding to deal with the intensive data compiling and calculus.

We referred to the water footprint of hurricane Harvey (https://owi.usgs.gov/vizlab/hurricane-harvey/, accessed on March 25, 2020) to estimate the event boundary in southeast area in Texas, near Gulf of Mexico. The digital

elevation model (DEM) data and the hydrologic unit code (HUC) map inside that boundary were downloaded from the USGS NED database (https://viewer.nationalmap.gov/basic/, accessed on November 25, 2019) and USDA NRCS database (https://websoilsurvey.sc.egov.usda.gov/App/WebSoilSurvey.aspx, accessed on November 25, 2019), respectively. Soil data were downloaded from USDA NRCS website (https://websoilsurvey.sc.egov.usda.gov/App/WebSoilSurvey.aspx, accessed on November 25, 2019). Land cover data (30 m resolution, 2016 version) were downloaded from MRLC website (https://www.mrlc.gov/, accessed on November 25, 2019). Hourly NEXRAD precipitation data (4 km grid size) were collected from NCAR/UCAR EOL data website (https://data.eol.ucar.edu/dataset/21.093, accessed on November 25, 2019). Hourly discharge flow data were collected from USGS website (https://waterdata.usgs.gov/nwis, accessed on March 25, 2020). Details of the two events of hurricane Harvey and Patricia can be found in National Hurricane Center Tropical Cyclone Reports (Kimberlain et al, 2016; Blake and Zelinsky, 2018). Appendix B also described how these data were utilized in the model parameter estimation.

4.3 Results and Discussion

4.3.1 Performance and Uncertainty of 2K-IC-Observed Model

Based on pre-study, the IC method was chosen as the loss model. With NEXRAD data of 2K and observed discharge flow data, the model named 2K-IC-Observed was calibrated as the pivot model. Except for one model collapsing during calibration, 25 models had satisfactory NSE after calibration (The NSE of 'Sanantonio'

basin was below 0 and was not included in the following analysis). Predictably, most of the model validations for hurricane Patricia failed (only 3 out of 25 models had validation NSE above 0.6). We will discuss the failure of validation at the end of results and discussion section. Table 5 shows the calibration results of each model. The GLUE method was applied to each of the models and then the two indices were calculated. Each model had a total of 200 realizations, top half of the realizations were filtered and used in calculation. The hydrographs (200 realizations) were compared to the observed flows, as shown in Figure 27.

Table 5 Performance and uncertainty level of 2K-IC-Observed Model

Basin name	Basin area (KM2)	Subbasin number	Average area of subbasin	Precipitation (MM)	Peak flow (m3/s)	NSE	Shannon entropy*	Relative width	Realizations covered*
Brazos	25858.37	36	718.29	275.4	3763.9	0.84	6.643	0.48	0
BrazosC	2264.69	19	119.19	547.8	1299.0	0.79	6.640	0.41	0
ColoradoL	371.1	27	13.74	381.4	215.6	0.91	6.644	0.30	0
Colorado	8991.06	11	817.37	403.2	2510.2	0.54	6.642	0.37	0
Guadalupe	9168	14	654.86	297.7	5037.4	0.84	6.644	0.24	0
Lavaca000	2123.41	13	163.34	340.5	2094.2	0.77	6.643	0.27	0
Lavaca390	1447.45	7	206.78	372.2	735.8	0.81	6.644	0.26	0
Lavaca450	771.26	5	154.25	318.3	580.2	0.81	6.643	0.39	0
Lavaca503	379.77	3	126.59	287.8	199.8	0.93	6.643	0.47	1
Lavaca504	132.55	1	132.55	298.5	51.8	0.76	6.643	0.49	0
LavacaGP1	219.99	3	73.33	260.4	189.0	0.98	6.644	0.41	1
LavacaGP2	166.7	5	33.34	237.5	257.0	0.93	6.643	0.42	1
Neches	25321.07	35	723.46	372.6	6537.3	0.80	6.644	0.23	0
SanantonioN	1788.16	15	119.21	185.2	129.6	0.95	6.642	0.67	1
SanjacintoP1	2466.15	13	189.7	534.3	3707.3	0.92	6.644	0.12	0
SanjacintoP2	1046.95	9	116.33	688.2	2215.9	0.97	6.644	0.27	1
SanjacintoP3	734.52	3	244.84	799.7	891.5	0.99	6.644	0.44	1
SanjacintoP4	855.56	3	285.19	622.7	3084.7	0.86	6.640	0.41	0
SanjacintoP5	268.15	1	268.15	551.3	594.3	0.81	6.643	0.06	0
SanjacintoP6	303.07	1	303.07	641.4	2164.9	0.54	6.613	0.34	0

Basin name	Basin area (KM2)	Subbasin number	Average area of subbasin	Precipitation (MM)	Peak flow (m3/s)	NSE	Shannon entropy*	Relative width	Realizations covered*
SanjacintoP7	492.16	3	164.05	861.3	928.2	0.97	6.644	0.35	1
SanjacintoP8	618.29	1	618.29	872.7	993.3	0.78	6.644	0.12	0
SanjacintoBP1	235.93	7	33.7	879.9	475.4	0.85	6.644	0.17	0
SanjacintoBP2	268.75	7	38.39	978.1	1245.2	0.89	6.643	0.37	0
Trinity	17770.84	27	658.18	187.9	3113.0	0.82	6.644	0.29	0

*Shannon entropy were calculated based on the top half realizations, where B=100, which means the maximum value is 6.644. '1' means that the observed flow was fully covered by the 200 realizations.

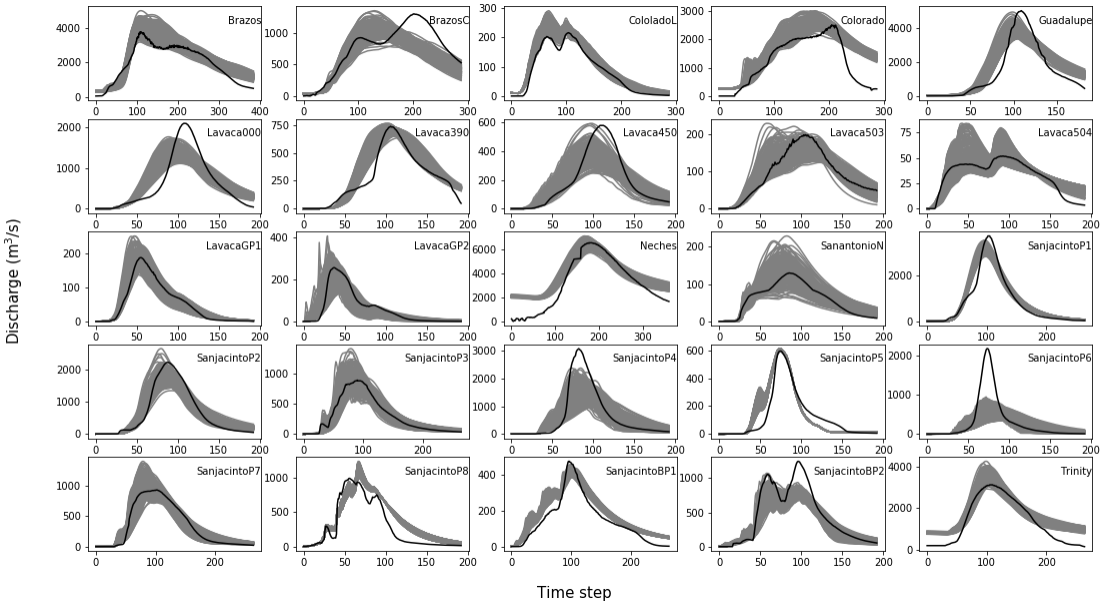

Figure 27 . Hydrograph ensembles (grey lines) versus observed flows (solid black lines) of 25 basins

In Figure 27, the grey lines are the 200 realizations and the solid black line is the observed flow. Confidence intervals of each basin can be constructed, based on those graphs with GLUE method too, which were not presented here. However, it would be just a regular GLUE study application as mentioned in the introduction section. What interested us more is the potential relationships between different models with uncertainty levels. Some of the basins produced ensembles which 'bracket' the observed

flow completely (Lavaca503, LavacaGP1, LavacaGP2, SanantonioN, SanjacintoP2, SanjacintoP3, and SanjacintoP7). All those basins had NSEs above 0.90. CololadoL and SanjacintoP1 had NSE above 0.90 and were nearly completely covered by the realizations. Ideally, a full coverage leads to a high relative band width. However, the converse is not necessarily true. Realizations derived from the GLUE method did not always cover the observed hydrograph, which has been shown by numerous studies (Mirzaei et al., 2015). Figure 28 shows the relationship which indicates that the relative band width had no correlation with NSE. For further implementation, we explored relations between calculated indices and basin features. In Figure 29, for smaller area basins, the average area of subbasins and peak flow tended to have their observed flows being fully covered. But those features did not lead to smaller relative uncertainty band widths. Among the four features, precipitation and peak flow showed relatively notable negative correlations with relative band width. It may be explained that with increasing intensity of precipitation and peak flow, the variation of hydrologic response also increased. From equation (49), higher standard deviation resulted in smaller relative band width. It seemed that NSE had a relatively notable negative correlation with the average area of subbasins (r=-0.48). However, it needs to be interpreted carefully. There was a gap of 300-600 km^2 in the figure. From 0 to 300 km^2, NSE decreased as the average area increased. Right after 600 km^2, NSE bounced back to higher values and then decreased as area increased. It indicated that there might be a threshold value of average area which cut off the pattern, which was consistent with the results from a similar study (Zhang et al., 2013). Shannon entropy did not show any correlation with

any of the indicators or features. It made sense because it described the distribution of the likelihoods, which, due to equifinality, were almost uniformly displayed for each basin (Beven and Binley, 1992). That was also reflected in the relations between NSE and feasible model parameter distributions, as shown in Figure 30, which was an example of equifinality of basin ‘SanjacintoP2’. Other basins showed identical results, where marginal likelihoods of the model parameters showed equal weights within the parameter range. Above all, for the pivot model, NSE and relative width exhibited no specific trend regarding different basins.

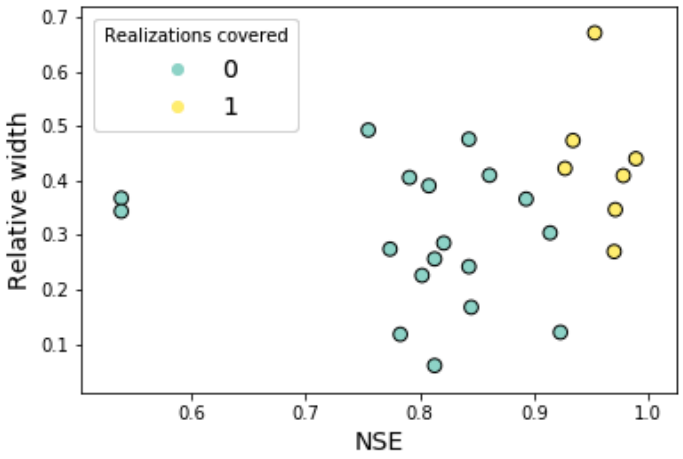

Figure 28 Relations between indices and realizations covered

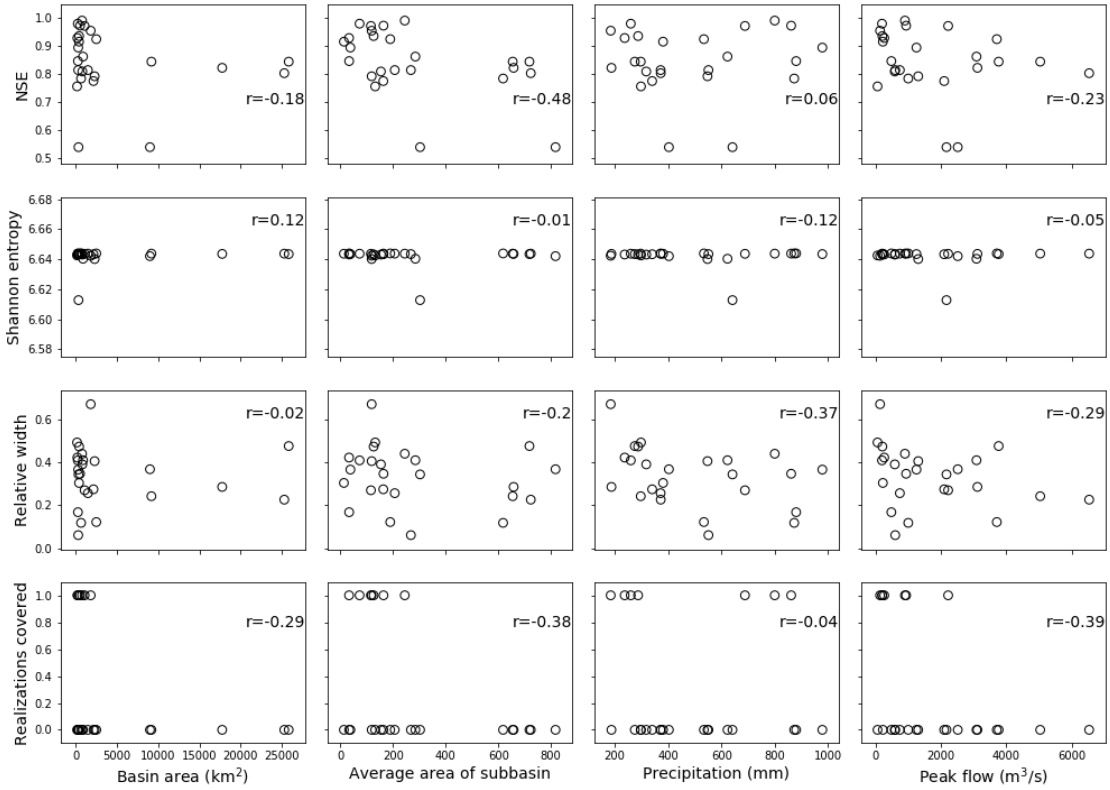

Figure 29 Relations between indices and basin features

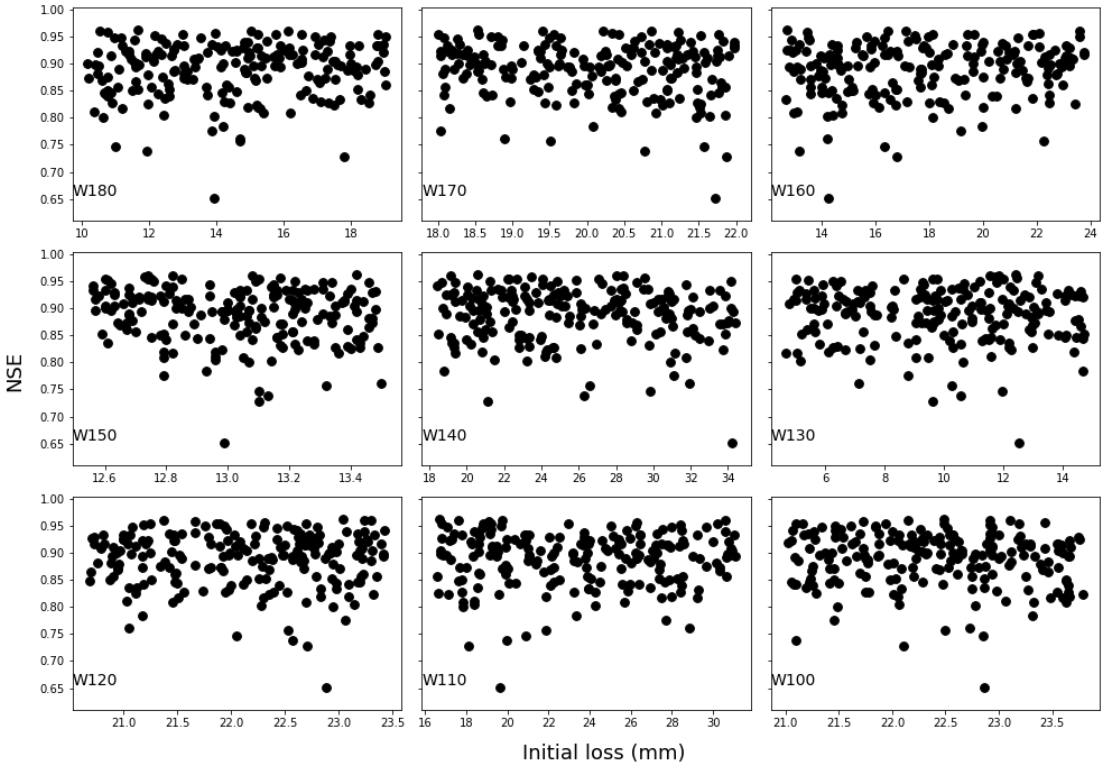

Figure 30 NSE VS. initial loss of subbasins in basin 'SanjacintoP2'

4.3.2 Comparison of 2K, 5K, and 10K Models

Based on the 2K-IC-Observed model, precipitation of 2K NEXRAD grid size was substituted by precipitation values of 5K and 10K NEXRAD grid sizes. Other modules of the model were kept unchanged. Performances and uncertainties of the three models were compared and analyzed. The 5K and 10K models showed similar trends and relationships with 2K model as described in section 4.3.1. However, some indices of the model changed with the variation of NEXRAD grid size. Figure 31 shows that the average precipitation (total amount of precipitation in a basin divided by basin area) of 25 basins increased as the gird size increased. The original NEXRAD grid size was 4K

and we mosaiced it into 2K, 5K, and 10K using a bilinear resampling technique from ArcGIS. The reason for the increasing amount of precipitation might be due to the algorithm of bilinear resampling, which performed a bilinear interpolation and determined the new value of a cell based on a weighted distance average of the four nearest input cell centers. However, we could see that the amount of change was almost invisible (487.8 - 488.7 mm). Thus, the impact due to grid size difference but not precipitation intensity change can be detected. The average NSE of 25 basins decreased as the grid size increased. It is noted that in Figure 32, which showed the percentage change of NSE and relative band width of each individual basin, some of the basins had increased NSE, which made it hard to explain the overall relationship between the change of NSE and grid size. However, most of the basins (21 out of 25) had NSE variation within 10%.

On the contrary, the average relative band width of 25 basins increased as the grid size increased. At the same time, as shown in Figure 32, the relative width increased with the grid size increase for all individual basins. Besides, the change percentage declined with increased basin area, average area of subbasins, and observed peak flow. This means that the uncertainty due to the change of precipitation grid size is more sensitive to smaller basin area, average area of subbasin, and observed peak flow. In other words, it had less effect on extreme event modeling than on normal event modeling, since extreme event modeling is usually associated with bigger basin area, average area of subbasin, and observed peak flow. A polynomial curve (in the form of: y=ax^b+c) was fitted to the relationship between the change of relative band width and

features. The coefficients and coefficient of determination (R^2) are summarized in Table 6.

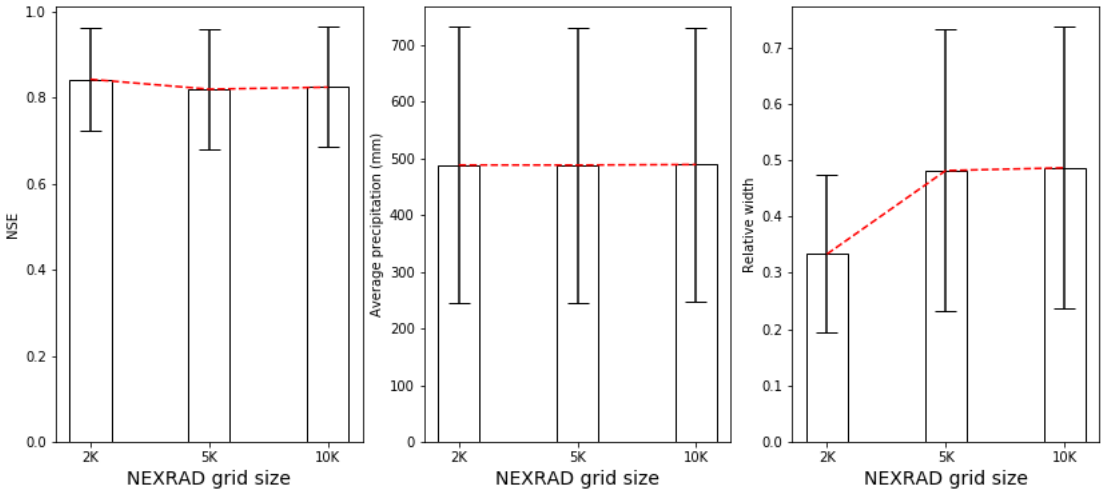

Figure 31 Average NSE, precipitation and relative width of 25 basins with variation of NEXRAD grid size

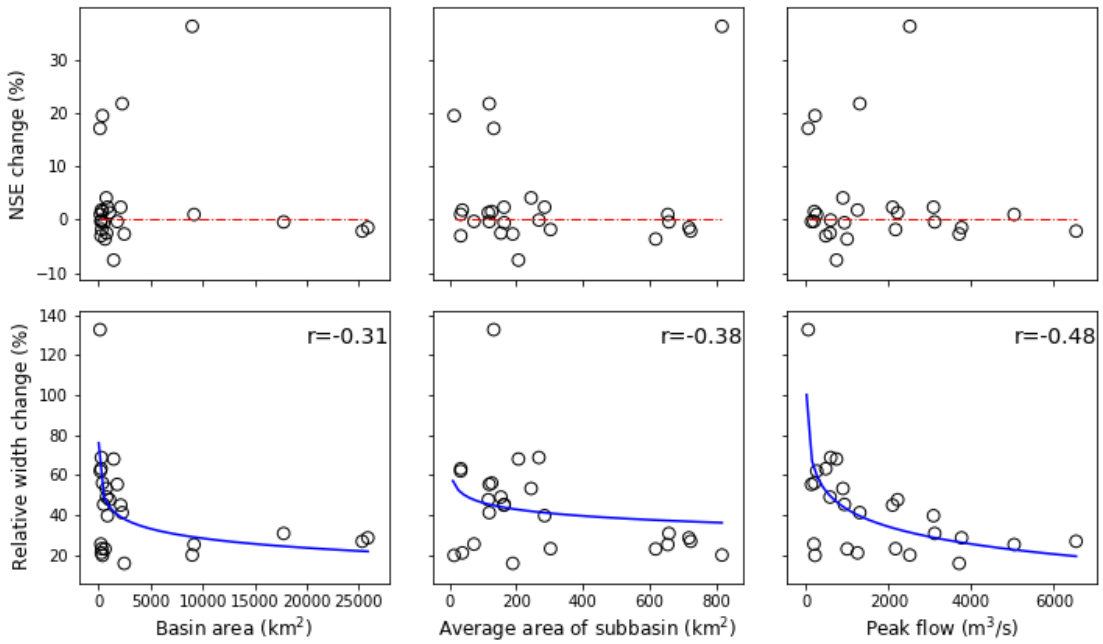

Figure 32 Percentage of individual change ((5K-2K)/2K*100, e.g., positive percentage indicated that NSE of 5K model was bigger than that of 2K model, vice versa) of NSE and relative width due to change of NEXRAD grid size versus. basin area, average area of subbasin, and peak flow

Table 6 Coefficients and coefficient of determination of fitted curves for the relationship between percent change of relative width with basin features

Coefficients	Basin area VS. Relative width change	Average area of subbasin VS. Relative width change	Peak flow VS. Relative width change
a	-66411.91	78048.39	-131800.24
b	1.04×10^{-4}	6.08×10^{-5}	9.44×10^{-5}
c	66503.80	-77980.35	131929.04
R^2	0.19	0.04	0.40

4.3.3 Comparison of IC and SCS Models

Based on the 2K-IC-Observed model, the SCS loss method was applied to the model in place of the IC loss method. Other modules of the model were kept unchanged. The performances and uncertainties of the two models were compared. Three basins had

NSEs below 0 after SCS model calibration and were not included in the following analysis. The names and features of these basins are shown in Table 7. It can be seen that all of those basins had larger basin areas, subbasin numbers, and average area of subbasins than those from the other basins. The main reason might be that the SCS method was derived for small watersheds, it has mainly been used for small agricultural, forest, or urban watersheds (Xiao et al., 2011; Walega et al., 2020). Figure 33 shows the average NSE and relative band width of 22 basins from the two different models. The average NSE of IC model was higher than that of the SCS model. However, the standard deviation of SCS model was bigger. The IC model had a smaller average relative band width and standard deviation. It can also be seen from Figure 34 that not all IC models had higher NSE, but all IC models had smaller relative width. Figure 34 shows the differences of NSE and relative width of individual IC and SCS models (not including the 3 collapsed models) plotted against basin area, average area of subbasin, peak flow, and average precipitation. There were 9 IC models which had higher NSE, however, the 3 collapsed models were not counted. It was noted that for small basin areas (area less than 3000 km^2), either IC or SCS models could result in higher or lower NSEs, while for large basin areas, including the 3 basins shown in Table 7, the SCS models had poorer performances (lower NSE or collapsed). The same pattern was true with the relationship between NSE and average area of subbasins. In this study, the basin area and average area of subbasins had no correlation, as shown in Table 5. However, the models which had larger average area of subbasins still performed poorer with the SCS method. The reason was the same as the reason for certain models that collapsed.

Figure 34 shows that as basin area, average area of subbasins, peak flow, and average precipitation increased, the difference of relative widths between IC and SCS models declined. Similar to different NEXRAD grid size models, the uncertainty due to the difference of model structures was more sensitive to smaller basin area, average area of subbasins, observed peak flow, and average precipitation. In other words, it had less effect on extreme event modeling than on normal event modeling, since extreme event modeling is usually associated with large basin area, average area of subbasin, observed peak flow, and average precipitation. A polynomial curve (in the form of: y=ax^b+c) was fitted to the relationship between relative width difference and features. The coefficients and coefficient of determination (R^2) are summarized in Table 8.

Table 7 Collapsed basins during SCS model calibration

Basin name	Basin area (km^2)	Subbasin number	Average area of subbasin	Precipitation (mm)	Peak flow (m^3/s)
Brazos	25858.37	36	718.29	275.4	3763.9
Neches	25321.07	35	723.46	372.6	6537.3
Trinity	17770.84	27	658.18	187.9	3113.0

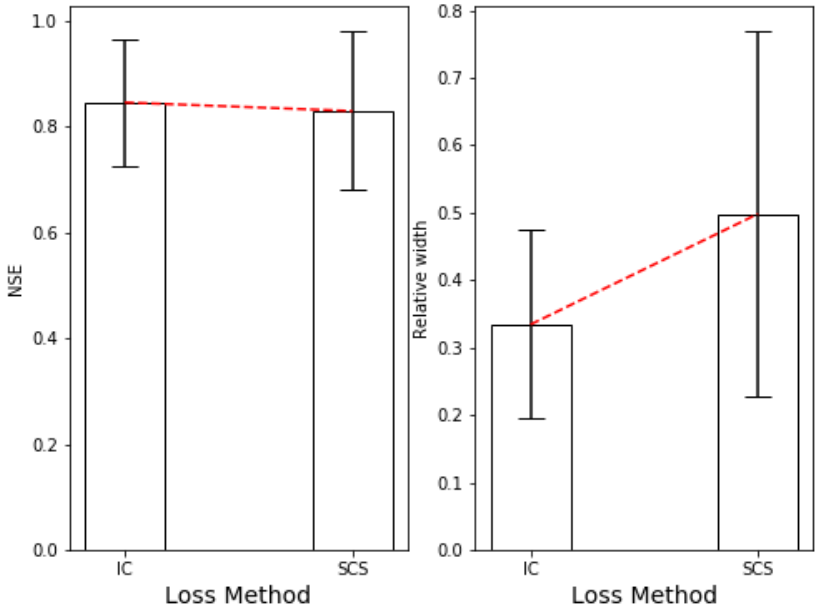

Figure 33 Average NSE and relative width of 22 basins for IC and SCS models

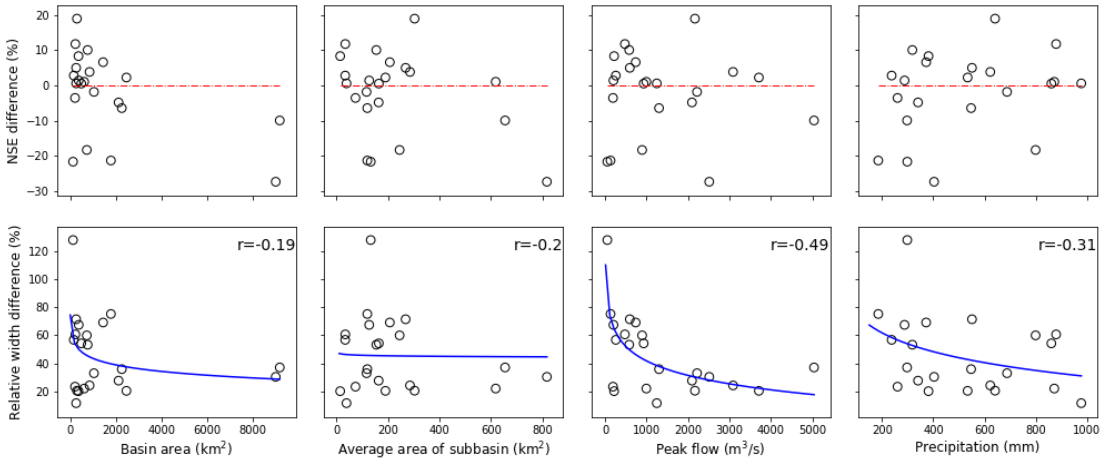

Figure 34 Percentage of individual difference ((SCS-IC)/IC*100, e.g., positive percentage indicated that NSE of SCS model was bigger than that of IC model, vice versa) of NSE and relative width between two loss method models versus basin area, average area of subbasin, peak flow and precipitation.

Table 8 Coefficients and coefficient of determination of fitted curves for the relationship between the difference of IC and SCS models and basin features

Coefficients	Basin area VS. Relative width difference	Average area of subbasin VS. Relative width difference	Peak flow VS. Relative width difference	Precipitation VS. Relative width difference
A	-44021.99	7721.40	-135364.42	-35258.88
B	1.52×10^{-4}	-6.93×10^{-5}	1.09×10^{-4}	5.44×10^{-4}
C	44111.73	-7673.12	135508.33	35422.34
R^2	0.09	0.0004	0.44	0.12

4.3.4 Comparison of 2K-IC-Observed and 2K-IC-Biased Models

Based on the 2K-IC-Observed model, biased observed discharge flow was used to calibrate the model in place of the original observed true discharge flow. Other modules of the model were kept unchanged. The performances and uncertainties of the two models were compared. Figure 35 shows the average NSE and relative band width of 25 basins for 2K-IC-Observed and 2K-IC-Biased models. The average NSE of 2K-IC-Biased models was slightly smaller but had bigger standard deviation. Figure 36 shows that most of the basins (23 out of 25) had NSE differences within 5%. There was no evidence to indicate better or poorer performances between the two models. The only exception with the difference of 42% was basin 'Colorado'. The reason of this 'outlier' might be that even for the pivot model, the NSE of 'Colorado' (NSE=0.539) was much lower than the average (0.843). With a poor performance in the pivot model, adding noise to discharge might make the situation worse. It was interesting to see that basin 'SanjacintoP6' had poor performance in the pivot model as well (NSE=0.539). However, the difference of NSE between the two models of this basin was only 0.07%. It was noted that 'SanjacintoP6' had much smaller basin area and average area of subbasins than 'Colorado', which means that besides the initial NSE value, basin area, and average

area of subbasins are also factors affecting the NSE difference between the two models. The average relative width of 25 basins was bigger in the 2K-IC-Biased model, with a bigger standard deviation. On the contrary to NSE differences, all individual basins showed increased relative band width in the 2K-IC-Biased model, as shown in Figure 36. It was interesting that the patterns shown in the figure were identical with models with different NEXRAD grid scale and loss methods (described in section 4.3.2 and 4.3.3). With basin area, the average area of subbasin, peak flow, and average precipitation increase, the difference of relative band widths between the two models declined which means that uncertainty due to biases introduced by discharge (model input) was more sensitive to smaller basin area, average area of subbasin, observed peak flow, and average precipitation. In other words, it had less effect on extreme event modeling than on normal event modeling, since extreme event modeling is usually associated with large basin area, average area of subbasin, observed peak flow, and average precipitation. A polynomial curve (in the form of: y=ax^b+c) was fitted for the relationship between relative width difference and basin features. The coefficients and coefficient of determination (R^2) are summarized in Table 9.

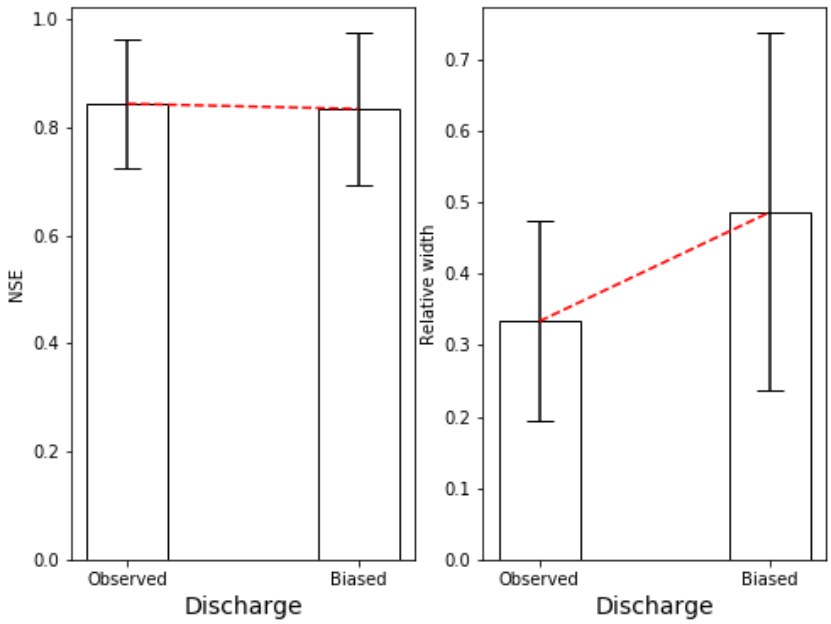

Figure 35 Average NSE and relative width of 25 basins for 2K-IC-Observed and 2K-IC-Biased model

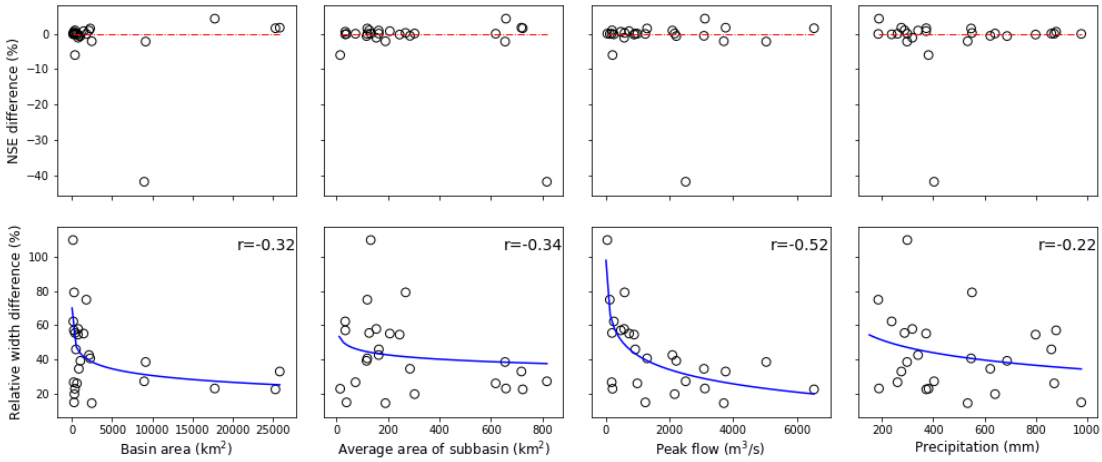

Figure 36 Percentage of individual difference ((Biased-Observed)/Observed*100, e.g., positive percentage indicated that NSE of 2K-IC-Biased model was bigger than that of 2K-IC-Observed model, vice versa) of NSE and relative width between two models versus basin area, average area of subbasin, peak flow, and precipitation.

Table 9 Coefficients and coefficient of determination of fitted curves for the relationship between relative band width difference of 2K-IC-Observed and 2K-IC-Biased models and basin features

Coefficients	Basin area VS. Relative width difference	Average area of subbasin VS. Relative width difference	Peak flow VS. Relative width difference	Precipitation VS. Relative width difference
A	-34516.36	52157.77	-93349.40	-8268.60
B	$1.65x10^{-4}$	$-6.88x10^{-5}$	$1.29x10^{-4}$	$1.27x10^{-3}$
C	34599.56	-52096.06	93475.02	8375.96
R^2	0.16	0.03	0.45	0.06

4.3.5 Model Validation and Posterior Parameter Update

The validation of models used hurricane Patricia which had only about 1/3 precipitation (average proportion of basins) fell in the study area. Even though the two storms are all tropical, their paths were different. Hurricane Harvey started and reformed over the Bay of Campeche and made a landfall along the middle Texas coast, while hurricane Patricia started from the south of Mexico and weakened substantially before making a landfall along the coast of southwestern Mexico. This means that Harvey brought rainfall from atmosphere above basin outlet to upper parts of the basins, while Patricia brought rainfall from atmosphere above upper basins to basin outlets. Mohamadi and Kavian (2015) found that different intensities and patterns of rainfall resulted in significantly different runoff and soil loss. Thus, it is believed that different patterns and intensities of the two events will result in different model parameters. Specifically, most of the calibrated models will overestimate the runoff of Patricia. Taking ‘Lavaca450’ as an example, in Figure 37, the simulated hydrograph using calibrated parameters from Harvey overestimated the volume and peak flow. However, the shape and timing of the

hydrograph were almost identical to the observed hydrograph. Thus, we could infer that the mismatch was mainly due to the parameters from the loss method. The loss method was initial and constant loss method, which comprised two parameters: initial loss and constant loss rate. The initial loss was decided mainly by the land use classification and loss rate was determined by soil type. For different events, the land use classification would not change dramatically, while according to Mohamadi and Kavian (2015), the soil loss and runoff might change significantly. Thus, the validation of the model using loss rate calibrated by another significantly different storm caused notable mismatch. To implement it, we recalibrated the Patricia model with change of only the loss rate parameter (other parameters were from Harvey model and were kept still). The calibrated hydrograph showed even higher NSE (0.987) than that from Harvey model. It showed that the validation of the model had sufficient accuracy of prediction with proper adjustment of loss rate. Thus, the models were validated adequately for modeling the extreme event. For further study, the relationship between the loss rate and storm rainfall intensity can be explored and then applied to future model construction and validation.

In the GLUE method, Bayesian framework can be used to infer the posterior distributions of model parameters. Taking 'Lavaca503' as an example, Figure 38 shows how posterior distributions of initial loss were updated after calibration of Harvey and validation of Patricia (W60, W50 and W40 are subbasins of 'Lavaca503'). A uniform prior distribution of initial loss was assigned to each subbasin, shown as the solid black line. After the calibration of Harvey, we filtered half of the ensembles out, and equations (47) and (48) were applied to the left half for posterior distribution after Harvey. The

same procedure was used after the validation of Patricia, where the posterior distribution from Harvey became the prior distribution of Patricia. In Figure 38, it is shown that after two storms being involved in the procedure, the CDF of parameters changed. In this case, subbasin W50 and W40 changed slightly for both calibration and validation periods, while W60 changed dramatically after the validation of Patricia. In this section, it might be due to the impact of intensities and patterns of rainfall. Above all, this Bayesian procedure indicated that with more information of storms becoming available, more information of the hydrologic response could be revealed.

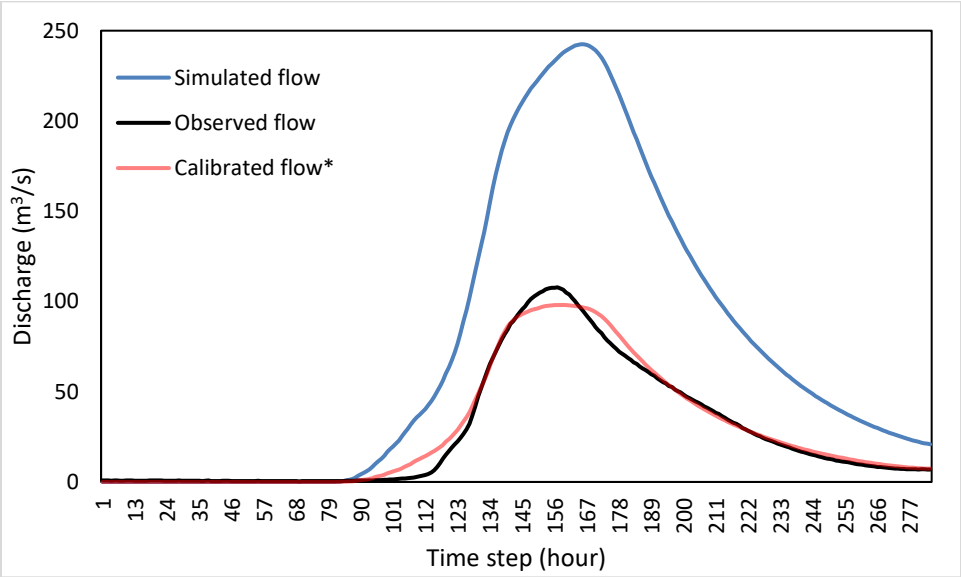

Figure 37 Validation hydrographs of Patricia in 'Lavaca450'.
*This calibration only calibrated loss rate of the basin, other parameters were from hurricane Harvey and kept still.

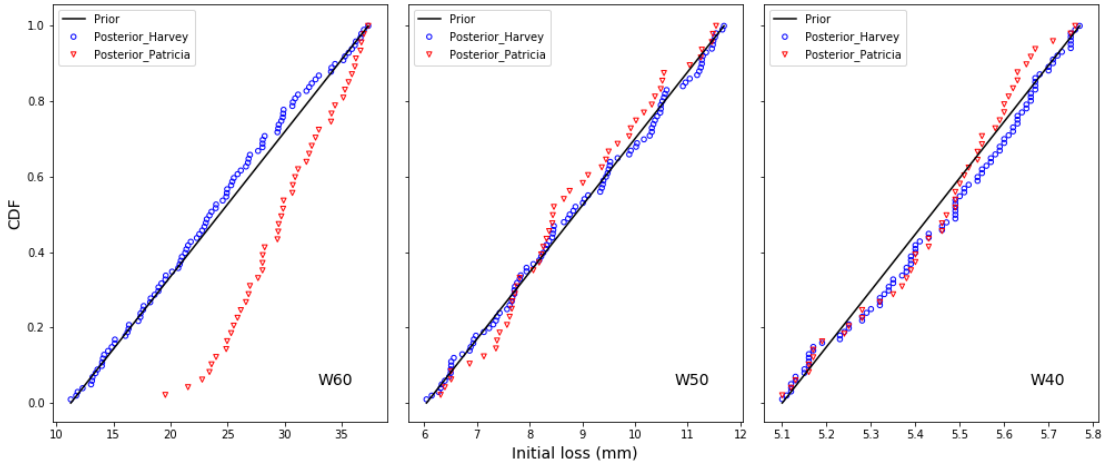

Figure 38 CDF update of posterior distribution of initial loss after calibration and validation for basin 'Lavaca503'.

4.3.6 Probable Maximum Flood with Uncertainty

PMF is derived by the following procedure: First, average point PMP value of 25900 km^2 was obtained from Chapter II. Second, apply the PMP values to the HMR 52 procedure to design the PMS described in Chapter III. Third, route the PMS with the R-R model from the previous study to derive the final PMF hydrograph. The following section showed the application of the R-R model with PMS to derive PMF with uncertainty in the lower Brazos River basin.

As shown in figure 1, the uncertainty of PMF rooted from three sources: uncertainty from PMP, PMS and R-R models. While in section 3.1.4, we decided not to pursue the uncertainty of PMS due to the huge burden of numerical sampling and the deterministic feature of designing PMS. Thus, the PMF uncertainty was accumulated from PMP to R-R model uncertainty, with PMS design procedure as a medium. First, the PMP with 95% confidence interval bound values (upper bound and lower bound) were transferred to PMFs with the PMS design procedure and the R-R model. Then, for the

upper bound and lower bound PMP CI values, the R-R models were run for 200 times with uniformly distributed parameter sets, where the bounds were ±10% of the optimum parameter values calibrated from hurricane Harvey. At last, the PMF hydrographs involving both uncertainty from PMP and R-R model were presented.

According to Chapter II, the PMP values of rainfall stations were assumed to follow a normal distribution. The 1-hr point PMP with standard deviation and confidence intervals (CI) within the study area (rainfall stations showed in figure 16) were summarized in table 10.

The average PMP value and CI were applied to design the PMSs with the relations built in section 3.1.3. Then, the PMSs were introduced to the R-R model and ran with the optimum model parameter set calibrated from hurricane Harvey to get PMFs. In figure 39, the peak discharge of PMF derived by the average PMP value (12716 CMS) was three times of the peak discharge value of hurricane Harvey (3764 CMS). While the average areal precipitation amount of PMS in the study area was 508 mm, which was also around three times of that from hurricane Harvey (169 mm). Appendix C showed detailed calculation of precipitation amounts of PMS and hurricane Harvey. The upper and lower bounds PMF were derived from the upper and lower bounds of 95% CI of PMP, respectively. The PMP CI (54.5 mm) resulted in 3656 CMS of difference (10890-14546 CMS) in the PMF peak discharge. In addition, 100 sets of model parameters considered as acceptable simulators from Chapter III in the study area were used to run the R-R model with bounds of PMP CI. Each of the 100 sets of hydrographs were shown with shallow red and blue shades in figure 39, which

represented the results considering the R-R model uncertainty. The peak flow range of lower and higher bound PMF were 10471-11231 CMS and 13976-14991 CMS, respectively. For peak flow, the PMP uncertainty accounted for 81% of the total uncertainty, while the R-R model uncertainty only accounted for 19%.

Table 10 1-hr point PMP values, standard deviation, lower bound and upper bound confidence interval of rainfall stations within the study area.

Station name	1-hr point PMP (mm)	Standard deviation (mm)	Lower bound CI (mm)	Upper bound CI (mm)
Bay city	193.6	11.8	170.4	216.7
Belton	232.6	13.0	207.2	258.1
Bertnam	266.4	20.0	227.3	305.5
Briggs	227.0	9.8	207.8	246.1
Groesbeck	221.9	14.8	192.8	250.9
Houston addicts	268.2	13.3	242.1	294.2
Houston alife	285.1	11.3	263.0	307.2
Jewett	294.9	19.4	257.0	332.9
Lexington	179.0	7.6	164.2	193.8
Spicewood	281.0	16.2	249.3	312.7
Still house	229.0	16.5	196.6	261.4
Thompson	231.6	18.6	195.2	267.9
Waco dam	220.5	16.3	188.5	252.5
Waco regional airport	183.3	11.9	160.0	206.5
Washington	202.1	9.6	183.3	220.9
Wheelock	255.0	12.6	230.2	279.8
Average	235.7	13.9	208.4	262.9

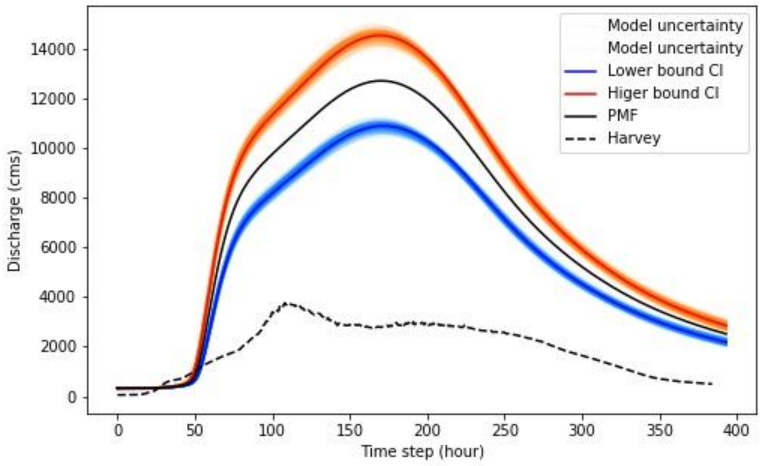

Figure 39 PMF hydrograph with uncertainty in lower Brazos River basin

CHAPTER V

CONCLUSION

This study investigated beginning with PMP to PMS and R-R modeling of extreme events, and developed a complete structure for the estimation of PMF with a focus on uncertainty quantification. The framework was implemented with a case study in Brazos River basin, Texas, United States.

Chapter II of this study developed a basin-scale model for calculating PMP and quantifying the uncertainties, which included the uncertainties caused by *K*, X_n and S_n, in the Hershfield method. The delta method and bootstrap method were used to quantify the uncertainties. The average PMP values for 1-hour, 6-hour and 24-hour durations were 177.8 mm, 342.9 mm, and 515.9 mm, respectively. The estimated standard errors were approximately 10% of the PMP values. The PMP values at each station followed the normal distribution and confidence intervals were 4.59%, 5.69% and 5.90% of PMP values for each duration. Except for 1-hour PMP map, which showed no obvious trend in the spatial distribution, the other two duration PMPs showed declining trends from east coast to west (inland). The basin-scale PMP values were more consistent with TCEQ results than those of the Hershfield method, and the delta method was more valid than the Salas method in quantifying uncertainties. The proposed model was found to be more robust than the Hershfield method and the Salas method for quantifying uncertainties for basin-scale application. Further studies are needed to extend the proposed model to other meteorologically homogeneous basins.

Chapter III refereed to HMR 52 for PMS design, updated the historical storm records within and around Texas and eventually developed a 72-hr PMS for lower Brazos River basin. The DAD curves were first derived from historical storm records. The records with storm area larger than 50000 km^2 showed fluctuating DAD curves which means that those data were less reliable. When storm area was larger than 5000 km^2, the precipitation depth dropped under 50% of the point depth. With the storm duration increase, the depth drop became smaller. From the relationship between duration and precipitation depth, the PMP values increased with the duration increase. For a specific duration, the larger storm area PMP had a bigger value. The DAD relations were used to interpolate PMP values for all durations and storm areas. The updated storm records suggested that the WWSDA relation introduced by HMR 52 was not necessarily true. Except for the area size that gives PMP, the within-storm depth-area relation from the updated storm records can give depths bigger than PMP for smaller area sizes, which is opposed to the relation stated by HMR 52. Hyetographs for the entire study area of a 72-hr PMS event were finally constructed with the application of DAD and WWSDA to the PMP values.

Chapter IV revisited hurricane Harvey, which is the wettest and second costliest tropical cyclone in the United States, and used it to calibrate the R-R model for extreme events in Texas. It traced back all the uncertainty sources in building an R-R model with the framework of GLUE method, analyzed model performance and uncertainty across different basins, and investigated the impact of extreme event features (larger basin area, intensive precipitation, and critical peak flow) on different sources of uncertainty

implemented by different models. Different R-R models based on different sources of uncertainties were constructed and applied to 26 independent watersheds in Texas near the Gulf of Mexico. With GLUE methodology, the impacts of different sources of uncertainty on model performance and uncertainty were investigated. The models with various structures and accuracies of precipitation and discharge were: 2K-IC-Observed (pivot model), 5K-IC-Observed, 10K-IC-Observed; 2K-SCS-Observed, and 2K-IC-Biased models. For the pivot model, the Nash-Sutcliffe Efficiency (NSE) of 25 basins ranged from 0.54 to 0.99 and showed a negative relation (r=-0.48) with the average area of subbasins, while there might be a threshold value between 300-600 km^2. The entropy values were almost identical across the basins (≈6.644) due to equifinality. The relative width ranged from 0.06 to 0.67 and showed a weak negative relation with precipitation (r=-0.37) and peak flow (r=-0.29). Comparison of different models with the pivot model showed that 1) NSE had no particular pattern of increase or decrease; 2) all other models showed increased relative width; and 3) uncertainties were more sensitive to smaller basin area, average area of subbasin, precipitation intensity, and observed peak flow, which means that for extreme event modeling with opposite basin features, the selection of model input and model setup had less impact on model performance and uncertainty. The R-R model with uncertainty analysis was then used to route the PMS from Chapter III to obtain PMF with uncertainty.

In lower Brazos River basin, the peak discharge of PMF derived by the average PMP value (12716 CMS) was around three times the peak discharge value of Harvey (3764 CMS). While the average areal precipitation amount of PMS in the study area was

508 mm, which was also around three times that from hurricane Harvey (169 mm). This comparison showed that even hurricane Harvey brought the most severe rainfall to the area in the history, it was still much less than the peak flow that PMF could have potentially brought to the area. The PMP CI (54.5 mm) resulted in 3656 CMS of difference (10890-14546 CMS) in the PMF peak discharge. For the peak flow uncertainty, PMP uncertainty accounted for most of the parts (81%), while the R-R model uncertainty accounted for less (19%). This study provided a thorough framework for quantifying the uncertainty of PMF and can be used in other areas of interest. Further studies like PMF inundation mapping with uncertainty is also of high interest.

REFERENCES

Abbaspour, K. C., 2008. SWAT-CUP2: SWAT calibration and uncertainty programs–a user manual. Department of Systems Analysis. Integrated Assessment and Modelling (SIAM), Eawag, Swiss Federal Institute of Aquatic Science and Technology, Duebendorf, Switzerland.

Abbaspour, K. C., Johnson, C. A., & Van Genuchten, M. T., 2004. Estimating uncertain flow and transport parameters using a sequential uncertainty fitting procedure. Vadose Zone Journal, 3(4), 1340-1352.

Al Mamoon, A. and Rahman, A., 2014. Uncertainty in design rainfall estimation: A review. J. Hydrol. Environ. Res, 2(1), pp.65-75.

Alaya, B., Zwiers, F. and Zhang, X., 2018. Probable maximum precipitation: its estimation and uncertainty quantification using bivariate extreme value analysis. Journal of Hydrometeorology, 19(4), pp.679-694.

Aronica, G., Bates, P. D., & Horritt, M. S., 2002. Assessing the uncertainty in distributed model predictions using observed binary pattern information within GLUE. Hydrological processes, 16(10), 2001-2016.

Arsenault, R., Poulin, A., Côté, P., & Brissette, F., 2014. Comparison of stochastic optimization algorithms in hydrological model calibration. Journal of Hydrologic Engineering, 19(7), 1374-1384.

Benson, M. A., 1973. Thoughts on the design of design floods. IN: FLOODS AND DROUGHTS.

Beven, K., & Binley, A., 1992. The future of distributed models: model calibration and uncertainty prediction. Hydrological processes, 6(3), 279-298.

Beven, K., & Freer, J., 2001. Equifinality, data assimilation, and uncertainty estimation in mechanistic modelling of complex environmental systems using the GLUE methodology. Journal of hydrology, 249(1-4), 11-29.

Bill K., Geoff M., Doug H., Dana M., Kristi S., Bryon L. and Jacob R., 2016. Probable Maximum Precipitation Study for Texas [report]. Retrieved from https://www.tceq.texas.gov/compliance/investigation/damsafetyprog.html

Blake, E. S., & Zelinsky, D. A., 2018. National Hurricane center tropical cyclone report: Hurricane Harvey. National Hurricane Center, National Oceanographic and Atmospheric Association.

Blake, E. S., & Zelinsky, D. A., 2018. Tropical Cyclone Report: Hurricane Harvey.

Bo, X. I. A. O., Qing-Hai, W. A. N. G., Jun, F. A. N., Feng-Peng, H. A. N., & Quan-Hou, D. A. I., 2011. Application of the SCS-CN model to runoff estimation in a small watershed with high spatial heterogeneity. Pedosphere, 21(6), 738-749.

Booij, M. J., 2005. Impact of climate change on river flooding assessed with different spatial model resolutions. Journal of hydrology, 303(1-4), 176-198.

Cameron, D. S., Beven, K. J., Tawn, J., Blazkova, S., & Naden, P., 1999. Flood frequency estimation by continuous simulation for a gauged upland catchment (with uncertainty). Journal of Hydrology, 219(3-4), 169-187.

Casas, M.C., Rodríguez, R., Prohom, M., Gázquez, A. and Redaño, A., 2011. Estimation of the probable maximum precipitation in Barcelona (Spain). International Journal of Climatology, 31(9), pp.1322-1327.

Casas, M.C., Rodríguez, R., Prohom, M., Gázquez, A. and Redaño, A., 2011. Estimation of the probable maximum precipitation in Barcelona (Spain). International Journal of Climatology, 31(9), pp.1322-1327.

Casella G, Berger R L. Statistical inference, 2002. Pacific Grove, CA: Duxbury.

Chavan, S.R. and Srinivas, V.V., 2015. Probable maximum precipitation estimation for catchments in Mahanadi river basin. Aquatic Procedia, 4, pp.892-899.

Chen, X., Hossain, F. and Leung, L.R., 2017. Probable maximum precipitation in the US Pacific Northwest in a changing climate. Water Resources Research, 53(11), pp.9600-9622.

Clavet-Gaumont, J., Huard, D., Frigon, A., Koenig, K., Slota, P., Rousseau, A., Klein, I., Thiémonge, N., Houdré, F., Perdikaris, J. and Turcotte, R., 2017. Probable maximum flood in a changing climate: An overview for Canadian basins. Journal of Hydrology: Regional Studies, 13, pp.11-25.

Dariane, A. B., Javadianzadeh, M. M., & James, L. D., 2016. Developing an efficient auto-calibration algorithm for HEC-HMS program. Water resources management, 30(6), 1923-1937.

Desa, M.M.N. and Rakhecha, P.R., 2007, June. Extremes of the extreme observed 24-hour rainfalls in a tropical region–Peninsular Malaysia as a case. In

Proceedings of the 2nd International Conference on Managing Rivers in the 21st Century: Solution towards Sustainable River Basins, Kuching, Sarawak, Malaysia.

Devia, G.K., Ganasri, B.P. and Dwarakish, G.S., 2015. A review on hydrological models. Aquatic Procedia, 4, pp.1001-1007.

Dhar, O. N., Kulkarni, A. K., & Rakhecha, P. R., 1981. Probable maximum point rainfall estimation for the southern half of the Indian peninsula. Proceedings of the Indian Academy of Sciences-Earth and Planetary Sciences, 90(1), 39-46.

Dingman, S. L., 1994. Physical Hydrology Prentice Hall. Inc., New Jersey, 7458.

Douglas, E.M. and Barros, A.P., 2003. Probable maximum precipitation estimation using multifractals: application in the eastern United States. Journal of Hydrometeorology, 4(6), pp.1012-1024.

Efron, B., 1992. Bootstrap methods: another look at the jackknife. In Breakthroughs in statistics (pp. 569-593). Springer, New York, NY.

FEMA, 1998. Federal Emergency Management Agency, Mitigation Directorate, Integracy Committee on Dam Safety, October 1998. Federal Guidelines for Dam Safety: Selecting and Accommodating Inflow Design Floods for Dams, FEMA 94.

Freer, J., Beven, K., & Ambroise, B., 1996. Bayesian estimation of uncertainty in runoff prediction and the value of data: An application of the GLUE approach. Water Resources Research, 32(7), 2161-2173.

Fuentes-Andino, D., Beven, K., Halldin, S., Xu, C. Y., Reynolds, J. E., & Di Baldassarre, G., 2017. Reproducing an extreme flood with uncertain post-event information. Hydrology and Earth System Sciences, 21(7), 3597-3618.

Gabellani, S., Boni, G., Ferraris, L., Von Hardenberg, J. and Provenzale, A., 2007. Propagation of uncertainty from rainfall to runoff: A case study with a stochastic rainfall generator. Advances in Water Resources, 30(10), pp.2061-2071.

Gali, R. K., Douglas-Mankin, K. R., Li, X., & Xu, T., 2012. Assessing NEXRAD P3 data effects on stream-flow simulation using SWAT model in an agricultural watershed. Journal of Hydrologic Engineering, 17(11), 1245-1254.

Gangrade, S., Kao, S.C., Naz, B.S., Rastogi, D., Ashfaq, M., Singh, N. and Preston, B.L., 2018. Sensitivity of probable maximum flood in a changing environment. Water Resources Research, 54(6), pp.3913-3936.

Georgakakos, K. P., Seo, D. J., Gupta, H., Schaake, J., & Butts, M. B., 2004. Towards the characterization of streamflow simulation uncertainty through multimodel ensembles. Journal of hydrology, 298(1-4), 222-241.

Gillingham, K., Nordhaus, W., Anthoff, D., Blanford, G., Bosetti, V., Christensen, P., ... & Reilly, J., 2018. Modeling uncertainty in integrated assessment of climate change: a multimodel comparison. Journal of the Association of Environmental and Resource Economists, 5(4), 791-826.

Glickman, T.S. and Zenk, W., 2000. Glossary of meteorology. AMS (American Meteorological Society).

Hansen, E.M., Schreiner, L.C. and Miller, J.F., 1982. NOAA Hydrometeorological Report No. 52: Application of Probable Maximum Precipitation Estimates–United States East of the 105th Meridian.

HEC-HMS Technical Reference Manual, USACE, Davis, CA, USA, Mar. 2000. Accessed on Nov. 25, 2018. [Online]. Available: https://www.hec.usace.army.mil/software/hec-hms/documentation.aspx

HEC-HMS Users Manual, Version 4.2, USACE, Davis, CA, USA, Aug. 2016. Accessed on Nov. 25, 2018. [Online]. Available: https://www.hec.usace.army.mil/software/hec-hms/documentation.aspx

Hershfield, D. M., 1961. Estimating the probable maximum precipitation. Journal of the hydraulics Division, 87(5), 99-116.

Hershfield, D. M., 1965. Method for estimating probable maximum rainfall. Journal‐American Water Works Association, 57(8), 965-972.

Ichiba, A., Gires, A., Tchiguirinskaia, I., Schertzer, D., Bompard, P., & Veldhuis, M. C. T., 2018. Scale effect challenges in urban hydrology highlighted with a distributed hydrological model. Hydrology and Earth System Sciences, 22(1), 331-350.

Jennings, A.H., 1950. World's greatest observed point rainfalls. Monthly Weather Review, 78(1), pp.4-5.

Joshi, M., Seidel-Morgenstern, A., & Kremling, A., 2006. Exploiting the bootstrap method for quantifying parameter confidence intervals in dynamical systems. Metabolic engineering, 8(5), 447-455.

Koutsoyiannis, D., 1999. A probabilistic view of Hershfield's method for estimating probable maximum precipitation. Water resources research, 35(4), pp.1313-1322.

Lee, K. and Singh, V.P., 2020. Analysis of uncertainty and non-stationarity in probable maximum precipitation in Brazos River basin. Journal of Hydrology, 590, p.125526.

Lehbab-Boukezzi, Z., Boukezzi, L., & Errih, M., 2016. Uncertainty analysis of HEC-HMS model using the GLUE method for flash flood forecasting of Mekerra watershed, Algeria. Arabian Journal of Geosciences, 9(20), 751.

Liu, J., Shao, W., Xiang, C., Mei, C., & Li, Z., 2020. Uncertainties of urban flood modeling: Influence of parameters for different underlying surfaces. Environmental Research, 182, 108929.

Liu, Y. and Gupta, H.V., 2007. Uncertainty in hydrologic modeling: Toward an integrated data assimilation framework. Water resources research, 43(7).

Mejia, G. and Villegas, F., 1979. Maximum precipitation deviations in Colombia. In Proc., 3rd Conf. on Hydrometeorology (pp. 74-76).

Merz, R., Parajka, J., & Blöschl, G., 2009. Scale effects in conceptual hydrological modeling. Water resources research, 45(9).

Micovic, Z., Schaefer, M.G. and Taylor, G.H., 2015. Uncertainty analysis for probable maximum precipitation estimates. Journal of Hydrology, 521, pp.360-373.

Mirzaei, M., Huang, Y. F., El-Shafie, A., & Shatirah, A., 2015. Application of the generalized likelihood uncertainty estimation (GLUE) approach for assessing uncertainty in hydrological models: a review. Stochastic environmental research and risk assessment, 29(5), 1265-1273.

Mohamadi, M. A., & Kavian, A., 2015. Effects of rainfall patterns on runoff and soil erosion in field plots. International soil and water conservation research, 3(4), 273-281.

Montanari, A., 2005. Large sample behaviors of the generalized likelihood uncertainty estimation (GLUE) in assessing the uncertainty of rainfall‐runoff simulations. Water resources research, 41(8).

Moore, J.N., PE, C.E., Riley, R.C. and PE, W.P.S., 1993. Comparison of temporal rainfall distributions for near probable maximum precipitation storm events for dam design. In Proceedings of the 1993 Annual Conference of the Association of State Dam Safety Officials.

Moradkhani, H. and Sorooshian, S., 2009. General review of rainfall-runoff modeling: model calibration, data assimilation, and uncertainty analysis. In Hydrological modelling and the water cycle (pp. 1-24). Springer, Berlin, Heidelberg.

Moradkhani, H., & Sorooshian, S., 2009. General review of rainfall-runoff modeling: model calibration, data assimilation, and uncertainty analysis. In Hydrological modelling and the water cycle (pp. 1-24). Springer, Berlin, Heidelberg.

Moradkhani, H., Hsu, K. L., Gupta, H., & Sorooshian, S., 2005. Uncertainty assessment of hydrologic model states and parameters: Sequential data assimilation using the particle filter. Water resources research, 41(5).

Moradkhani, H., Sorooshian, S., Gupta, H. V., & Houser, P. R., 2005. Dual state–parameter estimation of hydrological models using ensemble Kalman filter. Advances in water resources, 28(2), 135-147.

Myers, V.A., 1967. The estimation of extreme precipitation as the basis for design floods Resume of practice in the United States.

Nearing, G.S., Tian, Y., Gupta, H.V., Clark, M.P., Harrison, K.W. and Weijs, S.V., 2016. A philosophical basis for hydrological uncertainty. Hydrological Sciences Journal, 61(9), pp.1666-1678.

Neuman, S. P., 2003. Maximum likelihood Bayesian averaging of uncertain model predictions. Stochastic Environmental Research and Risk Assessment, 17(5), 291-305.

Nobilis, F., Haiden, T. and Kerschbaum, M., 1991. Statistical considerations concerning probable maximum precipitation (PMP) in the Alpine country of Austria. Theoretical and applied climatology, 44(2), pp.89-94.

Ornes, S., 2018. Core Concept: How does climate change influence extreme weather? Impact attribution research seeks answers. Proceedings of the National Academy of Sciences, 115(33), 8232-8235.

Paulhus, J.L.H. and Gilman, C.S., 1953. Evaluation of probable maximum precipitation. Eos, Transactions American Geophysical Union, 34(5), pp.701-708.

Paulhus, J.L.H. and Gilman, C.S., 1953. Evaluation of probable maximum precipitation. Eos, Transactions American Geophysical Union, 34(5), pp.701-708.

Perrin, C., Michel, C., & Andréassian, V., 2001. Does a large number of parameters enhance model performance? Comparative assessment of common catchment model structures on 429 catchments. Journal of hydrology, 242(3-4), 275-301.

Rakhecha, P. R., & Soman, M. K, 1994. Estimation of probable maximum precipitation for a 2-day duration: Part 2—North Indian region. Theoretical and applied climatology, 49(2), 77-84.

Rezacova, D., Pesice, P. and Sokol, Z., 2005. An estimation of the probable maximum precipitation for river basins in the Czech Republic. Atmospheric research, 77(1-4), pp.407-421.

Roth, D., 2010. Texas hurricane history: National Weather Service, Camp Springs, Marlyand, 83 p.

Runkle, J., K. Kunkel, J. Nielsen-Gammon, R. Frankson, S. Champion, B. Stewart, L. Romolo, and W. Sweet, 2017: Texas State Climate Summary. NOAA Technical Report NESDIS 149-TX, 4 pp.

Salas, J. D., G. Gavilán, F. R. Salas, P. Y. Julien, and J. Abdullah. 2014. "Uncertainty of the PMP and PMF." In Handbook of engineering hydrology: Modeling, climate change, and variability, Book II, 575–603. Hoboken, NJ: Taylor & Francis.

Schreiner, L.C. and Riedel, J.T., 1978. Hydrometeorological Report No. 51: Probable Maximum Precipitation Estimates, United States East of the 105th Meridian. US Department of Commerce, National Oceanic and Atmospheric Administration and US Department of the Army, Corps of Engineers.

Schreiner, L.C. and Riedel, J.T., 1978. Probable maximum precipitation estimates, United States east of the 105th meridian (Vol. 55). Department of Commerce, National Oceanic and Atmospheric Administration.

Sherif, M., Almulla, M., Shetty, A., & Chowdhury, R. K., 2014. Analysis of rainfall, PMP and drought in the United Arab Emirates. International journal of climatology, 34(4), 1318-1328.

Singh, V. P., Yadav, S., & Yadava, R. N. (Eds.)., 2018. Hydrologic Modeling. Water Science and Technology Library. doi:10.1007/978-981-10-5801-1

Singh, V.P. and Strupczewski, W.G., 2002. On the status of flood frequency analysis. Hydrological Processes, 16(18), pp.3737-3740.

Task Committee on Hydraulic Modeling, Environmental and Water Resources Institute, ASCE, 2000, May. Hydraulic modeling: Concepts and practice. American Society of Civil Engineers.

Thiemann, M., Trosset, M., Gupta, H., & Sorooshian, S., 2001. Bayesian recursive parameter estimation for hydrologic models. Water Resources Research, 37(10), 2521-2535.

Vrugt, J. A., Diks, C. G., Gupta, H. V., Bouten, W., & Verstraten, J. M., 2005. Improved treatment of uncertainty in hydrologic modeling: Combining the strengths of global optimization and data assimilation. Water resources research, 41(1).

Vrugt, J. A., Gupta, H. V., Bastidas, L. A., Bouten, W., & Sorooshian, S., 2003. Effective and efficient algorithm for multiobjective optimization of hydrologic models. Water resources research, 39(8).

Vrugt, J. A., Gupta, H. V., Bouten, W., & Sorooshian, S., 2003. A Shuffled Complex Evolution Metropolis algorithm for optimization and uncertainty assessment of hydrologic model parameters. Water resources research, 39(8).

Wagener, T., & Gupta, H. V., 2005. Model identification for hydrological forecasting under uncertainty. Stochastic Environmental Research and Risk Assessment, 19(6), 378-387.

Wagener, T., McIntyre, N., Lees, M. J., Wheater, H. S., & Gupta, H. V., 2003. Towards reduced uncertainty in conceptual rainfall‐runoff modelling: Dynamic identifiability analysis. Hydrological processes, 17(2), 455-476.

Walega, A., Amatya, D. M., Caldwell, P., Marion, D., & Panda, S., 2020. Assessment of storm direct runoff and peak flow rates using improved SCS-CN models for selected forested watersheds in the Southeastern United States. Journal of Hydrology: Regional Studies, 27, 100645.

Willeke, G.E., 1979. Myths and uses of hydrometeorology in forecasting. In Proceedings Engineering Foundation Conference on Improved Hydrolic Forecasting, Why and How.

WMO (World Meteorological Organization), 1986. Manual for estimation of probable maximum precipitation. Operational Hydrology Report 1, 2nd Edition, Publication 332, Geneva.

WMO (World Meteorological Organization), 2009. Manual on estimation of probable maximum precipitation (PMP), WMO: No.1045, 259 pages.

Wurbs, R. A.; Bergman, C. E.; Carriere, P. E.; Walls, W. B., 1988. Hydrologic and institutional water availability in the Brazos River Basin. Texas Water Resources Institute.

Yu, Z., Lu, Q., Zhu, J., Yang, C., Ju, Q., Yang, T., ... & Sudicky, E. A., 2014. Spatial and temporal scale effect in simulating hydrologic processes in a watershed. Journal of Hydrologic Engineering, 19(1), 99-107.

Yu, Z., Wang, Y., Xu, H., Davidson, N., Chen, Y., Chen, Y. and Yu, H., 2017. On the relationship between intensity and rainfall distribution in tropical cyclones making landfall over China. Journal of Applied Meteorology and Climatology, 56(10), pp.2883-2901.

Zhang, H. L., Wang, Y. J., Wang, Y. Q., Li, D. X., & Wang, X. K., 2013. The effect of watershed scale on HEC-HMS calibrated parameters: a case study in the Clear Creek watershed in Iowa, USA. Hydrology & Earth System Sciences Discussions, 10(1).

Zhang, Y., Singh, V.P. and Byrd, A.R., 2019. Basin-scale statistical method for probable maximum precipitation with uncertainty analysis. Journal of Hydrologic Engineering, 24(2), p.04018067.

Zhou, Z., Liu, S., Hua, H., Chen, C. S., Zhong, G., Lin, H., & Huang, C. W., 2014. Frequency analysis for predicting extreme precipitation in Changxing Station of Taihu Basin, China. Journal of Coastal Research, 68(sp1), 144-151.

APPENDIX A

WITHIN/WITHOUT-STORM AVERAGE RATIO CURVE MAPS

Figure 20 (a-d) in the main text were constructed similar to Figure 13 as the preprocessing of the WWSDA relation. Figure 20 only showed (a) 1-hr, (b) 6-hr, (c) 24-hr and (d) 72-hr duration relations, the rest duration figures were shown in figure A1 (a-h). It showed the ratio of depth of various storm area (numerator) to the depth of a particular storm area (denominator) of a particular duration.

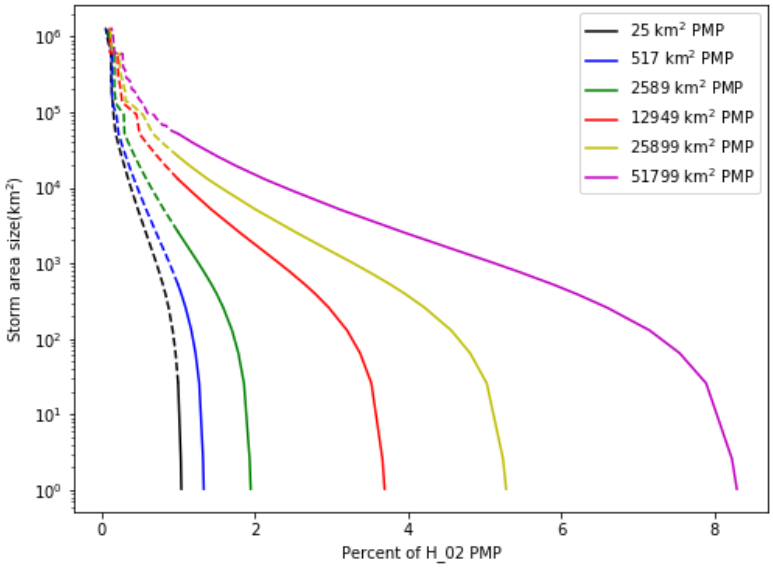
25 km² PMP
517 km² PMP
2589 km² PMP
12949 km² PMP
25899 km² PMP
51799 km² PMP
Storm area size(km²)
Percent of H_02 PMP

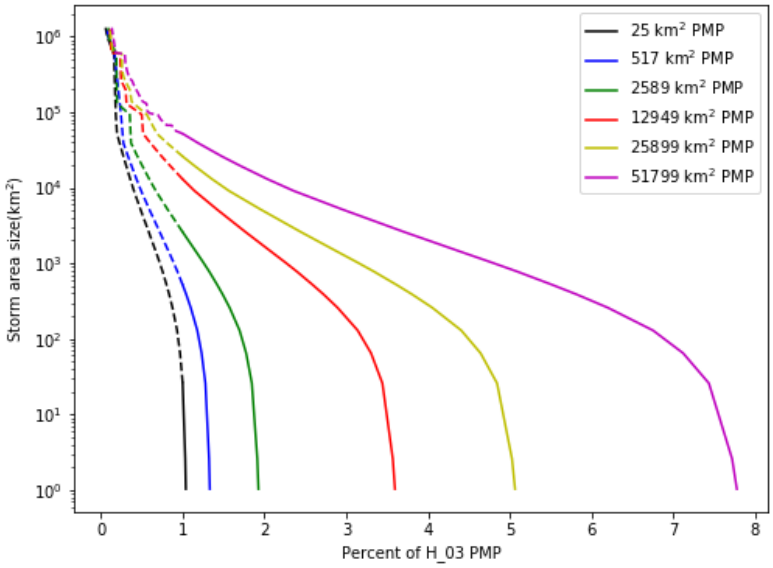
25 km² PMP
517 km² PMP
2589 km² PMP
12949 km² PMP
25899 km² PMP
51799 km² PMP
Storm area size(km²)
Percent of H_03 PMP

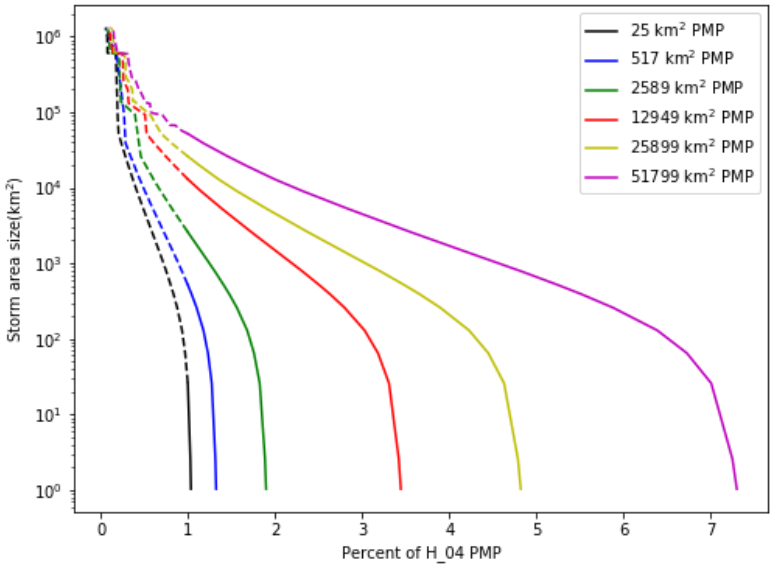
25 km² PMP
517 km² PMP
2589 km² PMP
12949 km² PMP
25899 km² PMP
51799 km² PMP
Storm area size(km²)
Percent of H_04 PMP

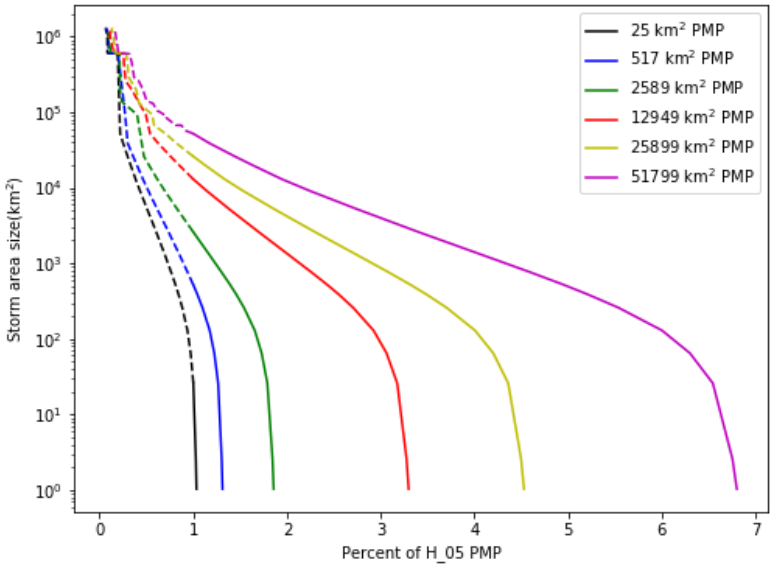
25 km² PMP
517 km² PMP
2589 km² PMP
12949 km² PMP
25899 km² PMP
51799 km² PMP
Storm area size(km²)
Percent of H_05 PMP

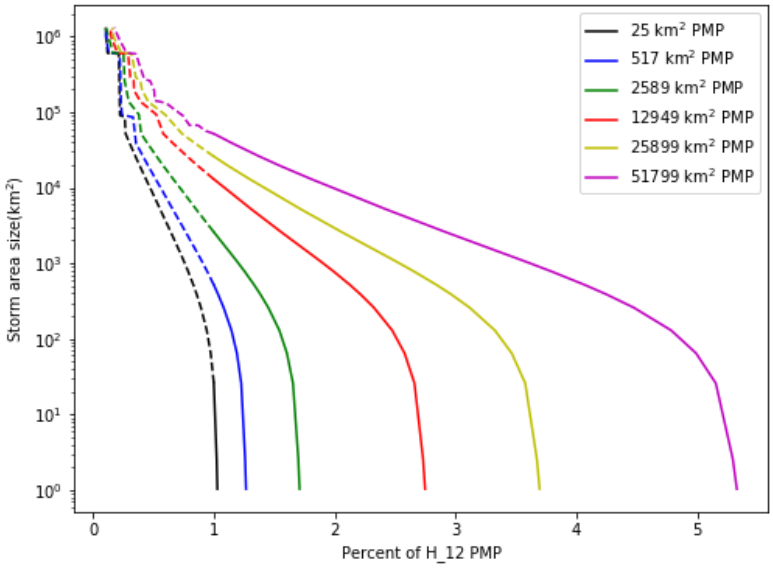
25 km² PMP
517 km² PMP
2589 km² PMP
12949 km² PMP
25899 km² PMP
51799 km² PMP
Storm area size(km²)
Percent of H_12 PMP

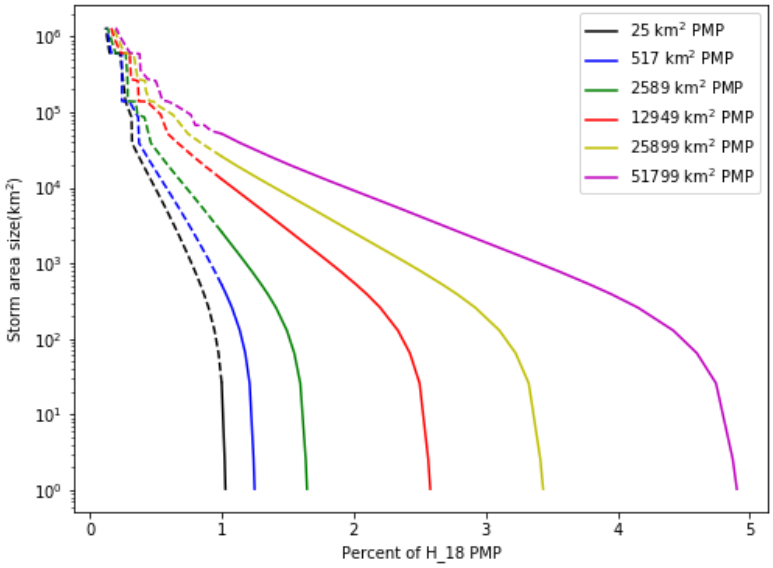
25 km² PMP
517 km² PMP
2589 km² PMP
12949 km² PMP
25899 km² PMP
51799 km² PMP
Storm area size(km²)
Percent of H_18 PMP

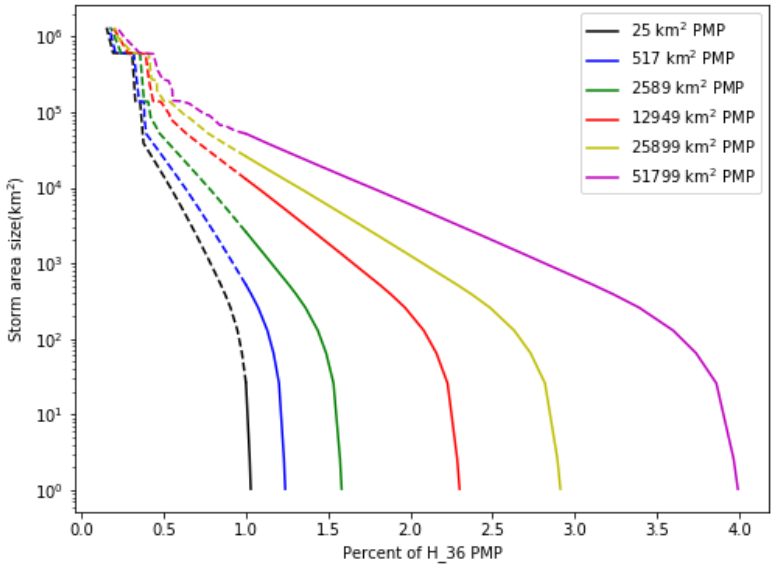

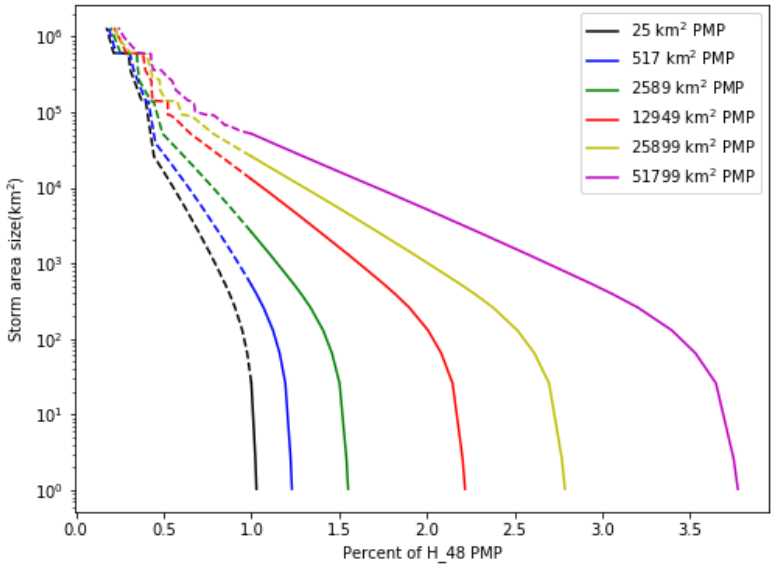

Figure A1 Within/without-storm average curves for standard area sizes of (a) 2-hr, (b) 3-hr, (c) 4-hr, (d) 5-hr, (e) 12-hr, (f) 18-hr, (g) 36-hr and (h) 48-hr duration.

APPENDIX B

RAINFALL-RUNOFF MODEL: WATERSHED HYDROLOGICAL CHARACTERISTICS AND PARAMETER ESTIMATION

In this study, the generation of sub-basins and reaches by HEC-GeoHMS is not discussed here. The detailed procedure for preparing the sub-basin divisions and reaches can be found in HEC-GeoHMS User's Manual (Version 10.1, 2013). Some of the initial parameter values shown in table 4 (e.g. drainage area, time of concentration, reach length, and energy grade) were generated, based on physical features during the procedure. The other parameters were estimated from observed data and calculations (e.g., CN values, impervious percentage, roughness coefficient, initial base flow, initial abstraction, linear reservoir constant, exponential decay constant, bottom width, and side slope). Calibration was done by the default optimization algorithm (Nelder Mead and Univariate Gradient) in HEC-HMS. Since it was an event-based simulation, we focused more on the peak flow which resulted in choosing the peak-weighted squared error as the objective function.

During calibration, we found that only a few parameters were sensitive to the results, which were then chosen as the calibrated parameters in table 4. Former studies also showed that three to five free (for calibration) parameters were recommended for lumped models (Perrin et al., 2001). Thus, in this study, only calibration of partial parameters was conducted, and uncertainty analysis was based on these parameters.

1. Terrain and hydrologic unit data

Figures B1 and B2 show the DEM data and HUC data for the lower Brazos River basin. The DEM data was used in HEC-GeoHMS to generate subbasins (HUC was used as a reference for manually adjusting the delineated subbasins) and reaches as well as estimation of parameters such as drainage area, time of concentration, reach length, and energy grade. The software has built-in functions to estimate those parameters and populate the values to the properties of each subbasin.

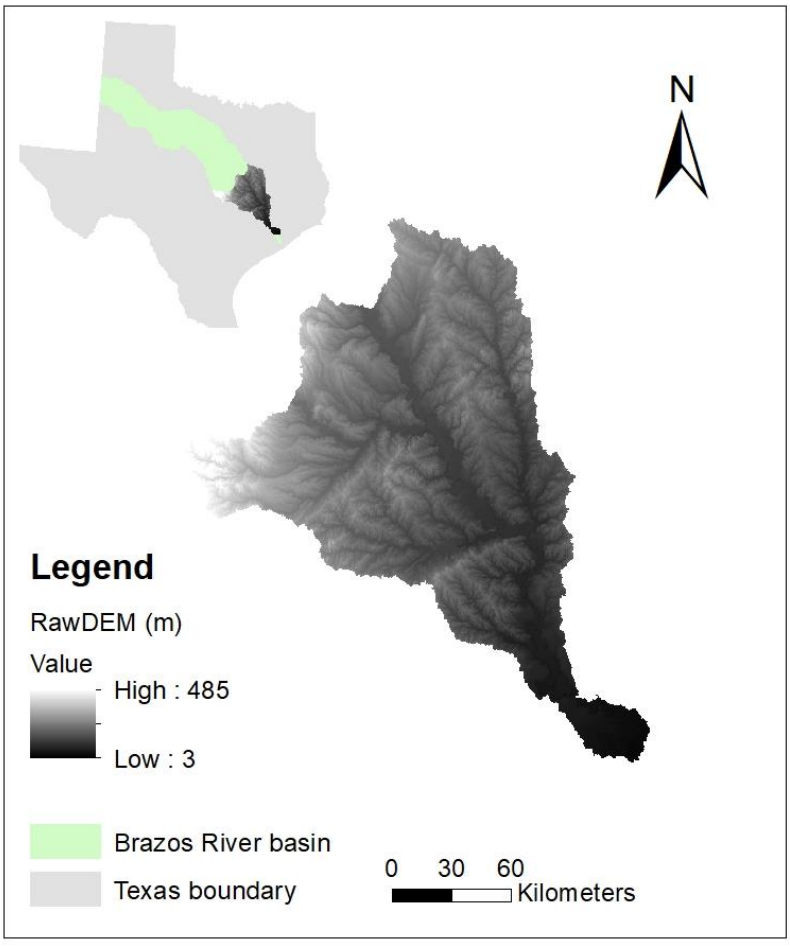

Figure B1. DEM data of lower Brazos River basin

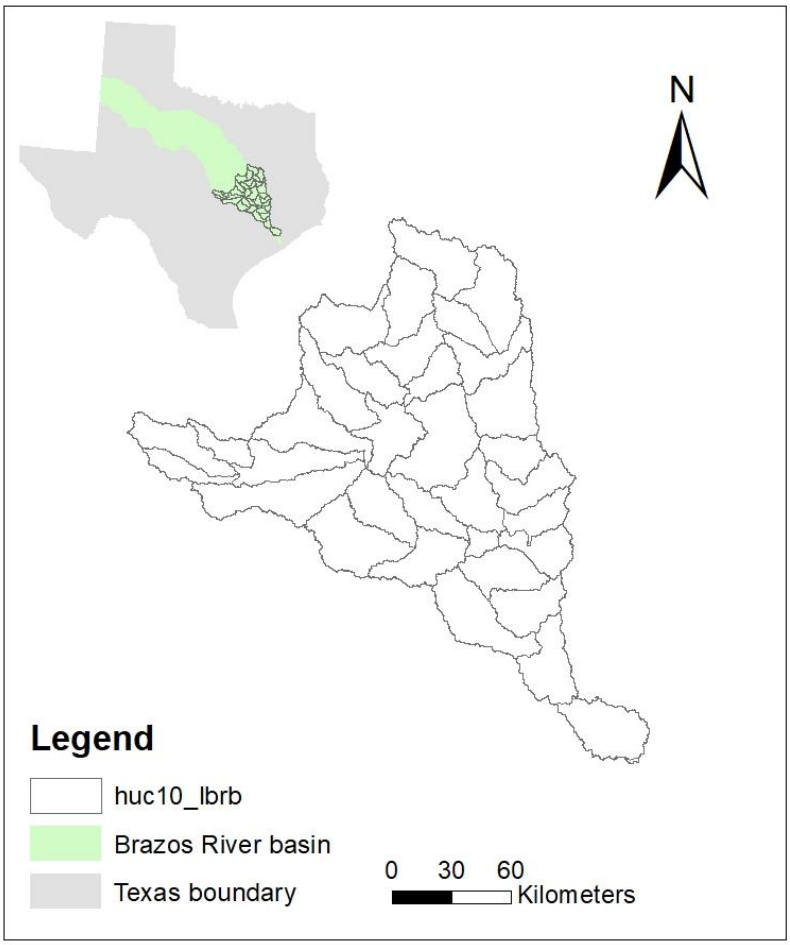

Figure B2. 10-digit HUC within lower Brazos River basin

2. Initial loss and constant loss rate

The initial and constant loss method required an initial estimation of the initial loss and constant loss amounts during the event. The initial loss was estimated by the land use cover type and associated interception loss provided by CECW-EH Engineering Manual 1110-2-1417, flood runoff analysis. In Table 6-1 of the manual, it describes surface losses and interceptions amount ranges due to different land use types. Referring

to the ranges, we assigned different loss amounts to different land use types. The land use cover data (figure B3) was downloaded from https://www.mrlc.gov/data/legends/national-land-cover-database-2016-nlcd2016-legend. Then the initial loss map (figure B4) was calculated from Table 6-1 matching figure B3.

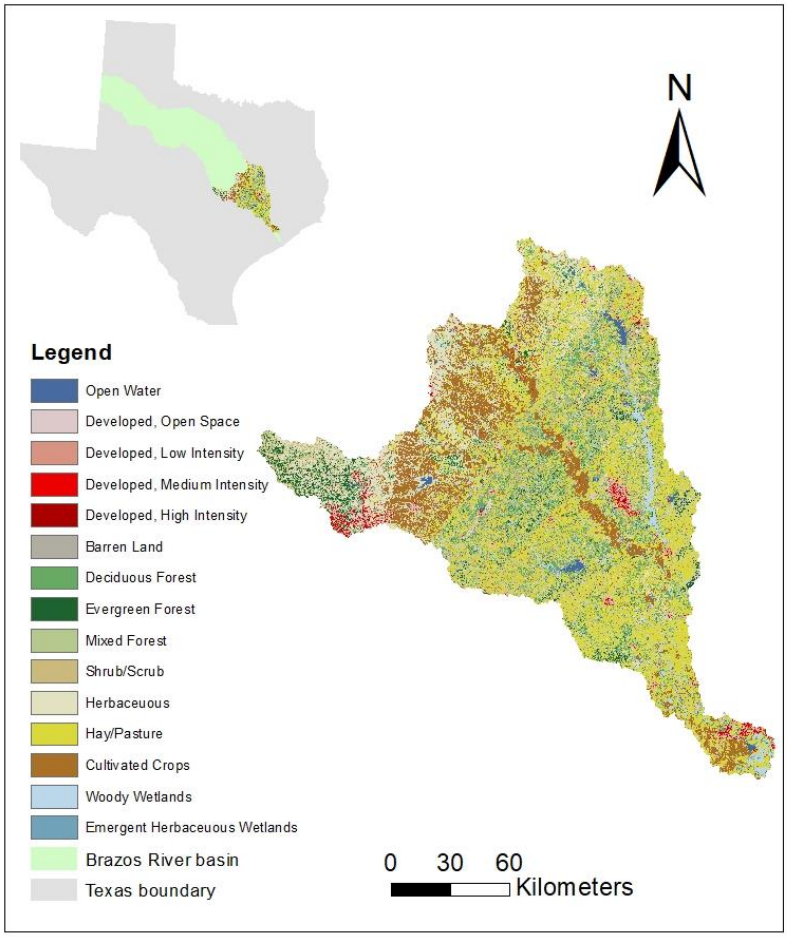

Figure B3. Land use cover within lower Brazos River basin

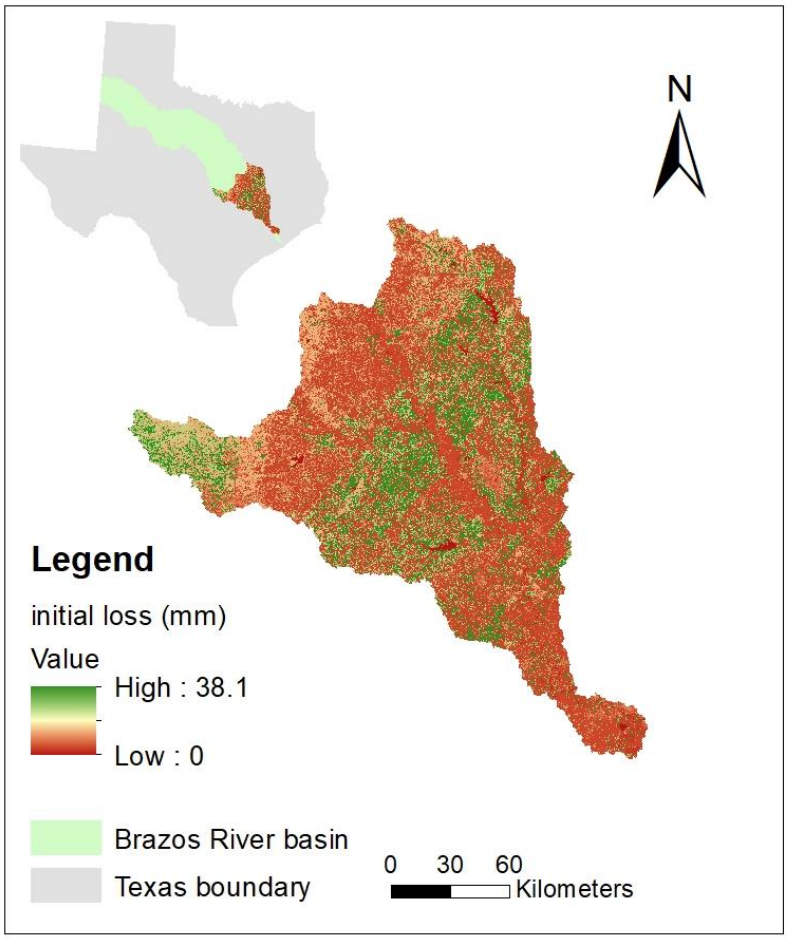

Figure B4. Initial loss within lower Brazos River basin

According to Soil Conservation Service (1986) and the study by Skaggs and Khaleel (1982), we referenced table B1 and the hydrologic soil group in the study area to estimate the constant loss rate in the area. Soil data were downloaded from USDA NRCS website (https://websoilsurvey.sc.egov.usda.gov/App/WebSoilSurvey.aspx). Figure B5 shows the soil group within lower Brazos River basin and figure B6 shows the constant loss rate.

Table B1. SCS soil groups and infiltration (loss) rates (SCS, 1986; Skaggs and Khaleel, 1982)

Soil Group	Description	Range of Loss Rates (mm/hr)
A	Deep sand, deep loess, aggregated silts	7.6-11.4
B	Shallow loess, sandy loam	3.8-7.6
C	Clay loams, shallow sandy loam, soils low in organic content, and soils usually high in clay	1.3-3.8
D	Soils that swell significantly when wet, heavy plastic clays, and certain saline soils	0.0-1.3

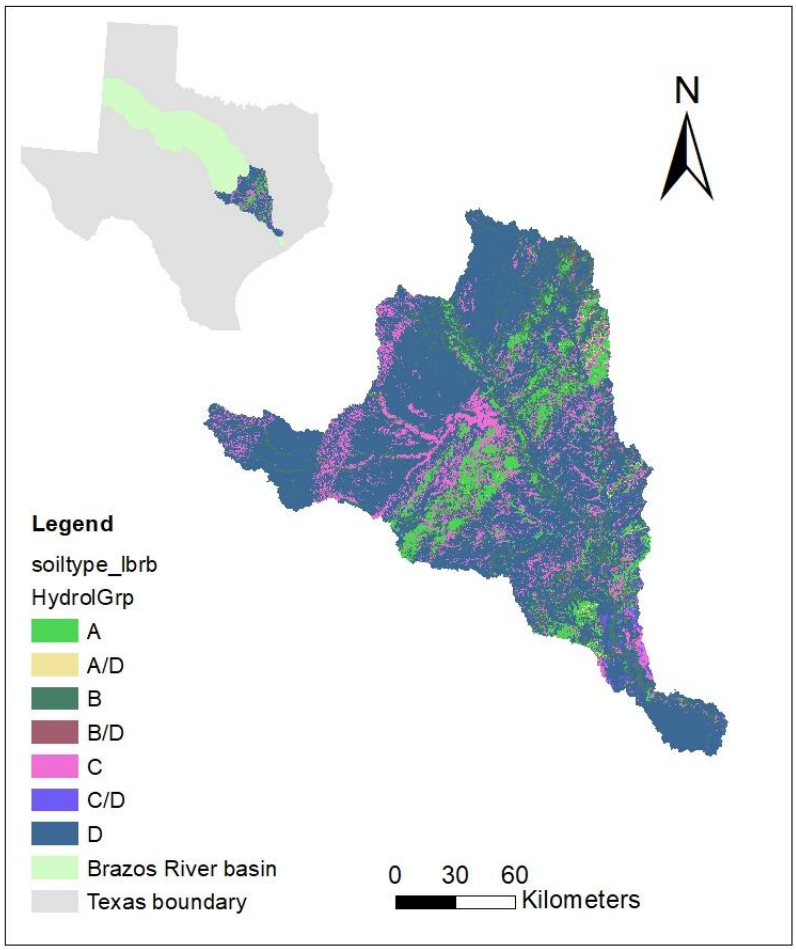

Figure B5. Soil group within lower Brazos River basin

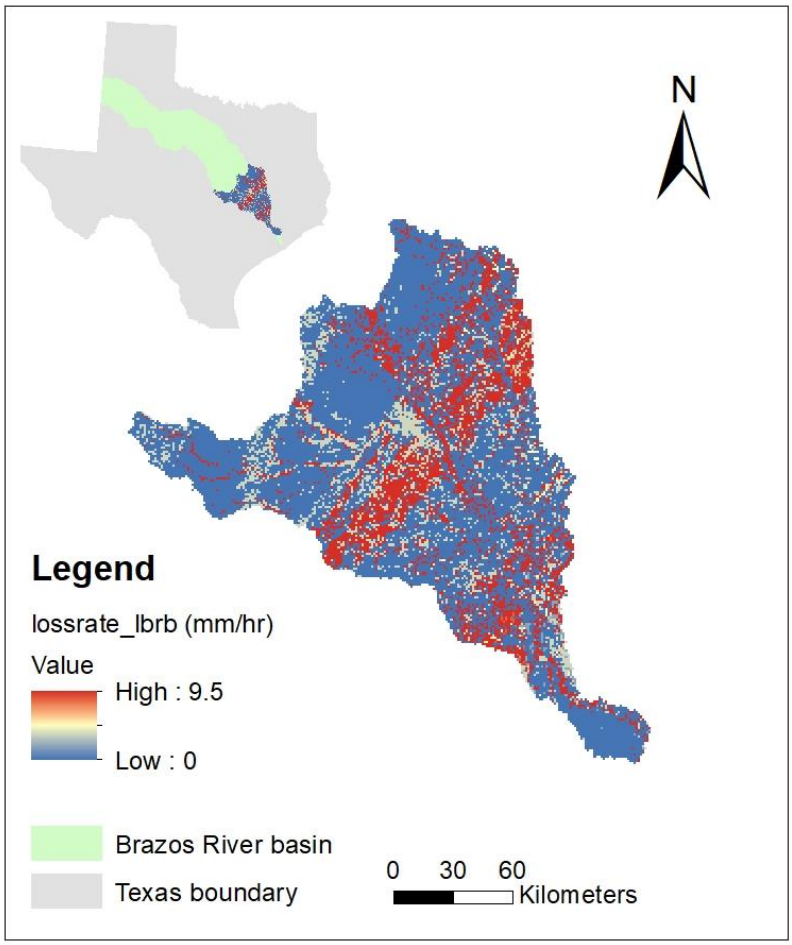

Figure B6. Loss rate within lower Brazos River basin

3. Curve number

The SCS CN model requires CN values derived from land use classification data (figure B3) and hydrologic soil group data (figure B5). The calculation of CN using those two data sources can be referred to Table 2-2 in Technical Release 55 (TR55) (Cronshey, 1986) from USDA. The final generated CN map is shown in figure B7. In

addition, HEC-HMS utilized the impervious percentage to reflect the partial runoff without loss. Impervious area in the watershed is that portion which all contributes precipitation runoffs, without infiltration, evaporation, or other volume losses. On the other hand, precipitation on pervious area is subject to losses. The impervious percentage map shown in figure B8 was downloaded from the MRLC website.

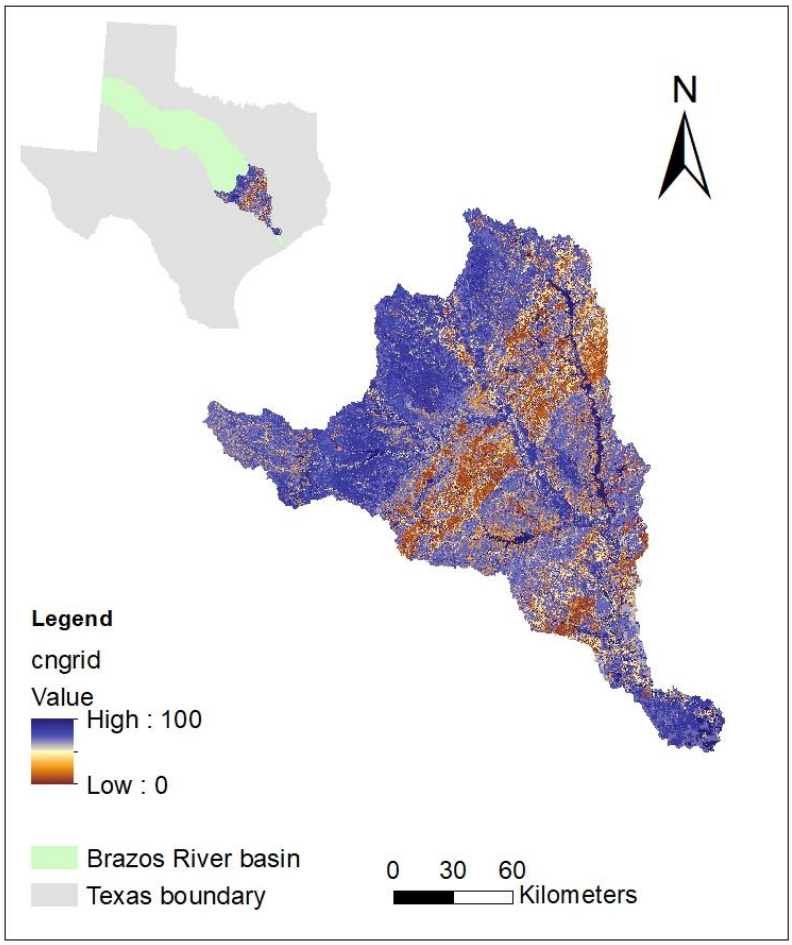

Figure B7. CN values within lower Brazos River basin

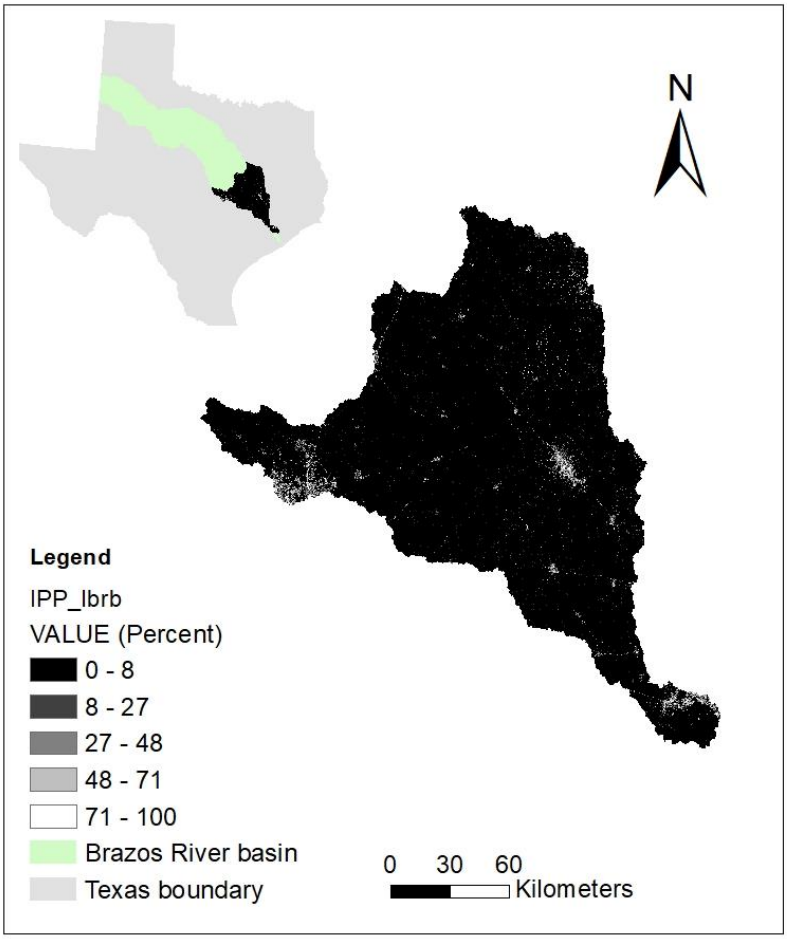

Figure B8. Impervious percentage within lower Brazos River basin

4. Initial baseflow and baseflow recession constant

Initial baseflow Q_0 was collected from the available discharge flow records from USGS website. The recession constant K can be estimated from flow discharge data. From equation (42), flows prior to the start of direct runoff can be plotted and an average of ratios of ordinates spaced one day apart can be computed.

5. Constant linear reservoir parameter (storage coefficient)

The storage coefficient *R* is an index of the temporary storage of precipitation excess in the watershed as it drains to the outlet point. *R* has unit of time and the value of it is computed by the ratio of flow at the inflection point on the falling limb of the hydrograph to the time derivative of flow (Clark, 1945). Sabol (1988) introduced a method to estimate *R* using the technique of hydrograph recession analysis. After a series of transformation from the recession equations and linear reservoir equations from Clark unit hydrograph method, a relationship between *R* and *K* was developed as shown in equation (15) in the original study. *R* is then estimated as *K* is known.

6. Time of concentration

The time of concentration (t_c) of the subbasin is an important parameter in the model. It represents the time of the rainfall excess travels from the farthest point to the outlet. This study referred to TR 55 and estimated t_c as the sum of three segments: travel time of sheet flow, shallow concentrated flow, and open channel flow. In the calculation, the roughness coefficient was estimated from Table 3-1 in TR 55; the reach length *L* and energy grade S_e were estimated from HEC-GeoHMS with DEM data; the shape of the channel was assumed to be trapezoidal, the bottom width *W* of the river was estimated using Google map, the side slope S_s was assumed to be 30°, and the hydraulic radius was calculated accordingly; the 2-year 24 hour duration rainfall in Texas was collected from USGS Water-Resources Investigations Report 98–4044 U.S. report (Depth-Duration Frequency of Precipitation for Texas).

7. Calibration and validation event periods and reservoir data

Hurricane Harvey, that occurred during August 24 through September 1, 2017, was used as the calibration event. The time period from October 24, 2015 through November 1, 2015 from Hurricane Patricia was used as the validation period. For the major reservoirs may affect the simulation during the simulation, we used instant outflow release data in the streams where the reservoirs are located. There are three main reservoirs included in the study area: Lake Limestone, Lake Granger, and Lake Somerville. The instant outflow data from those reservoirs were collected from the U.S. Army Corps of Engineers (USACE) Fort Worth district website. (http://www.swf-wc.usace.army.mil/cgi-bin/rcshtml.pl?page=Hydrologic).

APPENDIX C

AVERAGE AREAL PRECIPITATION OF PROBABLE MAXIMUM STORM AND HURRICANE HARVEY

The average areal precipitation amount of PMS in the study area was 508 mm, which was around three times of that from hurricane Harvey (169 mm). Table C1 showed the data from HEC-HMS and the calculation of the average areal precipitation amount of PMS.

To estimate the 72-hr average areal precipitation happened within the study area, information of hurricane Harvey was refereed from NWS website (https://www.weather.gov/hgx/hurricaneharvey). We used ArcGIS and georeferenced the study area to the hurricane Harvey map as shown in figure C1. The original 5-day rainfall map of hurricane Harvey was downloaded from the NWS website. Then, we estimated the average precipitation in each "rainfall_polygon" area and calculated the area weighted average precipitation within the study area. Table C2 showed the detailed data. The 72-hr amount was estimated from the 5-day amount by multiply the ratio 0.6.

Table C1 Average areal precipitation amount of PMS

Subbasin name	Subbasin area (km^2)	Total average rainfall (mm)	Total rainfall ($km^2 \cdot m$)
W860	345.68	407.8	140982.13
W880	347.71	419.6	145909.55
W810	692.27	417.9	289292.71
W870	805.88	451.5	363854.82
W840	1339.4	381.5	510967.71

Subbasin name	Subbasin area (km^2)	Total average rainfall (mm)	Total rainfall ($km^2 \cdot m$)
W820	1029.2	470.9	484650.28
W730	837.91	764.1	640205.14
W750	724.26	953.5	690596.40
W710	597.17	813.8	485947.09
W650	706.59	501.0	354022.79
W1430	963.89	527.6	508577.28
W1480	798.45	399.6	319084.57
W790	1472.8	847.4	1248094.90
W1530	369.76	472.9	174859.50
W890	811.25	810.1	657193.63
W1010	1141.4	354.1	404112.67
W920	742.07	634.8	471043.77
W990	778.1	598.5	465700.63
W910	588.32	763.7	449317.63
W970	166.68	847.8	141307.97
W960	2.2931	999.5	2291.95
W1130	996.7	378.2	376971.87
W610	900.71	351.4	316491.48
W600	475.7	275.8	131198.06
W660	671.6	277.6	186422.73
W680	961.18	269.9	259412.87
W1180	645.99	513.6	331748.16
W1170	688.52	539.7	371559.82
W950	180.77	750.9	135738.39
W930	376.7	517.8	195040.19
W1230	429.9	456.1	196060.19
W1220	718.32	618.6	444367.12
W1280	703.9	474.8	334197.64
W1070	1095.6	386.9	423854.77
W1330	797.93	277.3	221242.05
W1100	953.77	283.7	270622.70
Sum	25858.37	N/A	13142941.2
Average rainfall (mm)			508.3

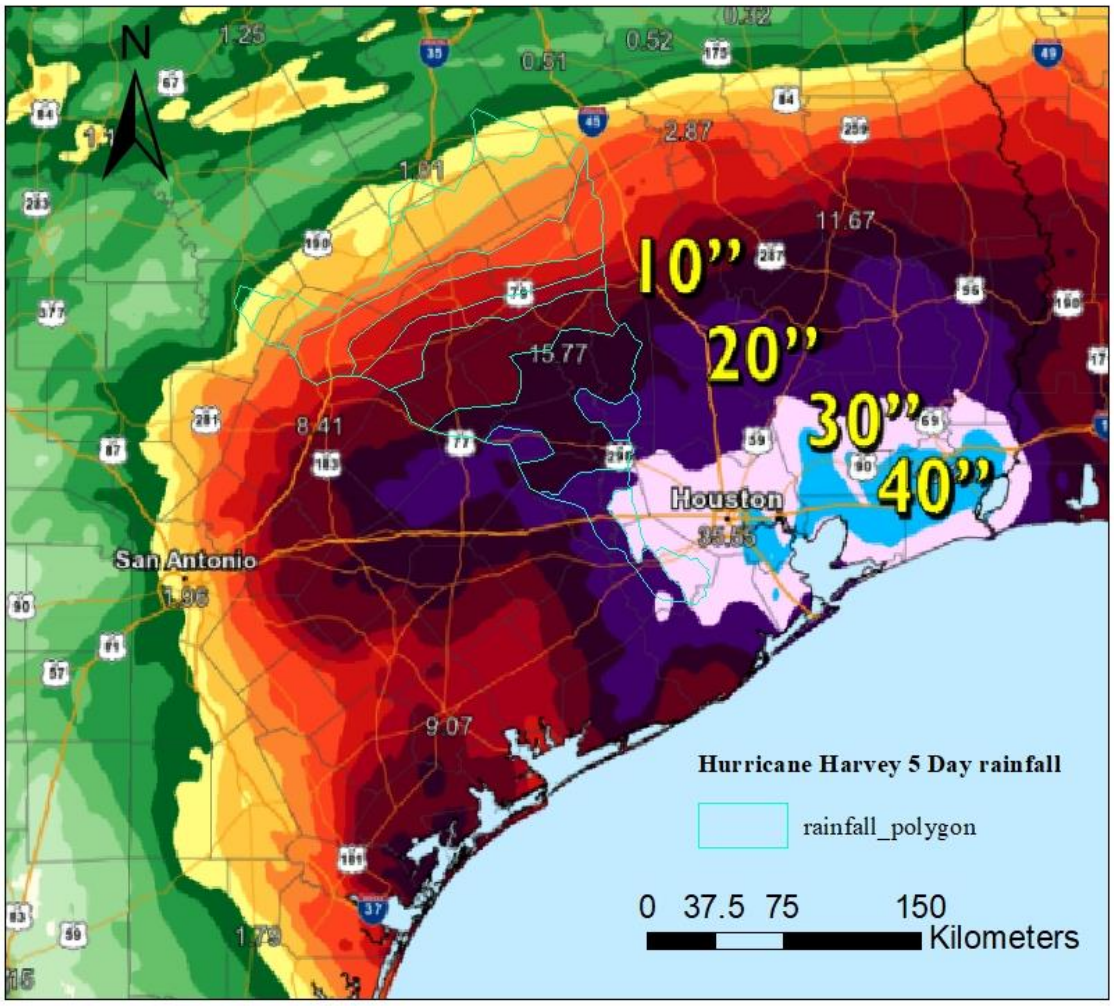

Figure C1 Estimation of 72-hr average areal precipitation of hurricane Harvey within the study area

Table C2 Average areal precipitation amount of hurricane Harvey

Rainfall_polygon ID	5-day precipitation (mm)	Area (km^2)	Total precipitation ($km^2 \cdot mm$)
1	889.0	483	429088.3
2	889.0	375	333202.5
3	635.0	1411	895991.4
4	635.0	433	274835.0
5	635.0	572	363496.9
6	444.5	4731	2102929.5
7	63.5	531	33735.6

Rainfall_polygon ID	5-day precipitation (mm)	Area (km^2)	Total precipitation ($km^2 \cdot mm$)
8	44.5	159	7085.1
9	317.5	3861	1225962.8
10	31.8	76	2427.7
11	228.6	1761	402548.6
12	177.8	2145	381366.8
13	44.5	347	15417.9
14	127.0	3272	415538.9
15	88.9	2684	238630.7
16	63.5	2303	146231.6
17	44.5	724	32200.5
SUM		25869	7300689.6
Average precipitation (mm)			282.2